T. Striekwold

Heating Properties of Holmium Doped Nanoparticles

For Image Guided Thermo-Brachytherapy

TUDelft

Heating Properties of Holmium Doped Nanoparticles

For Image Guided Thermo-Brachytherapy

By

T. Striekwold

in partial fulfillment of the requirements for the degree of

Master of Science
in Applied Physics

at the Delft University of Technology,
to be defended publicly on Thursday, December 17, 2020, at 14:00.

Supervisor:	Ass. Prof. dr. ir. A. Denkova	TU Delft
Thesis committee:	Ass. Prof. dr. ir. K. Djanasjvili	TU Delft
	Prof. dr. S.. Picken	TU Delft

TUDelft   REACTOR INSTITUTE DELFT

Acknowledgements

Abstract

Because diagnostics have improved tremendously, nowadays breast cancer is more frequently detected at an early stage. Long-term prognosis is excellent and therefore the new treatment should focus on minimizing long-term side effects and treatment burden. This research proposes cancer treatment using nanoparticles (NPs) for a combination of heat therapy and brachytherapy. For the NP design, superparamagnetic iron-oxide nanoparticles (SPIONs) will be used. Because of their biocompatibility and good magnetic properties, they are suitable candidates for heating using an alternating magnetic field. To make the NPs applicable for brachytherapy, the NPs are doped with holmium (Ho), a lanthanide with high magnetic moment and radioisotope Ho-166. Furthermore, SPIONs and Ho change the relaxivity of water protons and therefore they can be used as contrast agents for magnetic resonance imaging. This makes it possible to image the NPs during the treatment and enables thermal planning and dose-rate calculations delivered to the cancer tissue to be performed.

The incorporation of Ho inside the iron-oxide structure is expected to change the magnetic properties of the NPs. The success of using Ho as contrast agent and for brachytherapy purposes have been proven in several researches. However, the influence of Ho on the heating performance of these SPIONs is unknown. This research will characterize the magnetic properties of undoped and Ho-doped SPIONs and compare them, in order to examine the heating possibilities of Ho-doped NPs.

For the synthesis of the NPs a spark discharge generator was used. Spark ablation is a synthesis method able to yield narrow size distribution of different metallic particles and alloys. However, since spark ablation is relatively new, the synthetic methodology itself had to be developed. Therefore, this research was divided into two parts: 1) the synthesis of NPs using spark ablation and 2) the characterization of Ho-doped iron NPs and the comparison with undoped SPIONs.

Since the first part focused on the spark ablation synthesis, the influence of the generator settings on the primary particle size was investigated using DLS and TEM. The VS-Particle generator was able to produce 4 nm Fe-Fe and Ho-Fe NPs, a size that is smaller than expected. The generator settings did not influence the primary particle size and therefore, the settings of the generator were chosen to maximize the yield. The initial set-up had low yield and therefore, the influence of micro-bubbler, electrode configuration and bubbling column were examined and changed to improve the yield. A bronze sintered filter with pore size 0.4-20 μm, solid iron electrodes and 60 mL bubbling column volume appeared to be the most optimal.

During the second part of this research, 4 nm Ho-doped iron oxide NPs and un-doped iron oxides were produced. They were characterized using TEM, DLS, XRD, ICP, SEM-EDX, Mössbauer spectroscopy, SQUID and NMR. As a result of low concentrations obtained, no good qualification of the produced particles could be obtained. All particles showed superparamagnetic behavior and influenced the relaxivity times of water protons. To what extend the relaxivity was changed upon doping remains unfortunately unclear, because the composition of the NPs is unknown.

It can be concluded that the used set-up was not able to produce reproducible NPs and therefore no reliable characterization could be done on the Ho doped particles. Future research should focus on a more controllable synthesis method to be able to examine the possibilities of Ho for heating purposes.

Table of Content

1   Introduction

Breast cancer is one of the most common types of cancer in the world.[1,2] Extensive research has been done on the diagnosis and treatment of this disease. As a result, breast cancer is more frequently diagnosed at an early stage. Because the long-term prognosis of breast cancer is very good, the new challenge is to minimalize the side effects of the treatment.[3,4]

Current treatment mostly consist of a combination of surgery and external beam radiotherapy (EBRT), which is a time-consuming treatment, possibly leaving the patient with deformations. A new treatment approach consists of the implantation of nanoparticles for heating therapy in combination with brachytherapy. This is a minimally invasive treatment with minimal or no side-effects and excellent cosmetic results.[5,6]

By applying an alternating magnetic field (AMF), NPs will heat up due to hysteresis and relaxation processes.[7,8] Thermal ablation involves heating the tissue above 50 °C which causes direct cell death due to a heat shock, while hyperthermia implies the heating of tissues up to 42 °C and is mainly used in combination with ionizing radiation. Under heat exposure, DNA repair is inhibited and therefore, cells are less capable of recovering from ionizing radiation exposure. Hence, hyperthermia indirectly affects the treatment of cancer cells.[9,10]

Given the potential of NPs in cancer treatment, a large amount of research is directed to superparamagnetic iron oxide nanoparticles (SPIONs).[11] The biocompatibility of superparamagnetic particles combined with iron oxide's magnetic properties make SPIONs an ideal candidate for heating therapy.[12,13] By doping SPIONs with radio-isotopes, heating therapy and brachytherapy can be combined. The dopants can also enhance the magnetic properties of the SPIONs. Transition metals are known to be effective dopants, but lanthanides are even more promising due to their beneficial magnetic properties conditioned by a unique electron configuration.[12–16] Holmium (Ho) is a lanthanide known for its radioisotope Ho-166, which decays under emission of β- and γ radiation. Ho also possesses high magnetic moments and is therefore a good candidate as dopant in SPIONs for better heating properties and as brachytherapy agent.[14,17,18] Furthermore, magnetic NPs alter the protons' relaxation properties in water and can therefore enhance the contrast between tumor and healthy tissues. Both SPIONs and Ho are known to work as effective T_2 contrast agents and can be used for imaging of the NPs and dose calculations.[6,17,19]

Research has proven the application of 166Ho as a suitable dopant for brachytherapy and diagnostic technologies like MRI and SPECT. However, the effect of doping SPIONs with Ho on the heating properties of SPIONs is still unknown. The goal of this research is to examine the influence of Ho doping on the heating of SPIONs. To answer this question, Ho-doped SPIONs were synthesized, characterized and their magnetic properties were evaluated.

To improve the applicability of NPs, efficient synthetic methods are being explored to achieve NPs with a high yield and a narrow size distribution. In this research, a spark discharge generator (SDG) developed by VS-Particle was exploited. Since this method is relatively new, the synthetic methodology itself had to be developed. Therefore, this research on Ho-doped SPIONs can be divided into two parts: 1) synthesis and 2) characterization and comparison with undoped SPIONs. Theoretical study preceding the actual experimental verification of the hypothesis comprises an important part of this thesis.

2   Theory

2.1   Magnetic Properties

Magnetism originates from the orbital and spin motions of electrons around their nuclei and how the electrons in a material interact with each other. The occupation of orbitals by electrons is arranged according to the quantum rules, which leads to different interactions between materials. Electrons follow Pauli's exclusion principle, which states that two electrons cannot occupy the same state. This results in the fact that only electrons of opposite spins can fill a single orbit. Therefore, if an orbit is completely filled, the net spin will be zero. These electrons with opposite spins are called electron pairs.

Electrons also follow Hund's rule, which states that first, one spin direction is filled before the opposite one is filled. This leads to unpaired electron pairs. Only electrons from unfilled orbitals will interact with other unpaired electrons. The interaction may be repellent in case of spins with the same direction or attractive when spins of the opposite directions are involved.

Magnetic material classes

The total magnetic properties are a result of the way the collective of spins interact with each other. Five main classes of magnetic materials can be distinguished, based on the way they respond to a magnetic field. These five classes will be briefly explained below and summarized in Table 1.[20]

Diamagnetism

Diamagnetic materials consist of atoms with all orbital shells filled and therefore have no unpaired electrons. As a result, the atoms have no net magnetic moment and the material will have zero magnetization if no external field is applied. If an external field is applied, an electrical current is induced inside the electron orbits. The electron current that is induced by the magnetic moment has a sign that is opposite to that of the applied field and therefore, the diamagnetic material will get a net magnetization in the opposite direction of the applied magnetic field.[20]

Paramagnetism

In paramagnetic materials, the atoms or ions do have unpaired electrons and therefore can have a net magnetic moment. For zero external magnetic field, the magnetic moments of different atoms cancel each other and the total magnetization of the material is zero. However, when an external field is applied, the magnetic moments will tend to partially align to the external magnetic field and a net positive magnetization will occur. The fraction, which aligns is proportional to the magnetic field strength and therefore the magnetization is linear. Since the unpaired electrons are the reason magnetization occurs, high spin elements will have more pronounced paramagnetic behavior.

Ferromagnetism

Ferromagnetism only occurs in materials for which the same atoms are arranged in periodic lattice structures. In these periodic lattice structures, individual atomic magnetic moments align with each other. The unpaired spins line up parallel with each other and cause a net magnetization for a nearby group of atoms. This group of neighboring atoms with a net magnetization is called a magnetic domain. Because all magnetic domains are oriented randomly, the bulk magnetization is zero. If an external magnetic field is applied, all magnetic domains can be aligned, and the bulk material will have a net magnetization.

Ferromagnets tend to remember their magnetization once the external field is removed. The magnetization which remains after the external field is removed is called the remanence. This remanence is the driving force of permanent magnets which are used in daily life.

The magnetization of a ferromagnet in absence of an external field is dependent on the number of unpaired electrons which will interact with each other and the size of the magnetic domains. Smaller domains will lead to a bigger difference between the initial magnetization and the saturation magnetization. At high temperatures, thermal energy will overcome the exchange of electronic forces and will randomize the magnetic moments of the material. Therefore, above a certain temperature, all ferromagnetic property disappears (Figure 1). This temperature is called the Curie Temperature.[20] The effect of the magnetic domain will be explained in more detail later on.
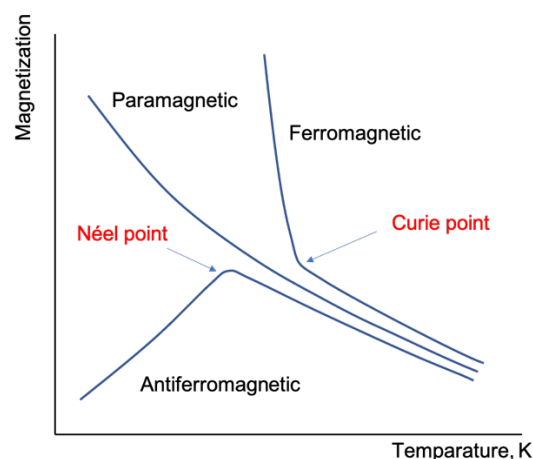
Figure 1 Temperature behavior of paramagnetic, ferromagnetic and antiferromagnetic material. The Curie temperature is the temperature above which ferromagnetic material will act as a paramagnetic material and the Néel temperature is that temperature for an antiferromagnetic material.[20]

Ferrimagnetism
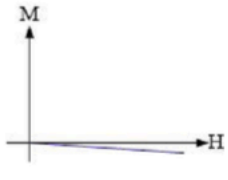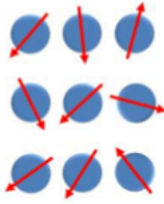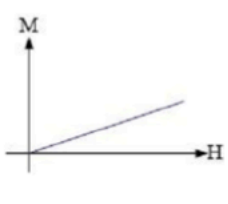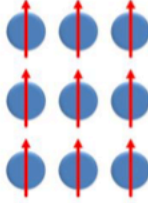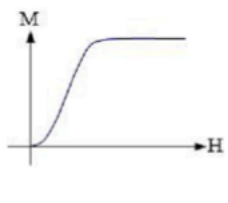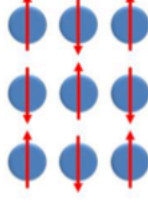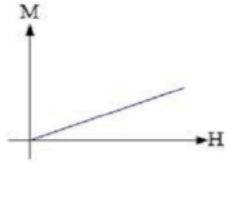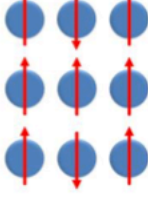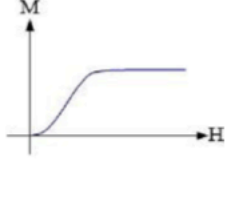
Ferrimagnetism is a result of more complex lattice structures than that of pure elements as with Ferromagnets. For ferrimagnets, the total spontaneous and saturation magnetization is still a result of individual magnetic domains, however, the domains now consist of magnetic moments, which do not align perfectly. Therefore, single domains have lower magnetization and the saturation magnetization will also be lower than that of the ferromagnets.

Antiferromagnetism

Antiferromagnetic materials resemble the structure of ferromagnets in the sense that all atoms are periodically structured and have strong exchange interactions between the neighboring

atoms. However, with antiferromagnets, the magnetizations of neighboring atoms align antiparallel and therefore cancel. As a result, the saturation magnetization is decreased. Just like ferromagnets, there is a temperature at which the alignment of atoms is overcome, and the antiferromagnetic material will behave like a paramagnet. For antiferromagnets this temperature is called the Néel temperature. The temperature behavior of paramagnets, ferromagnets and antiferromagnets is shown in Figure 1.

Table 1 Summary of types of magnetism[20]

Type	Example	Atomic / Magnetic behavior		
Diamagnetism	Inert gases; many metals Au, Cu, Hg; non-metalic elements B, Si, P, S; ions Na^+, Cl^-; molecules H2, N_2; H_2O	Atoms have no magnetic moment. Susceptibility is small and negative, -10^{-6} to -10^{-5}		
Paramagnetism	Some metals Al, some diatomic gases O_2, NO; ions of transition metals and rare earth metals; rare earth oxides	Atoms have randomly oriented magnetic moments. Susceptibility is small and positive, 10^{-5} to 10^{-3}		
Ferromagnetism	Transitions metals Fe, H, Co, Ni, alloys of ferromagnetic elements; some alloys of Mn, MnBi, Cu_2MnAl	Atoms have parallel aligned magnetic moments. Susceptibility is large (below T_c)		
Anti-ferromagnetism	Transition metals Mn, Cr and many of their compounds, MnO, CoO, NiO, Cr_2O_3, MnS, MnSe	Atoms have antiparallel aligned magnetic moments. Susceptibility is small and positive 10^{-5} to 10^{-3}		
Ferrimagnetism	Fe3O4 (magnetite); mixed oxides of iron and other elements such as Sr ferrite	Atoms have mixed parallel and antiparallel aligned magnetic moments. Susceptibility is large (below T_c)		

2.1.1 Hysteresis loop

From looking at a hysteresis loop as displayed in Figure 2, a lot can be learned about the properties of a material. For ferromagnets, ferrimagnets and antiferromagnets the magnetization is initially zero. If an external magnetic field is applied, the magnetization will increase with the magnetic field until the saturation magnetization M_S is reached. Once an external magnetic field has been applied, magnetization will stay even if the magnetic field is turned off. This is called the remanent magnetization M_R. To turn around the magnetic orientation, an extra magnetic field strength has to be applied to get the total magnetization to zero. The amount of extra field strength needed is called the coercive magnetization H_C. The need for extra magnetic field results in extra work done per reversal of the magnetization. This is the property, which is used in hyperthermia and will be explained in the next chapter. Along with the Curie and Néel temperature, the hysteresis loop will describe the fundamental behavior of all magnetic materials.
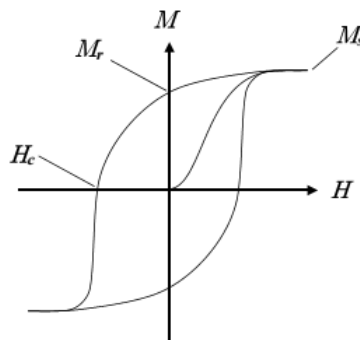
Figure 2 Hysteresis loop ferromagnetic material. The magnetization is showed as a function of applied magnetic field.[20]

2.1.2 Magnetic domains

The magnetic properties are highly dependent on the size of the nanoparticles that are made out of magnetic material. Magnetic domains are generated to minimize the total energy in a material. In general, the total energy is the sum of the magnetostatic, exchange, anisotropy and Zeeman energies[20].

For a growing particle, the exchange energy will stay minimal for perfect alignment of the dipole spins of atoms. However, at a certain point the magnetostatic energy, which increases with the alignment of these spins will overgrow the increase in exchange energy for non-alignment and therefore a second domain will be formed (Figure 3).
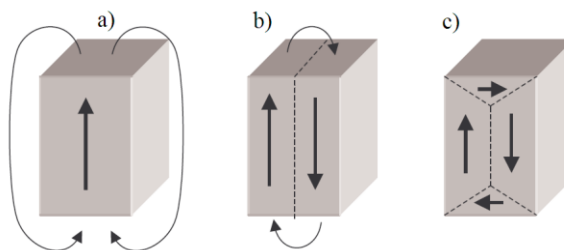
Figure 3 Schematic representation of the domain formation from a single domain (a) to double (b) and 4 domains (c)[20]

The interplay of all interactions and energies which cause this domain formation are all grain size-dependent. However, the magneto-crystalline saturation magnetization, the exchange interaction, the composition and the temperature of the material also play an important role in the domain formation. Because there are a lot of variables, it is very hard to give a prediction

on the domain formation. However, as a rule of thumb it can be stated that the number of domains grows with the grain size.
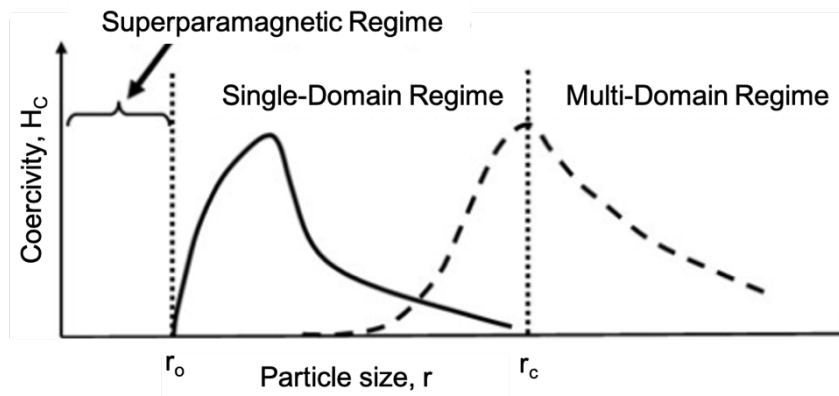
Figure 4 Coercivity as a function particle size. [13,57,59]

Figure 4 shows the coercivity changing with the increase in particle diameter. Above a certain size (r_0), the number of aligned dipoles increases until the magnetostatic energy increases more than the exchange energy is saving by perfect alignment. Therefore, the multi-domain regime is reached at r_c. There is also a regime on the left of the single domain limit, which is called the superparamagnetic region. In this region, the magnetic anisotropy energy is smaller than the thermal energy of the environment. Therefore, when no external magnetic field is applied, all particles have a random orientation and the entirety of individual spins will cancel each other. As a result, no remanent or coercive magnetization will be present. However, the saturation magnetization is very high when an external magnetic field is applied, because all individual spins are able to align. Superparamagnetism can occur for both ferro,- and ferrimagnetic materials.

2.2 Magnetic Nanoparticle Heating Mechanisms

Heating can be achieved using several heat sources like electromagnetic radiation waves, ultrasound waves or electrical induction.[21] However, these techniques cause a homogeneous heat distribution throughout a tissue. Because these heating methods are nonspecific to tumor cells, the peritumoral cells will be damaged as much as tumor cells. To target specific tissue with heat, magnetic nanoparticles should be introduced and subsequently subjected to an alternating magnetic field (AMF). The magnetic nanoparticles can be inserted into the tumor or they can target the tumor cells via the EPR effect. Under exposure of an AMF, primarily cancer cells will be heated. The heat released is characterized by the specific absorption rate expressed in $W\,g^{-1}$ and is given by the following equation:

$$SAR = \frac{\Delta T}{\Delta t}\frac{C}{m} \tag{1}$$

where C is the heat capacity of the fluid per mass and m is the concentration of NPs in the suspension.[22] The SAR values of a material are roughly proportional to the magnetic saturation value, the magneto-crystalline anisotropy constant (K) and inversely proportional to the size distribution of the nanoparticles. Several mechanisms can induce heat production. Below, frictional heating, hysteresis heating and relaxation heating are explained.[8]

2.2.1 Hysteresis Heating

As explained before, to reverse the magnetic orientation, extra work has to be done to overcome the remanent magnetization in ferromagnetic materials. The amount of extra work is equal to the area enclosed by the hysteresis loop. The work done on the NPs is converted into thermal energy and this thermal energy is the heat that can be used for heating. The power with which thermal energy is applied is given by the frequency of the AMF times the integral of the B-H curve of this closed loop:[10]

$$P_{heat} = f\mu_0 \oint \vec{H}\,d\vec{M} \tag{2}$$
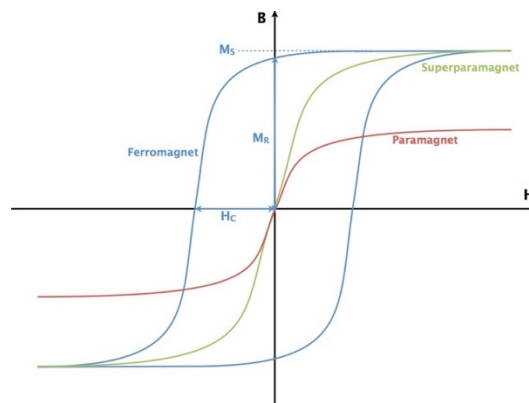

Figure 5 Hysteresis loop for paramagnetic, ferromagnetic and superparamagnetic nanoparticles.[8]

2.2.2 Relaxation Heating

If particles decrease in size, they will lose their ferromagnetic behavior and will become superparamagnetic. In Figure 5 it can be seen that the paramagnetic and superparamagnetic materials do not have remanent magnetization and therefore the enclosed area of their hysteresis loop is zero. However, Chan and Chou[23] evaluated the heating of Fe_3O_4 superparamagnetic NPs exposed to AMF and still found heating. They concluded that heating in the superparamagnetic nanoparticles is caused by Néel relaxation.

In a crystal lattice, there is a preferred alignment for the magnetic vector of the superparamagnetic nanoparticles and the lattice structure. Therefore, after the distortion of an external pulse, relaxation will take place. The realignment of magnetic dipoles of the NPs causes magnetic friction which generates heat.[8,22] Thus, superparamagnetic particles are indeed able to generate heating due to Néel relaxation. The Néel relaxation time is given by eq (3).

$$\tau_N = \tau_0 e^{\frac{K_u V_M}{k_B T}} \tag{3}$$

where τ_0 is a constant depending on the material used, which is also called the attempt time, K_u is the anisotropy constant, V_M is the hydrodynamic volume. The total heat produced per NP is equal to the energy per relaxation time, multiplied by the number of relaxations. To have efficient heating, the time between the alternating magnetic pulses should be the same as the relaxation time.

Not only the Néel relaxation can produce heat, but also Brownian relaxation. Where Néel relaxation only changes the spin of the NPs and keeps the particles fixed, Brownian relaxation will rotate the whole NP. By rotating the NP, friction between the NP and the environment will generate heat. The Brownian relaxation time is given by eq (4):

$$\tau_B = \frac{4\pi\eta V_M}{k_B T} \tag{4}$$

where η is the viscosity of the fluid, r_{hydr} is the hydrodynamic radius, k_B is the Boltzmann constant and T is the absolute temperature.[24]

I order to have ferromagnetic, antiferromagnetic or ferrimagnetic properties particles must be bigger than superparamagnetic nanoparticles. Therefore, the hysteresis heating is the dominant heating mechanism for bigger particles ($\geq 100 nm$). In the superparamagnetic regime, the dominant Brownian and Néel relaxation occur at the same time, so the effective relaxation time is given by eq (5).[25]

$$\frac{1}{\tau} = \frac{1}{\tau_B} + \frac{1}{\tau_N} \tag{5}$$

From equation (5) it can thus be seen that the effective relaxation is dominated by the shorter of the two. That means that Brownian relaxation will dominate at larger particles and lower viscosities and Néel relaxation will be dominant for small particles and viscous solutions. However, typical magnetic field frequencies used in experimental studies favor relaxation times in which Néel is dominant.[26]

The power with which heat is produced is given by:

$$P_{heat} = \frac{1}{2}\omega\mu_0\chi_0 H^2 \frac{\omega\tau}{1+\omega^2\tau^2} \tag{6}$$

where ω is the angular frequency, H the magnitude of the applied field and μ_0 and χ_0 are the magnetic permeability and susceptibility.[10,27]

2.3 Magnetic Resonance Imaging (MRI)

Magnetic Resonance Imaging (MRI) is a non-invasive technique advantageous because of its high spatial and temporal resolution, deep tissue penetration and non-ionizing character.[19,28–30] The contrast and details obtained by MRI originate from the difference in proton relaxation times in various human tissues.[31] Relaxation times are defined by the time it takes for the spins to relax to their thermal equilibrium state after a disturbance by a radio frequency (RF) pulse in the presence of a static magnetic field. The focus within MRI lays on the longitudinal (T_1) and the transverse (T_2) relaxations.

When exposed to a homogeneous external magnetic field B_0 in the longitudinal direction (z-axis), most spins will align along this field inducing a net magnetization M_0. When an RF pulse is applied at 90° with respect to the magnetic field B_0, the net magnetization will be pushed into the transversal plane (xy-plane). For the T_1-relaxation, the relaxation time corresponds with the time it takes for individual spins to re-align along the direction of the static magnetic field (B_0). During an RF pulse, the spins obtain excess energy. For longitudinal relaxation, the energy gained by the RF pulse can only be exchanged with the lattice. Therefore, this relaxation is also called spin-lattice relaxation.

After the RF-pulse is applied, all the spins will be in phase with each other and will all point in the same direction of the applied pulse. Therefore, there will be a nonzero transverse magnetic field M_{xy}. The lifetime of this transverse magnetic field is characterized by the T_2 relaxation time. During this T_2 relaxation, transversal spins will dephase. The spins will interact with each other without letting energy dissipate and therewith changing the transverse energy into longitudinal energy. Because the increase in longitudinal magnetization is only possible due to the decrease in transverse magnetization, $T_2 \leq T_1$ is always satisfied. Because the transverse relaxation is only depending on interactions between spins, it is referred to as spin-spin relaxation. Figure 6 visually explains the relaxations with respect to the initial net magnetization.
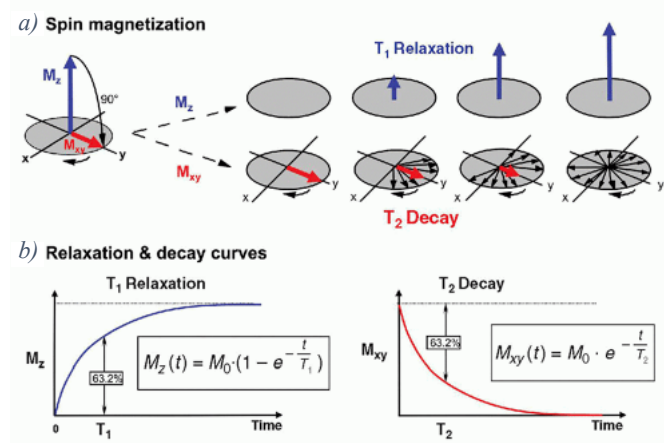
Figure 6: Magnetization orientation of proton spin after an RF-pulse (a) and the corresponding decay relations for T_1 and T_2(b).[32]

As a result of a magnetic field applied by the MRI device, the dephasing is not only a result of the spins exchanging energy but there is also dephasing due to the magnetic field inhomogeneities. A difference is therefore made between T_2 and T_2', where T_2 is the relaxation time due to the material and T_2' is the relaxation time resulting from signal decay due to the external field. The two relaxation times can be combined to give the measured relaxation time

(eq (7)). To exclude the influence of the external magnetic field, a spin-echo sequence can be used.

$$1/T_2{}^* = 1/T_2{}' + 1/T_2 \tag{7}$$

Because the relaxation due to the external field is a static dephasing effect,[33] the phase decay is reversible. If a 180° RF pulse is applied, the spins that were initially dephasing will start to rephase and as a result of symmetry, the dephasing will take the same time as rephasing. Therefore the 180° RF pulse should happen at TE/2, where TE is the time after which an echo is created and therefore describes the degree of T_2-weighting. This is all illustrated in Figure 7.
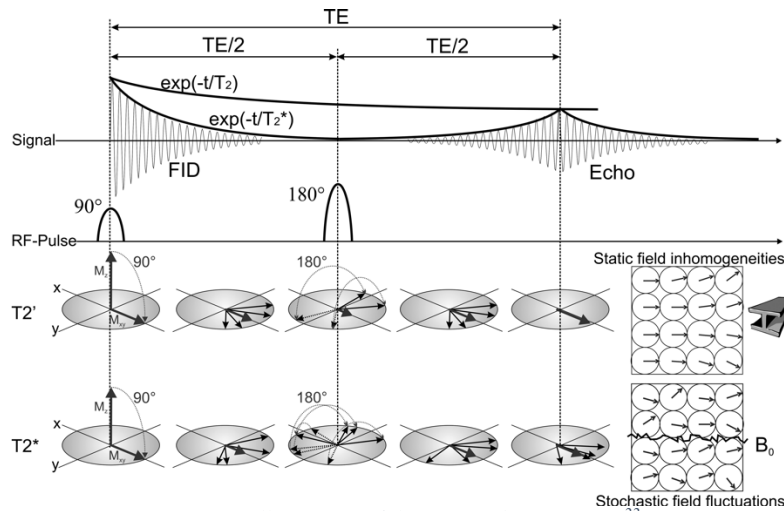
Figure 7 Illustration of the Spin-Echo Sequence.[33]

For too short TE, the transversal spins will rephase the same number of protons in different tissues and therefore do not give any T_2 contrast. TR is the time between excitations and therefore depicts the T_1 weighting. For too long TR the spins will recover their equilibrium and there will be no more T_1 contrast left. This is all illustrated in more detail in Figure 8. Both TE and TR are variables that can influence the contrast of an MRI image and therefore have to be chosen carefully. Typically, for an efficient T_1 contrast short TR and TE and for T_2 contrast long TR and TE are chosen.
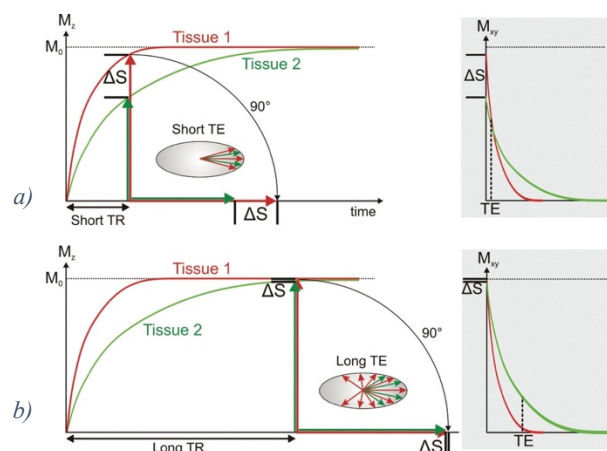
Figure 8 Longitudinal and transversal relaxation for two different materials. Illustrated are the differences in contrast for a) short TE and TR and b) long TE and TR.[33]

2.3.1 Contrast Agents

Contrast agents can be used to increase the signal difference between tissue. Despite the superb resolution compared with other non-invasive imaging techniques like SPECT and PET, the limited contrast agent sensitivity is the main drawback for MRI.[19,29,34] Table 2 summarizes different imaging techniques with their sensitivity. This indicates the need for improvement of contrast agents. Although most contrast agents affect both T_1 and T_2, the effects of contrast agents are in general categorized for either T_1 or T_2.[28] The ability of contrast agents to change the relaxation time is defined by the relaxivities r_1 or r_2 expressed per mM of magnetic substance per second. The ratio of r_2/r_1 for T_1 agents is normally around 1-2, whereas for a T_2 agents this ratio lays above 10.

Table 2 Sensitivity of MRI with contrast agents compared to other imaging techniques.[29,34]

| Modality	Spatial resolution	Dept	Sensitivity (mol/L)
PET	1-2 mm	No limit	$10^{-11} - 10^{-12}$
SPECT	0.5-1mm	No limit	$10^{-10} - 10^{-11}$
MRI	25-100 μm	No limit	$10^{-3} - 10^{-5}$
CT	50-200 μm	No limit	$10^{-2} - 10^{-4}$
Ultrasound	50-500 μm	mm-cm	$10^{-3} - 10^{-4}$

T_1 contrast agents

Contrast agents which reduce T_1 are called positive CAs and make the tissue brighter on the MRI scan.[35] The most common elements used for T_1-weighted contrast are paramagnetic substances like gadolinium complexes. Gd is a paramagnetic lanthanide with seven unpaired electrons in the 4f shell. These unpaired electrons can interact with the surrounding lattice. T_1 relaxation is defined by the interaction between spin and lattice and therefore, more unpaired electrons shorten the T_1.[28] However, poor selective tissue labelling and localization of conventional Gd-complexes are a major drawback in the success of Gd as a contrast agent. The use of Gd inside nanoparticles might overcome these limitations.[36]

The way paramagnetic particles interact with their surroundings can be explained by the inner- and outer-sphere models of the water exchange. For the inner-sphere model, the relaxation depends on the chemical exchange of water molecules directly coordinated to a paramagnetic center with the bulk water in the solvent/surrounding tissues.[35] The outer-sphere model describes the interaction between the total spin of the paramagnetic ion and the spin of long-distance hydrogen atoms.[35]

T_2 contrast agents

CAs shortening T_2 are called negative contrast agents because they let the tissue appear darker on the MRI scan.[35] For T_2-weighted imaging, superparamagnetic iron-oxide nanoparticles (SPIONS) are often used because of their high chemical stability, low toxicity and high magnetic moment.[29,31] The high magnetic moments enhance the alignments of the material with the external magnetic field. This way, they enhance the interaction with proton spins and decrease the T_2 relaxation time. Two iron oxides are considered: maghemite ($\gamma - O_3$) and magnetite (Fe_3O_4). The nanoparticles of these two types of oxides are superparamagnetic if they are smaller than approximately 30 and 25 nm respectively.[28]

Superparamagnetic relaxation is described by the outer sphere model only.

2.4   Brachytherapy

Brachytherapy (BT) is a treatment in which radioactive sources are placed near the tumor. By the insertion of the source near the tumor, this treatment can deliver high radiation doses without harming healthy tissue. Brachytherapy and external beam radiation therapy (EBRT) are the two types of radiation therapy clinically used. Although EBRT has taken a prominent role in the treatments option of cancer, the discovery of man-made radionuclides and the development of remote afterloading have renewed the interest in BT.[5] By using an ablative dose over a short period, the tumor can be attacked without harming adjacent organs. For the cancer treatment, this means a shortened therapy duration and lowered risk of reoccurrence, compared to conventional radio treatment, as well as reduced collateral damage and therefore faster recovery.[5,37]

Brachytherapy can be characterized by the dose rate, the positioning of the radionuclides and the duration of the irradiation. The dose rate differs from ultra-low-dose-rate (U-LDR 0.01-0.3 Gy/h) to high-dose-rate (HDR: > 12Gy/h). In between are low-dose-rate (LDR:0.4-2.0 Gy/h), pulsed-dose-rate: (PDR: 0.5-1.0 Gy/h) and medium-dose-rate (MDR:2-12 Gy/h). Concerning the positioning, the source can be applied inside the tumor (interstitially) or in contact with the tumor (intracavitary, intraluminal, endovascular, surface brachytherapy). For the duration of BT, there is a distinction made between permanent and temporal seeds. For the permanent implants, U-LDR and LDR are used and for temporary BT higher dose rates are used.[5,38,39]

Historically, permanent implants have been used a lot. However, better imaging techniques make individual cancer treatment with HDR and thus temporary treatment more interesting. As a result of better visualization of the tumor, the treatment and dose rates applied to the tumor can be personalized and an isodose treatment can be ensured. Furthermore, afterloading techniques reduce the health risks of using HDR. Using afterloading, sophisticated imaging modalities and computerized treatment planning make the HDR a very flexible and safe treatment.[40] A disadvantage of the HDR is the late tissue effects. PDR circumvents this problem by applying an MDR several times, while maintaining treatment advantages such as isodose optimization, planning flexibility and radiation safety.[38]

Conventional breast cancer treatment consists of breast conserving surgery, followed by EBRT. This treatment has great advantages over mastectomy and comes with good to excellent in-breast cancer control rates (95-100%). However, this treatment takes up to six weeks of daily EBRT treatment, which may lead some patient to refuse EBRT and opt for mastectomy. By using breast HDR BT instead of EBRT after a surgery, this duration can be reduced to 5 days only, while maintaining the treatment performance. Although the applicability of EBRT is higher than BT, this shows great possibilities for BT.[5]

Since breast cancer is more frequently diagnosed in the early-age stage, new treatment techniques are suggested to minimize the long-term treatment effects and lower the costs of the treatment.[4,6] Based on the same principles as early-state prostate research, permanent breast seed implants could be used to treat apply radio therapy to the tumor. By using seeds with NPs that are loaded with radiotherapeutic NPs which diffuse into the tumor, the treatment can be reduced to a 1-hour session to administer the seed. After this session the patient is free to go home and continue their day-to-day lives, because the sources are permanently implanted behind the skin. This reduces the treatment intensity for the patient and could decrease the cost for the hospital.[3,4,41]

2.5   Nanoparticle Design

Now that the applications of nanoparticles have been discussed, it is time to consider which type of NPs should be developed to combine all three applications. Although it is known that a combination of parameters is involved in the effectiveness of several applications, for simplicity, a list is made with tunable magnetic properties of fundamental importance per application and displayed in Table 3.

Table 3 Tunable magnetic properties and their applications.[42]

Tunable property	Application
Saturation Magnetization M_s	MRI, Hyperthermia
Coercivity H_c	Hyperthermia
Blocking Temperature T_B	Hyperthermia
Néel and Brownian relaxation time of nanoparticles t_N & t_B	MRI, Hyperthermia

Different synthetic techniques can be used to change the dominant parameters of the nanoparticles which influence these properties. The main parameters are the size, shape, composition and shell-core design. The effect of each parameter on the properties will now be discussed.

2.5.1 Size

The unique magnetic properties of nanoparticles can be attributed to the high surface-to-volume ratio.[42] The influence of the size on the magnetic properties has already been subtly discussed during the explanation about magnetic domains. Here a more elaborate explanation will follow. For the upper limit, M_s will increase with the size until a threshold size is reached beyond which M_s is constant and close to the bulk value. However, NPs have a disordered spin layer at their surface. For the lower limit, the contribution of this disordered layer increases as the size decreases. The magnetization M_s can generally be described by the eq (8).[43]

$$M_s = M_{sb}[(r-d)/r]^3 \qquad (8)$$

where r is the NP size, M_{sb} the saturation magnetization of the bulk and d the thickness of the disordered surface layer. This equation does not hold if the particles become so small that they get in the superparamagnetic regime. There the maximal M_s is reached. As the effect of the size on the coercivity is already explained, this will not be discussed here in any more detail. As already stated, it is hard to extract only one parameter as a function of a property. A good example is seen in the experiments of Guardia *et al.* and Salazar *et al.* Guardia shows that the M_s decreases with decreasing particle size and that particles below 17nm are in the single domain regime.[42] In the single domain regime, a decrease in magnetization is expected to be a result of the above described disordered layer. However, Salazar *et al.* argue that for particles below a size of 20 nm, the presence of an oxidized layer Fe_2O_3 on the surface of Fe_3O_4 means the NPs can no longer be classified as Fe_3O_4.[44] Due to an increase in low-magnetization maghemite Fe_2O_3 instead of high-magnetization magnetite Fe_3O_4 the magnetization will decrease. The decrease in magnetization for smaller particles can therefore be a result of the disordered layer or the maghemite contribution. This example of a complication of the size dependence is just meant as an illustration of how hard it is to predict the magnetic properties for different materials. For other materials, the oxidation state might not be a problem, or the

oxidation state could already impose a problem in the multiple domain regime and therefore not overlap with the single domain sizes.

For application in hyperthermia or thermal ablation, size is a critical parameter. Eighter hysteresis losses or Néel/Brownian relaxation processes will lead to heating. Which of these processes is dominant, is mainly dependent on the size. For small particles in the single or superparamagnetic domain hysteresis heating is negligible. For particles below 20 nm Néel relaxation is dominant and above 20 nm Brownian relaxations dominate.[45] Relevant studies show that for Fe_3O_4 with size below 7 nm[46] or 9.8 nm[47] no heating occurs. Furthermore, all research named in Kolhatkar *et al.* confirm the positive relation between the increasing size and the SAR value.[42,47,48]

SPIONs are T_2 contrast agens and therefore affect transverse relaxivity. The size of the particle governs the transverse relaxivity via the magnetic moment as described above and via the operative diffusive regime. For very small particles (below 30nm), it is more likely for the particles to be in the motional averaging regime (MAR). This is also called the outer-spere regime as explained for T2 contrast agents like SPIONS. In this regime, the relaxivity is linear with the diffusion time and quadratic with the magnetic moment.[30] Bigger particles are in the static dephasing regime (SDR). In this regime, the diffusion can be neglected and the relaxivity is linear with the magnetic moment. The relaxivity is maximal in the SDR. For big particles, the refocusing of the transverse magnetization may become inefficient and the relaxivity decreases for increasing diffusion time. The diffusion regimes and the transversal relaxivity as a function of particle diameter are displayed in Figure 9.
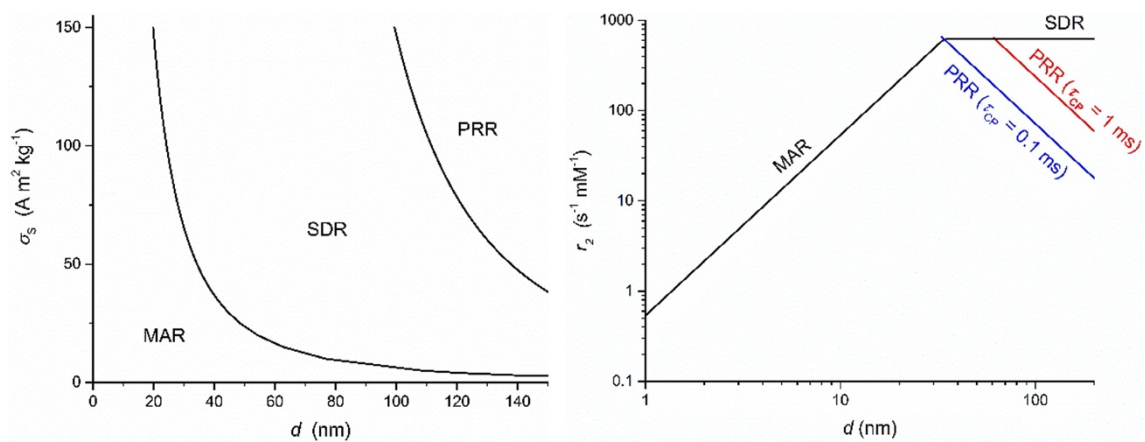
Figure 9 Diameter dependence of a) Saturation magnetisation per unit mass and b) the transverse relaxivity. Both images distinguish the different regimes.[42]

2.5.2 Shape

Increasing the particle size will not always lead to symmetric spherical growth. A lot of research has been done on the influence of NP's shape on the magnetic properties. Previous research shows, that cubic NPs have a higher M_s than spherical NPs with the same volume.[49] A simulation of the magnetic spin structures for spherical and cubical particles demonstrates that the lower M_s is a result of more disordered spins. The simulations by Noh *et al.* showed that the disordered spins of a spherical particle contributed for 8%, whereas for cubic NPs they only contributed for 4%.[50] Although some research points out certain relations as described above, no conclusive statements can be made due to the many influencing parameters in NPs.[42]

Figure 10 Simulation by Noh et al. from the spin alignments at the border of spherical (a) and cubic (b) particles.[50]

The effects of cubical particles instead of spherical particles however, have been shown for different applications. Research has shown that the relaxation time is four times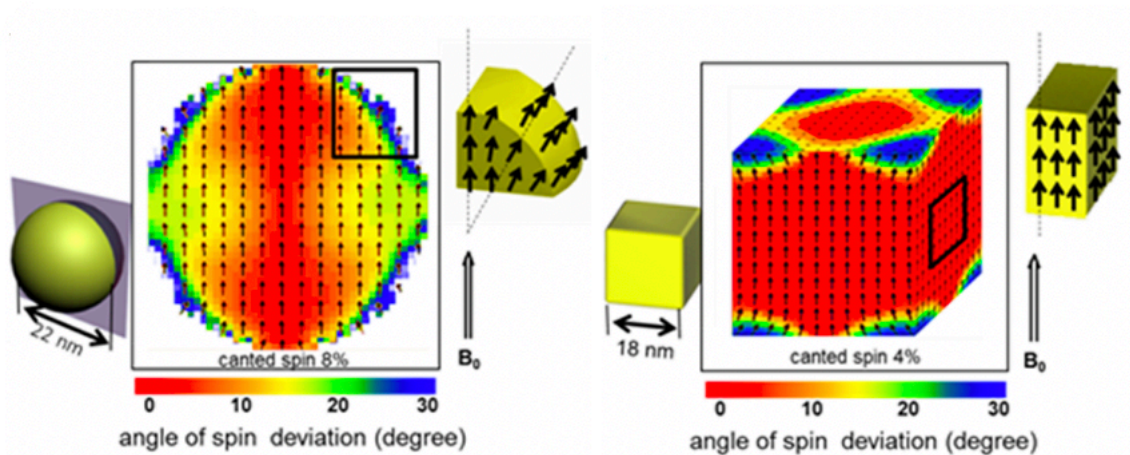 smaller for cubical Fe_3O_4 particles compared to spherical ones. Researchers attributed this increase in relaxivity to better crystal structure of Fe_3O_4 in cubical NPs.[49]

For hyperthermia applications, Guardia *et al.* and Noh *et al.* reported very high SAR values of 2452 W/g and 4060 respectively.[50,51] Guardia used cubical 19 nm Fe_3O_4 at 520 kHz and 29kA/m. Noh *et al.* used $Zn_{0.4}Fe_3O_4$ nanocubes of 40 nm measured at 500 kHz with 37.4 kA/m. Based on limited studies, no hard conclusions can be drawn about which shape is best for heating applications. However, NPs with flat surfaces appear promising.[42]

2.5.3 Composition

The most important parameter determining the magnetic properties of a material is the composition. The magnetic properties arise from the presence of unpaired electrons on metal atoms as described in the magnetism chapter. The orientation of the magnetic moment of these unpaired electrons defines the eventual magnetic behavior. For example, Fe_3O_4 which is actually $Fe^{2+}Fe_2^{3+}O_4$ where Fe^{3+} has 5 unpaired electrons and Fe^{2+} 4 unpaired electrons. One Fe^{3+} and one Fe^{2+} will occupy the octahedral sites and the final Fe^{3+} will occupy the tetrahedral sites which are left. The magnetic spin structure of several iron oxides is displayed in Figure 11and gives a net magnetic moment. It can be seen from this example that the eventual magnetic moment is not straightforward and that a lot of things can be tuned.

Several research groups are occupied by the research on the effect of dopants (M) on the magnetic properties of ferrites (MFe_2O_4). Improved saturation magnetization can be found by incorporating Mn^{2+} in the ferrite structure obtaining $MnFe_2O_4$. Since Mn^{2+} has a higher magnetic momentum, replacing the parallel Fe^{2+} with Mn^{2+} will increase the total magnetization. Further research on the spinel structures showed that Mn has a mixed spinel structure in contrast with other transition metals like Co, Ni and Fe. This means that for $MnFe_2O_4$ both Mn^{2+} and Fe^{3+} will occupy the tetrahedral sites which are only occupied by Fe^{3+} for the other metals.[42,52] This is shown in Figure 11.
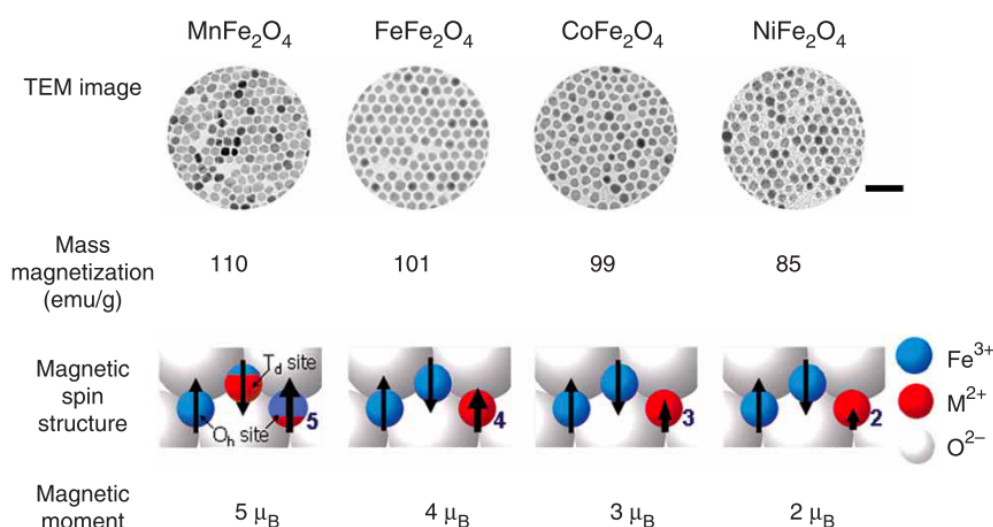
	MnFe$_2$O$_4$	FeFe$_2$O$_4$	CoFe$_2$O$_4$	NiFe$_2$O$_4$
TEM image				
Mass magnetization (emu/g)	110	101	99	85
Magnetic spin structure				
Magnetic moment	5 μ_B	4 μ_B	3 μ_B	2 μ_B

Figure 11 The spin structure of transition metals with the corresponding magnetic properties that come with this structure.[52]

2.5.4 Coating

The surface of NPs for medical application is typically decorated with a layer of long-chain organic molecules. Such coatings are applied to make NPs biocompatible and colloidally stable in physiological solutions or to provide a modified surface for functionalization such as targeting.

Since the saturation magnetization is value per gram of material, adding non-magnetic coating will always decrease this value. Although future developments may enable the use of magnetic coatings, which could contribute to the total magnetic properties and with that increase the SAR, research shows that coating often trades enhanced biocompatibility for reduced magnetic properties. This is mainly an effect of surface spin effects.[42,53]

In general, the thickness of the coating reduces the relaxivity and therefore the contrast of an MRI. However, it has been proven by Ye *et al.* the contrast can be enhanced by adding coating, if the r_1 relaxivity decreases more than the r_2 relaxivity and therefore the r_2/r_1 ratio increases.[54]

2.6 Holmium Doped Super Paramagnetic Iron Oxides

As described in the previous chapter, the composition of a material is very important for its magnetic properties. It is explained why the magnetization of a nanoparticle can be increased by exchanging a low magnetic moment Fe^{2+} ion, with a high magnetic moment Mn^{2+} ion. A lot of promising research on the doping of iron oxide nanoparticles with transition metals has already been done.[12,42,52] However, rare earth (RE) elements such as lanthanides can even be more interesting because of their higher magnetic moment.[12,55] This chapter will explain the potential of holmium as a dopant in SPIONs.

The unique properties of lanthanides originate from their 4f electrons. The 4f shell for lanthanides can contain up to 7 unpaired electrons. Furthermore, the 4f shell has higher spin-orbit coupling than the 3d shell for transition metals.[12,56] High spin-orbit coupling leads to higher magnetization and therefore, doping iron oxide nanoparticles with lanthanides may improve the magnetic properties and oxidation resistance.[12,57,58]

Research mainly reports a decrease in saturation magnetization for the introduction of lanthanides into the crystal structure. This decrease may be attributed to a lot of factors, but it is shown that the magnetic properties are mainly dependent on the concentration of lanthanide in the NPs. Huan *et al.* and Meng *et al.* explained that for certain concentration differences the saturation magnetization would increase due to the preferred occupied positions of lanthanides in the crystal structure.[12,57,59] Like Mn, Ho might also replace Fe ions inside the lattice structure of Fe_3O_4. If the lanthanides are substituted on the octahedral site more than on the tetrahedral site, their high magnetic moment will contribute to the increased net magnetization.

To maximize the magnetization, the element with the maximal magnetic moment should be chosen. From Table 4, it can be seen that Dy and Ho have the highest magnetic moments. For this research, Ho is chosen as a more interesting candidate because it has a radioisotope, ^{166}Ho, which decays under emission of β-particles and γ-radiation. It has a convenient half-life time of 26.8h.[19] The β-particles have a penetration depth of 3.2 nm, which makes it a good source for radionuclide therapy.[17,18,60] Moreover, the γ-radiation radiation could be used for SPECT. The high magnetization makes Ho a good T_2 MRI contrast agent and makes it supposedly applicable for heating purposes. Another preferable feature of Ho in contrast to iron-oxides, is that lanthanides do not show saturation in magnetization for high magnetic field. Therefore, for increasing magnetic field, the MRI contrast grows.[6,14,61]

Table 4 Electron configuration in the 4f shell and the magnetic moment of lanthanides.[31]

Lanthanide metal ion	Configuration (4f)	Magnetic moment
Eu^{3+}	↑↓ ↑ ↑ ↑ ↑ ↑ ↑	3.4
Gd^{3+}	↑ ↑ ↑ ↑ ↑ ↑ ↑	7.94
Dy^{3+}	↑↓ ↑↓ ↑ ↑ ↑ ↑ ↑	10.65
Ho^{3+}	↑↓ ↑↓ ↑↓ ↑ ↑ ↑ ↑	10.60

2.7   Spark Ablation

The growing interest in NPs emerges the search for new synthetic methods. The biggest challenge in NPs production at the moment is the tradeoff between the throughput and the control of the size distribution.[62–65] The most common synthesis route is wet synthesis, which allows fine-tuned NP production.[65,66] However, slow kinetics and batch type operations inhibit the scalability of the wet synthesis.[64] Moreover, these batch operations lead to a variety of physicochemical properties and need several chemicals for the synthesis of one type of NPs. This results in impurities in the NPs and chemical waste for the environment, which are both undesirable.

Another NPs production method is based on spark ablation, which is a simple process with a low amount of variables resulting in a reasonable yield.[67–70] Moreover, the method allows high surface purity, which is especially important for NPs because they have a high surface-to-volume ratio.

In this research, the VSP-G1generator from VS-Particle is used.[71] The VSP-G1 is a Spark Discharge Generator (SDG) which consists of two electrodes placed in a chamber and separated by a gap. A shunted capacitor and a high voltage generator are connected parallel to the electrodes. When the capacitor is charged, a spark discharges over the gap between the electrodes, material from both electrodes evaporates in a form of particles that form aerosols. The particles that are created initially form primary particles and the size of these particles defines the properties of the final material.[72] The primary particles are then transported by the carrier gas (typically N_2) into a gas bubbling column containing water, where the particles are accumulated.

Two phases of particle formation can be distinguished for this method: formation of the vapor and condensation of metal vapor to NPs. The formation of the vapor is controlled by two variables: the current I(mA) and the voltage U(V).

The current influences the yield of the generator because it selects the frequency with which sparks occur. The relation between the spark frequency (f), the current (I), the capacitance (C) and the discharge voltage (V_d) is given by eq (9).

$$f = \frac{I}{CV_d} \tag{9}$$

From this frequency, it can be seen that maximal current and low voltage lead to maximal yield and vice versa. However, the yield also depends on the amount of material ablated per spark, which in its turn is dependent on the energy per spark. The energy of each spark is mainly determined by the discharge voltage via eq (10):

$$E = \frac{1}{2}CV_d{}^2 \tag{10}$$

The discharger voltage is depending on the breakdown voltage V_b of the carrier gas and an uncertain overvoltage V_o.[67] Because the overvoltage is unpredictable the actual discharge voltage will fluctuate and so will the energy per spark and the frequency.
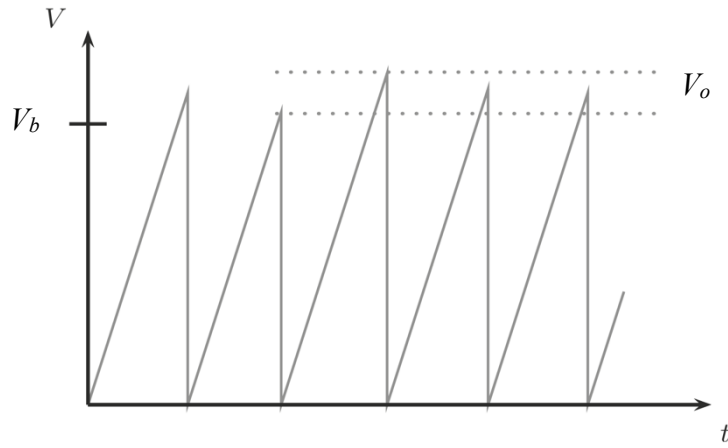
Figure 12 Voltage over the spark gap as a function of time.[30]

More energy leads to more material that can be vaporized per spark but also alters the size of the particles. For the VSP-G1 generator, a 20 nF capacitor is used. The flow rate can be set between 0 and 5 L/min. The current will be between 0 and 10 mA and the voltage can be set between 0 and 1.3 kV

Although the generator uses the voltage as a parameter, it is the distance between the electrodes that is changed when changing the voltage. Since the discharge voltage is a function of the choice of carrier gas and the distance between the electrodes, the voltage is controlled during the experiment by changing the gap distance. This leads to a steady voltage even though the electrodes are changing in size due to ablation. In the setup, N_2 is used as carrier gas because of its low ionization energy and low thermal conductivity, which results in the highest breakdown voltage and biggest particles.[70] In Figure 13 the relation between gap distance, quenching gas and breakdown voltage is displayed.
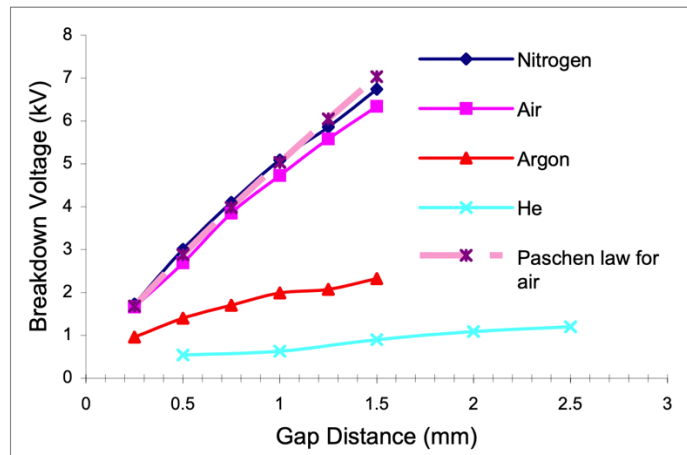
Figure 13 Effect of gap distance and choice of carrier gas on the breakdown voltage.[70]

When the vapor is created, a flow with quenching gas will carry the particles out of the reaction chamber. The evaporated material will lose its heat to the environment and nucleate into stable particles.[67–69] These stable particles are the first primary particles and range in size from 1 to 9 nm, depending on the evaporated material and the sparking conditions.[69,73–80]

Because of the high concentration of primary particles inside the gas chamber and transport tubes, the particles will collide. This will lead to coalescence and agglomeration. As long as

the temperature is above the melting temperature of the nanoparticles, the particles can coalesce easily.[81] Because the system loses energy to the environment, the temperature decreases for particles being away from the generator. Furthermore, the melting point increases for increasing particle size.[82] If the particle's temperature decreases below the melting point, a less trivial path of coalescence is taken. By coalescing, the total surface area is reduced and therefore the surface tension decreases. This decrease in surface leads to a release of heat which can be used for coalescence. In other words, there is a mechanism where coalescence accelerates itself by releasing surface tension.[83] However, as a result of decreasing temperature and increasing melting point, there is still a maximal primary particle size, which this system can reach. The maximal primary particle size in the system depends on the material used. Below the maximal primary particle size, the voltage, current and flow can be adjusted to decrease the primary particle size. When the particle temperature decreases, the particles will stick together and agglomerate.

Another way to explain the completeness of coalescence is to assume that the coalescence time is inversely exponentially dependent on the temperature of the particle and therefore, for low temperature the coalescence time is shorter than the collision time leading to partial coalescence only. This is summarized in Figure 14.
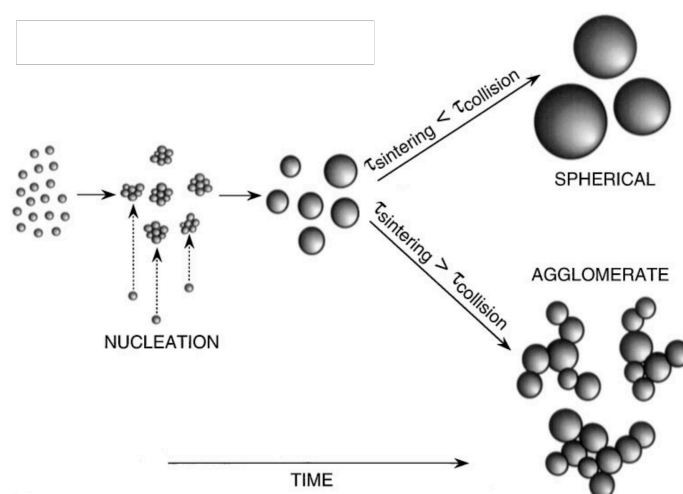

Figure 14 Primary particle and aggregate formation in the SDG.[84]

Apart from the voltage and current, the flow rate over the gas chamber can be adjusted. The flow rate has a more complicated effect on the primary particle size than the voltage and current. The flow rate determines the time the particles spent in the sparking chamber and tubing leading to the bubbling column. Since a low flow rate means the primary particles spend more time inside the sparking chamber and tubes before being collected, the particles have more time before being cooled down and have more time to collide with other particles. This leads to larger particles but also to a broader size distribution.[69] Tabrizi *et al.* concluded that at a flow rate above 5 L/min, the particle size will be constant.[70] Furthermore, the flow rate also affects the yield. If not all the particles are removed from the spark chamber between successive sparks, ablated material will accumulate inside the reaction chamber and will not reach the bubbling column.

2.7.1 Bimetallic Nanoparticles

For the creation of particles with different electrode materials, the particle creation is more complicated. The negative electrode in G1-generator is eroded more strongly than the positive electrode. This is a result of the fact that the majority of charge carriers in the plasma are positive ions and electrons. The positive ions have a higher mass than the electrons and therefore more kinetic energy. The positive ions are accelerated towards the negatively charged electrode and the negative electrons are accelerated towards the positive electrode. The heavy ions are able to ablate more material than the light electrons.[70] To make sure both electrodes ablate, temporary voltage reversal is necessary. The system is designed so that it resembles an RLC circuit with a damped oscillation character as displayed in Figure 15.[70,85] As a result of the oscillation behavior of the voltage, both electrodes act as an anode and cathode and will both ablate.
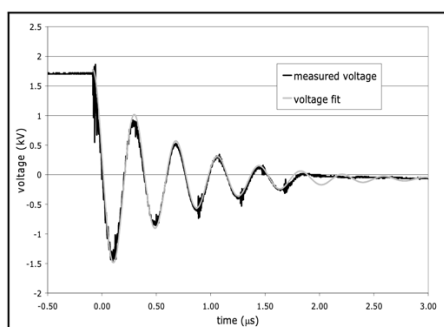

Figure 15 Damped oscillation behavior of the system, which acts as an RLC circuit.[70]

However, since the oscillation is damped the first electrode acting as anode will ablate less. The damping effect is clearly illustrated by Tabrizi *et al.* in an experiment that changed the material of the electrode which acts as the anode. The results of this experiment are shown in Table 5.

Table 5 Average composition of Pd-Au samples measured by ICP (reproduced from Tabrizi et al.[70]

Electrodes	Pd/Au weight ratio in the sample
Au(+)Pd(-)	0.58
Au(-)Pd(+)	0.34

The amount of ablated material is also a function of the different melting and boiling properties of the materials. The ratio at which the materials will occur in the sample will therefore differ for every electrode combination.

2.8   Bubbling Column

For medical applications, the created nanoparticles need to be in aqueous suspension.[86] Therefore, the typical accessories designed by VSParticle to depose the nanoparticles on solid supports are not applicable. To capture the nanoparticles in water, a new method should therefore be developed. As investigated by Sharaf during his internship with VSParticle the best solution is to use a bubbling column.[68]

Unfortunately, not much research has been done on the use of bubbling as a technique to extract particles from a gas flow. Most data available on the bubbling of gas with NPs concerns purification of the gas rather than NP capture in water. Although the goal is different, the physical principles are similar enough to establish a model of the extraction efficiency that can be used for this research. In this chapter, a brief model of the absorption efficiency inside will be given, based on the previous research.[68,87–89]

In a model first explained by Fuchs,[90] three different mechanisms are distinguished: Brownian diffusion, inertial deposition or gravitational settling. The dominant deposition mechanism is determined by the particle size. As can be seen from Figure 16 Brownian diffusion is the dominant mechanism for NPs with a size below 400nm. In this research, the focus is on particles below 100 nm and therefore only the diffusion mechanism will be considered.
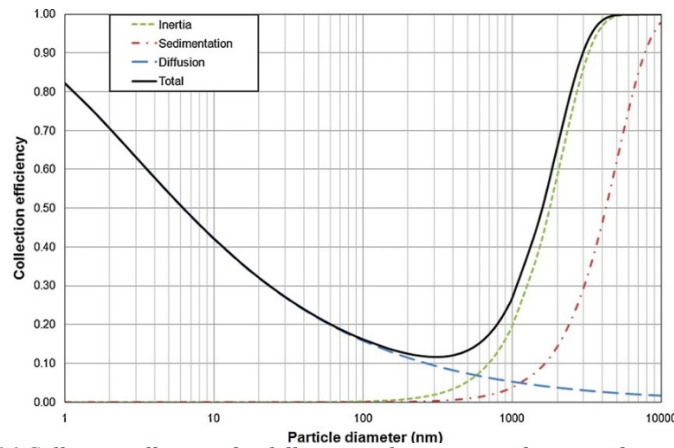

Figure 16 Collection efficiency for different mechanisms as a function of particle size.[88]

A very common way to describe the absorption efficiency is as follows:

$$\eta = \frac{C_{p0}-C_p}{C_{p0}} = 1 - \frac{C_p}{C_0} = 1 - e^{-ah} \tag{11}$$

where C_{p0} is the concentration of particles inside the gas that is inserted, C_p is the final concentration, a is the absorption coefficient, and h is the height of the bubbling column. The absorption coefficient a is given by eq (12), were D is the particle diffusion coefficient (eq (13), U_b is the bubble rising velocity and r_b is the radius of a single bubble (eq(14)).

$$a = 1.8 \left(\sqrt{\frac{D}{U_b r_b^3}} \right) \tag{12}$$

$$D = A \frac{T}{r_p} \tag{13}$$

$$r_b = 0.5 * \left[\left(\frac{6d_0\sigma}{\rho_l g} \right)^{\frac{4}{3}} + \frac{81v_l Qo}{\pi g} + \left(\frac{135Q_o^2}{4\pi^2 g} \right)^{\frac{4}{5}} \right]^{\frac{1}{4}} \tag{14}$$

From D it is again possible to see the inverse diffusion efficiency for increasing particle radius as it could be seen in Figure 16.

As can be seen from these equations, the main parameters affecting the efficiency are the height of the bubbling column and the bubble radius which is a direct translation of the gas flow rate and the viscosity of the water. These equations have been validated in the research by Charvet and Cadavid-Rodriguez.[88,89] They proved that an increase in height of the liquid inside the bubbling column indeed leads to an increase in absorption efficiency. Furthermore, they showed that an increase in flow rate and therefore an increase in bubble size resulted in a decrease in absorption efficiency. Both theoretical explanations and empirical findings can be intuitively explained. Increasing the liquid height increases the residence time of the bubble and with that the time for the particles to diffuse. By increasing the bubble radius, the area/volume ratio through which diffusion can take place is decreased and hence the diffusion. However, Charvet found an inconsistency in this model for which the absorption efficiency increases with a higher flow rate. This is a result of micro-bubble formation which comes with turbulent flows. The microbubbles' extremely high area/volume ratio compensates for the decreased Area/Volume ratio from the turbulent flow.

For the bubbling column design, a micro-bubbler suitable for the generation of appropriately small bubbles is needed. Furthermore, the liquid height should be maximized while preventing the bubbles from reaching the top.

3   Experimental

3.1   Experimental Method

The experimental set-up used for nanoparticle production and deposition is shown in Figure 17. Nitrogen was used as the inert carrier gas. The Brockhorst gas flow was controlled with a 0-25 L/min flow controller and a pressure sensor limits the pressure to 1.4 mbar.[91] When 1.4 mbar is reached, the flow will shut off. The gas was led through the VSP-G1, where two electrodes of eighter 99.99% Fe or both 99.99% Fe and 99.99% Ho were placed perpendicular to the gas flow. The gas flow, system pressure, current and voltage was controlled from the VSP-computer.
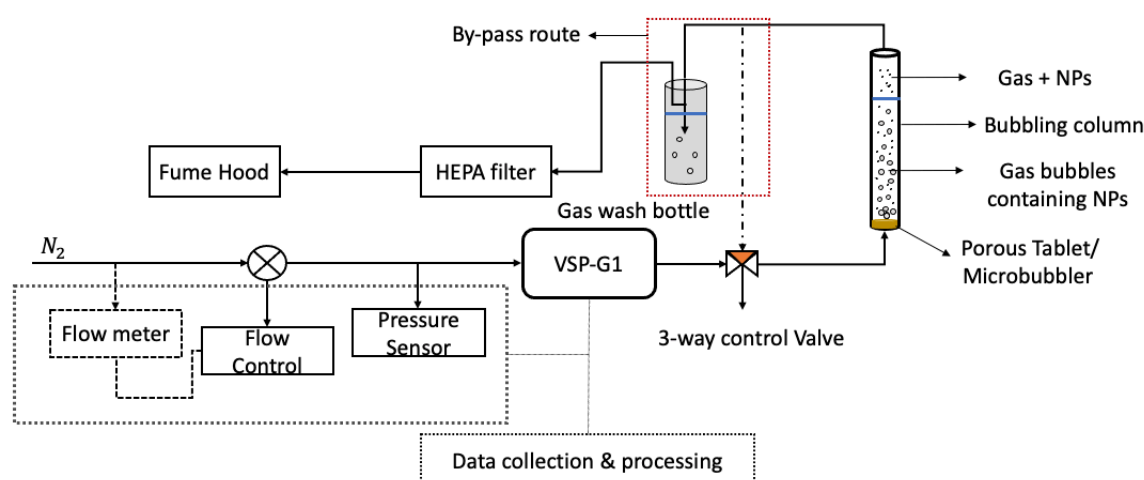

Figure 17 Schematic representation of the experimental set-up used in this project for NP production and deposition (produced by Meghana Amaregouda).

From the generator, the gas with nanoparticles was led to a 3-way control valve, which prevents the water from flowing back from the bubbling column to the generator. If the valve was closed, the gas with NPs flowed directly into the gas wash bottle via the by-pass route. Otherwise, the gas with NPs flowed to the bubbling column where microbubbles were created using a micro-bubbler and the particles diffused from the bubbles into the water. A bronze sintered porous tablet with a pore size of 0.04-2 μm was used as a micro-bubbler.[85] The gas and NPs that did not get collected, went through the gas wash bottle and the HEPA filter. The HEPA filter took out the NPS and the pure nitrogen gas was disposed in the building's ventilation system.

Before every experiment, the bubbling column is filled with miliQ water. After every experiment, a sample from the bubbling column was taken. If many particles got stuck on the micro-bubbler, a sonicator was used to collect them. Every time the electrodes were changed, the sample from particles left inside the generator was collected. This powder sample was used a lot because this was the easiest way of getting a high concentration sample.

3.2 Characterization Techniques

Below, all characterization techniques are explained. More background information on the techniques used is provided in Appendix C

Dynamic Light Scattering (DLS)

The AVL Goniometer, AVL-5000 correlator and the Perkin-Elmer photo counter were used in DLS setup. The laser with a 633 nm wavelength was placed at a 90° angle with the detector. The measurement was analyzed with AVL-5000 software using a CONTIN regularization with 150 grid-points. The DLS sample was diluted when the count rate was >1250 kHz and is optimally brought to 500kHz.

For the DLS sample, a DLS tube was filled with 2 ml pipetted from the column and micro-bubbler samples. For the filtered samples, a 400 nm syringe filter was used. For sonication of the sample, the Cole Parmer Ultrasonic Processor (750-Watt, 20 kHz) was used, sonicating the sample for 2 min with 20% of the amplitude.

Transmission Electron Microscopy (TEM)

A JEOL JEM-1400 plus Transition Electron Microscope (TEM) operating at an accelerating voltage of 120 kV was used to determine nanoparticle core size and shape. To perform a TEM image, a droplet of sample was applied on the TEM grid and dried. To verify the primary particle size, ImageJ was used to measure several particle sizes and take the average.[92] The calculations are shown in the Appendix B.1.

X-Ray Diffraction Spectroscopy (XRD)

For the XRD measurement, the Malvern Panalytical X'pert Materials Research Diffractometer is used with a copper X-ray tube. It was operated at a voltage of 45kV and 40 mA. For the XRD measurement, the generator's residue powder was placed inside an airtight sample holder to prevent the monochromator's ventilation system from blowing the particles away. The XRD measurement was executed with a Cu X-ray tube, for angles 10-90 with a step size of 0.008 °2θ and a measurement time of 5 hours. The measurement was repeated 10 times to improve the signal-to-noise ratio.

Inductively Coupled Plasma Optical Emission Spectroscopy (ICP OES)

For the ICP measurement, the PerkinElmer Optima 5300 is used. The samples were analyzed with the ICP-OES 5300DV. The calibration for Ho is done with for concentrations 1.00, 1.89 3.97 and 7.89 mg/L. The calibration for iron is done with concentrations 1.00, 1.80, 3.96 and 7.91 mg/L. The calibrations are displayed in Appendix B.5. The ICP measurement was repeated 3 times and the average value was used.

ICP is done on the samples from the column and the particles captured before the micro-bubbler. 5 mL of each sample was added to 1.5 mL nitric acid to dissolve the particles and perform ICP on it. To make sure all particles are dissolved, the samples are microwaved before ICP is performed.

Scanning Electron Microscopy (SEM) & Energy Dispersive X-ray (EDX/EDS)

The JEOL JSM-IT100 device was used to perform SEM-EDX. The Sample was prepared by applying a 0.5 mL droplet of the column or micro-bubbler sample on the carbon tape and letting it dry. The SED and HV setting were set at 7kV and x40, respectively. These where increased if the count rate was below 1000 cps. The EDX measurement was run for 1.5 h.

Mössbauer Spectroscopy

Transmission [57]Fe Mössbauer spectra were collected at 300 K with a conventional constant-acceleration spectrometer using a [57]Co(Rh) source. The data is analyzed by the Mosswinn software.[93] The sample is prepared by combining all Fe-Fe residue powder from the generator until 50 mg was reached.

Superconducting Quantum Interference Device (SQUID)

A Quantum Design VSM detector module was used for the NP's magnetic characterization. The measurements were done for -300 to 300 Oe and -30000 to 30000 Oe at T = 300K. For the liquid sample 1 mL was inserted in the VSM-sample holder and for the powder sample 1 mg was inserted in the sample holder.

Nuclear Magnetic Resonance (NMR)

The 400MHz Agilent NMR spectrometer was used to perform the measurement. An inversion recovery pulse sequence was used to obtain the T_1 measurement and a CPMG pulse sequence was used for T_2. One scan was performed for all measurements. The frequency used was 400 MHz. The measurement was performed at T = 298 K.

5 mL of sample from the column and micro-bubbler was pipetted into the NMR tube. To obtain the relaxation times, the measured data was fitted to the equations in Figure 6.

Heating measurement

The magneTherm[TM] digital device was used for the heating experiments of MNPs. different frequencies in the range from 50 kHz – 730 kHz were used. The magnetic field of the device is limited by 25 mT. The measurements were started 60s before, 60 s during and 60 s after applying a magnetic field. Different frequencies were tried.

For the heating measurement 1 mL sample is used. The filter sample of E33 is used and a powder sample from the generator diluted into water is used after sonicating.

4   Results and Discussion

In this chapter, the results of the spark ablation synthesis and the characterization of the Ho-doped SPIONS are given and discussed. The first part will give a summary of the steps taken in order to characterize and improve the NP production. The second part will compare the eventually produced Ho-doped SPIONS with undoped SPIONS. The logbook with all settings used for the experiments can be found in Appendix A

4.1   Spark Ablation

4.1.1   Particle Size

There is little experience with the combination of the VSP-G1 generator and the bubbling column to extract the NPs. Only Sharaf *et al.* has produced limited data on the bubbling column collection so far.[68] Therefore, his approach was used as a basis to find out an appropriate method. Before making Ho-Fe particles, Fe-Fe particles were made to get more knowledge about the production of particles with respect to the settings.

In Table 6 the setpoints and results from Sharaf's experiments are shown. Sharaf used a bubbling column filled with 10 cm of water and the same generator. Sharaf *et al.* used argon as carrier gas instead of nitrogen, which was used in this research. This should give him smaller particles because of the shortened mean free path and lower thermal conductivity of argon compared to nitrogen.[69]

Table 6 The selected setpoints and results for particle production and particle capture inside a bubbling column of Sharaf et al.[68]

Voltage (kV)	Current (mA)	Gas Flow Rate (L/min)	notes
1	5	1	Gives a moderate4 number of particles with a peak of 25-30 nm.
1	5	2	Gives a moderate4 number of particles with a peak of 15-20 nm.
1	7.5	2	Gives a large number of particles with a high peak.
0.7	2.5	2	Gives a relatively small number of particles with a peak of 12-15 nm.

DLS and TEM measurements were done to obtain information about the particles size and distribution and compare it to the results of Sharaf. The calculations are given in Appendix B.1.

Particle Aggregation

E12, E13 and E15 were all done for V = 1kv, I = 5 mA, F = 2L/min. DLS measurements gave the minimal peak at 17.20 nm, 32.45 nm and 4.80nm respectively. However, when comparing the TEM images, it could be concluded that the primary particles were all approximately 4 nm. These differences measured by the DLS can be explained by aggregation. The time between the experiment and the DLS was 6, 24 and 1 h, respectively. This illustrates that the experiment

particles will aggregate over time to confirm the aggregation, a DLS measurement was done for 67 h. The count-rate of this measurement showed an increasing trend (Figure 19), and since bigger particles scatter more light, this increasing count rate was assigned to agglomeration. This agglomeration is in line with literature.[64,70]
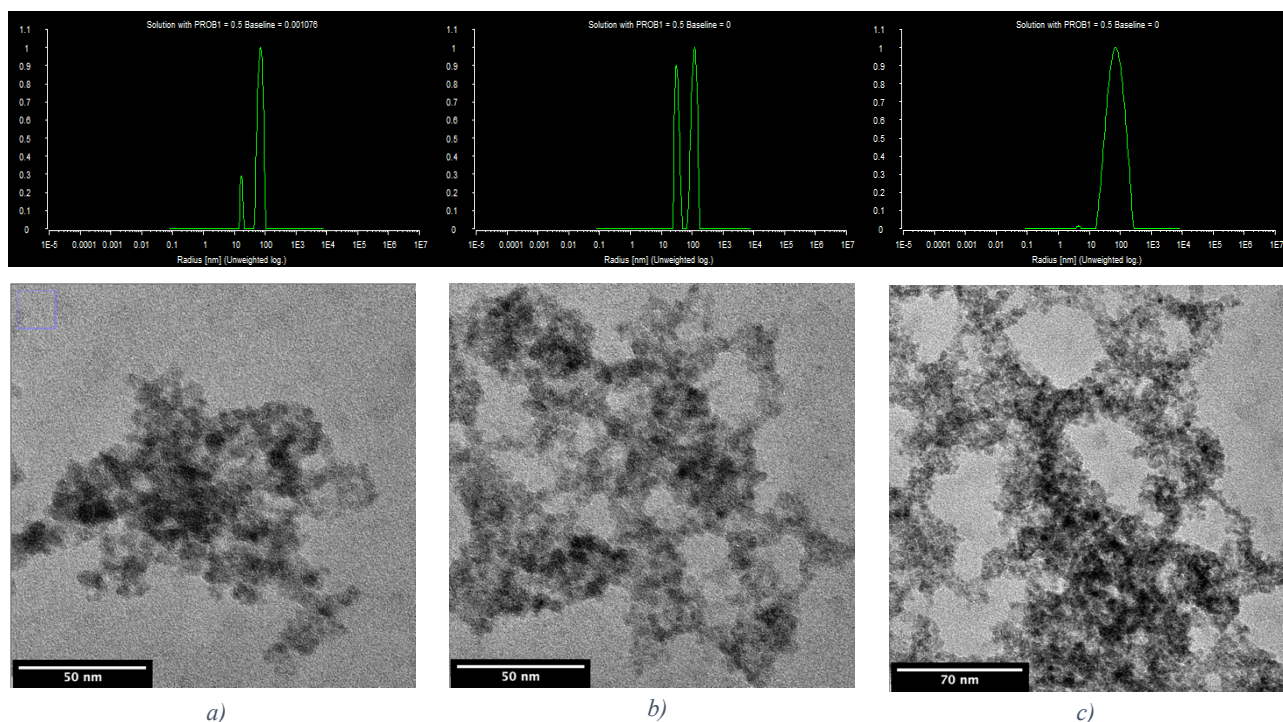

Figure 18 Size determination using DLS and TEM of a) E12, b) E13 and c) E15. DLS measurements give the first peaks for 17.2, 32.45 and 4.80 nm respectively. From all TEM images a primary particle size of 4nm was found.

To decompose the aggregates, the sample was sonicated. However, the aggregation increased as a result of higher collision frequency under exposure of an ultrasonic field.[94] From these experiments it could be concluded that aggregation takes place and that the DLS measurement should be done directly after the experiment, or aggregation has to be taken into account for the DLS measurement.
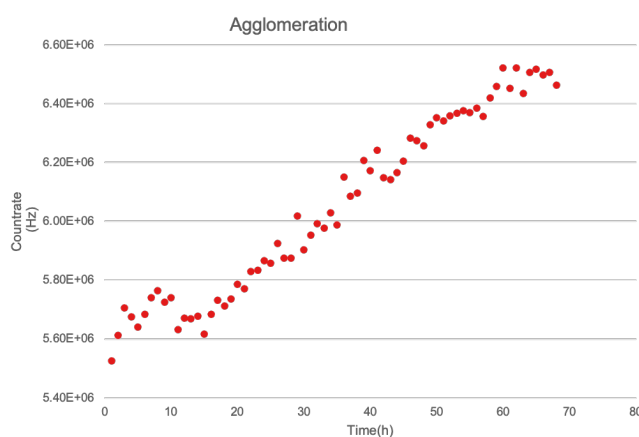

Figure 19 Count rate of the 67h DLS measurement, showing increasing count rate and thus agglomeration.

Maximal Primary Particle Size

From E12, E13 and E15 it was seen that for V = 1kV, I = 5 mA, F = 2L/min, 4 nm NPs were produced. Sharaf *et al.* measured 15-20 nm NPs for these settings. Figure 20 shows the size distribution as a function of generator settings provided by VS-Particle, where a) shows the data for argon and b) for nitrogen. Figure 20a predicts the measured particle size for Sharaf *et al.* to be 12-14 nm and for this research particles >12 nm were expected (Figure 20b). It could be concluded that the effect of the generator settings on the particle size did not correspond between Sharaf *et al.*, VS-Particle or this research. Therefore, the settings had to be established for the set-up from this research in particular.
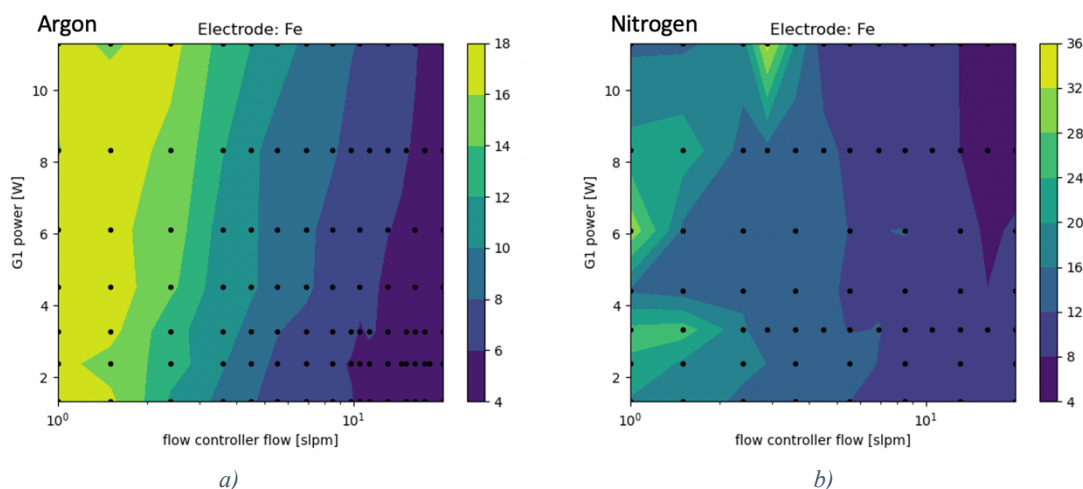

Figure 20 Size distribution of G1-generator spark ablated iron NPs for a) Argon and b) Nitrogen as carrier gas,

To increase the particle size, minimal flow and maximal current and voltage are selected. For E20, the voltage, current and flow were set at 1.3 kV,10 mA and 0.5 L/min, respectively. These setting theoretically produced the biggest particles the generator could achieve. However, from TEM it appeared that still particles of 4 nm were produced (Figure 21). Nevertheless, these sizes are in line with the available literature, which suggests that the peak size is expected to lay between 1-9 nm.[69,73–80] Further discussion with VS-Particle led to the conclusion that the generator would not be able to create Fe NPs with a size bigger than 4 nm.
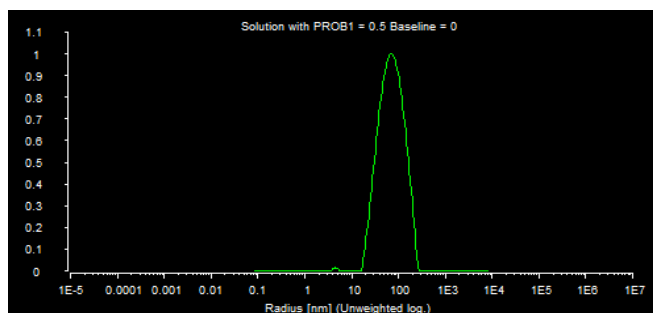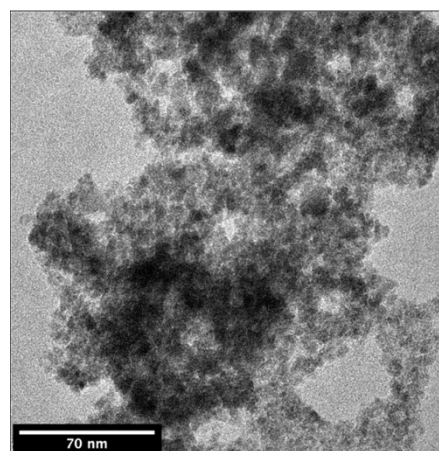
Figure 21 DLS chromatogram of (a) of E22 showing peaks at 9 nm and 90 nm; b)TEM image showing a 4 nm particle agglomeration

31

4.1.2 Yield

During experiments 1-21 the goal was to find out whether the generator settings affected the primary particle size, which happened not to be the case. Therefore, the best settings were considered the ones leading to the highest yield. This paragraph will explain the measures taken in order to maximize the yield.

Generator settings

For E22 and subsequent experiments the current was set to 10mA. For E22-25, the voltage was set on 0.65kV, but because of unsteady sparking, this was later increased to 1.3kV. The flow rate was set at 0.3L/min for experiments 22 and 23 to test if lower flow rate would result in smaller bubbles and therefore more diffusion of particles into the bubbling column. Since this was not true, it was later set to 3L/min for experiment 25 to see if a higher flow rate would take more particles from the sparking chamber into the bubbling column for diffusion. This did not make a difference either and therefore, from experiment 26 on, the flow rate was set at 1L/min.

Bubbling column volume

Since the yield is also highly dependent on the water volume present in the bubbling column, the water volume was increased to 200mL for experiments 22-25. This increased the absorption efficiency, as can be calculated by eq (11). Because the absorption efficiency was still. low and the volume was doubled, the concentration decreased. To increase the concentration, E21 and E22 were run for two consecutive days, but the concentration was still below the desired concentration. For E36 and E37 a bubbling column volume of 60 mL was used. This resulted in high concentrations. It may be concluded that the diffusion of NPs into the water happens in the low part of the bubbling column and increasing the volume will only lead to lower concentrations.

Micro-bubbler

The micro-bubbler used by Sharaf *et al.* did not let through enough air, resulting in pressure built-up at higher flow rates. If the pressure increased above 1.4 mbar, the system shut down. Therefore, instead of the micro-bubbler used by Sharaf, a metal mesh with great pore sizes was used. This deteriorated the bubble formation as can be seen from Figure 22a and b, because of the big pore sizes. In order to improve the bubble formation, four meshes were stacked on each other. This improved the bubble formation to some extent as can be seen in Figure 22 c). Nevertheless, the particle capture efficiency inside the bubbling column did not increase and the capture efficiency inside the mesh increased drastically (Figure 22 f). Therefore, the use of a mesh was abandoned.

To improve the bubble formation, porous tablets were then used. The tablets were composed of sintered bronze and stainless steel and had a pore size of 0.4-20 µm and 20 µm, respectively.[95,96] Both porous tablets have great bubbling formation (Figure 22 d and e) and increased the particle capture efficiency inside the bubbling column. Unfortunately, they captured many particles before entering the bubbling column as well. The stainless-steel tablet showed a severe pressure increase after three experiments, as illustrated in Figure 23. After the second experiment, the tablet was cleaned using an ultrasonic bath which helped to keep the pressure low for a little longer. However, after 30 min the pressure built-up changed drastically again (Figure 23b).
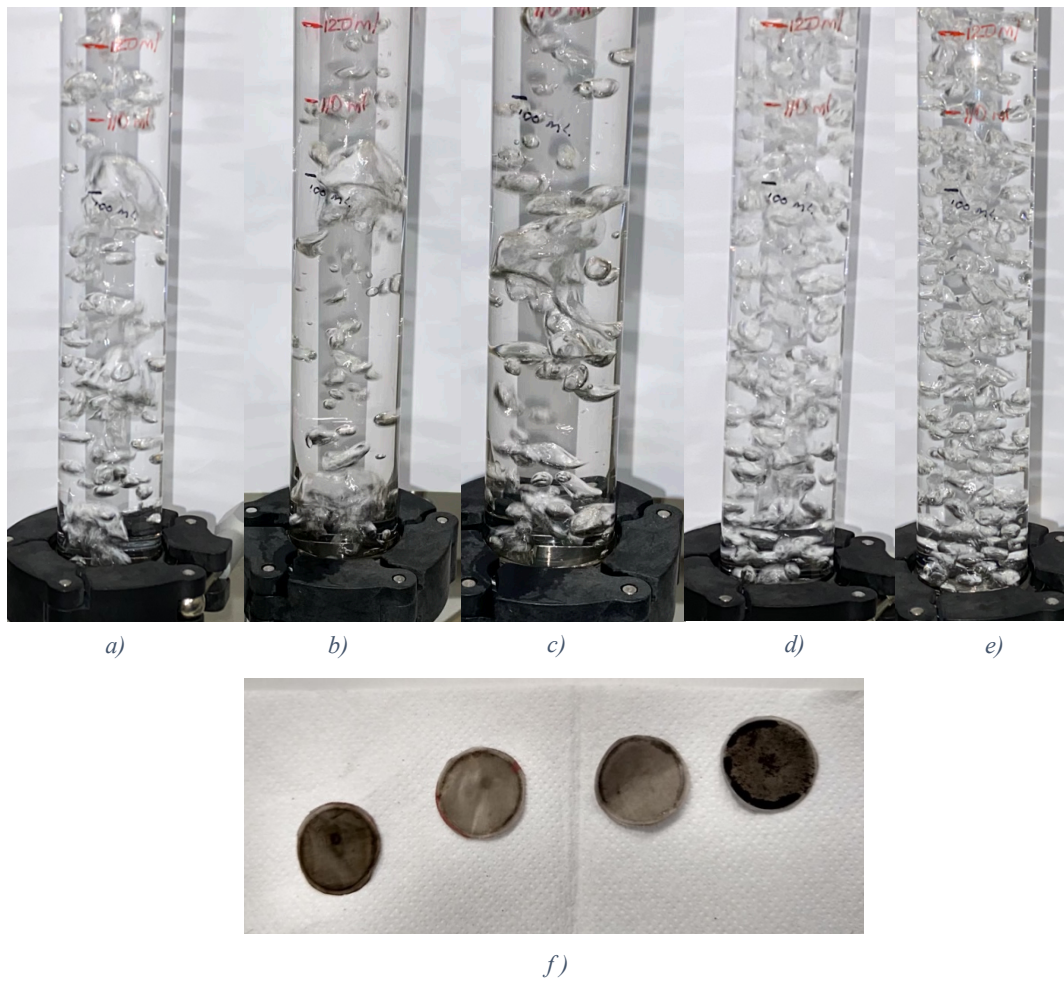
*Figure 22 Bubbling columns filled with 100 ml water under a flow rate of 1L/min for **a)** micro-bubbler used by Sharaf **b)** one metal mesh **c)** four metal meshes stacked **d)** stainless steel porous tablet **e)** bronze porous tablet **f)** metal meshes after an experiment showing a lot of particles are captured*
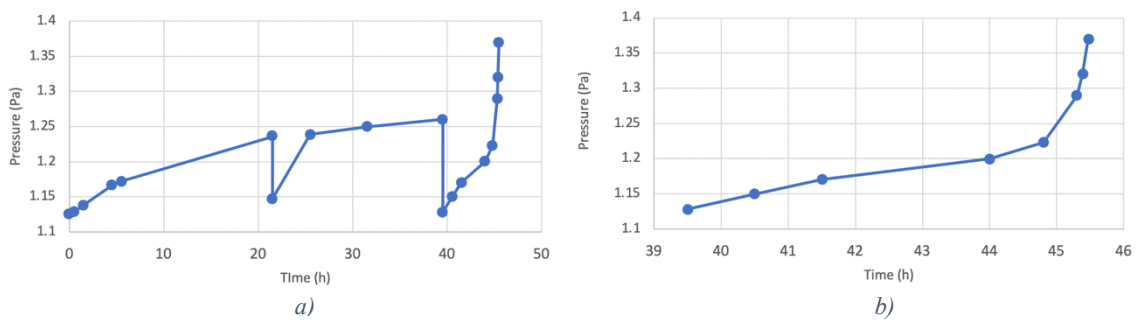

*Figure 23 The pressure increase for an experiment with Fe-Fe electrodes using 10mA 1.3kV and 1L/min. **a)** shows all three experiments **b)** shows the final one which had severe pressure increase at the end.*

The same experiments were done for the bronze tablet, but no pressure built-up occurred at all. Although the reported pore size for the sintered bronze micro-bubbler is smaller, its structure seems to be more permeable compared to that of the sintered stainless steel (Figure 24).

From E29 on, the bronze micro-bubbler was used in the setup. The use of the bronze micro-bubbler made it possible to collect particles over a duration up to 5 days, without building up pressure. This made it possible to reach a high concentration of particles and hence to do measurements on them. A large part of particles was also collected on the micro-bubbler. Using

an ultrasonic bath, these particles could be captured and, as it appeared from the NMR measurement (shown in the next chapter), these particles exhibited magnetic properties.

Figure 24 Porous tablets used in bubbling column: bronze (left) and stainless steel (right)

Electrodes

The downside of the long experiments is that the electrode eroded excessively. The Fe-electrode used for the experiment was hollow. The hollow electrode can be used as a gas inlet to increase the heat transfer between the electrode and the environment to suppress large particle (>100 nm) formation during spark ablation.[70] However, in combination with a solid electrode, the gas inlet is perpendicular to the electrodes and the hollow electrode acts as a solid electrode.

As a result of the long and high energy sparking, the electrodes eroded much faster than expected and therefore electrode symmetry decreased. Eventually, the 3mm Ho-electrode fitted inside the hollow Fe-electrode (Figure 25), which decreased the ablation efficiency drastically.
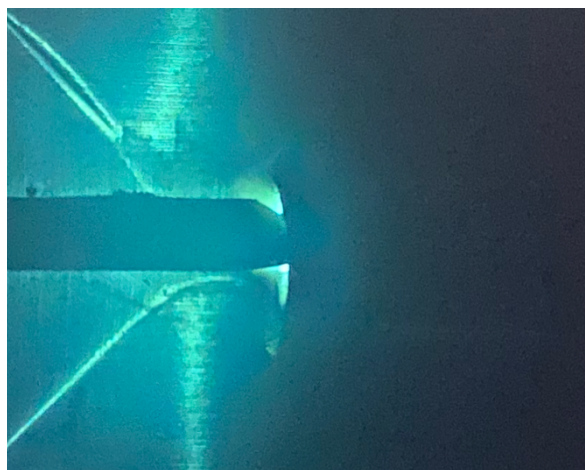

Figure 25 Ho-electrode (left) inserted inside the Fe-electrode (right). All sparking occurs inside the Fe electrode.

Furthermore, because the Fe-electrode is bigger than the Ho-electrode, it was placed at the high ablating anode side. The anode side is also the side which changes position during the sparking. Because only the Fe-electrode changed position while sparking, a decreasing length of the Ho-

electrode means that the spark ablation was positioned more towards the Ho-electrode and further away from the generator's center. This means the sparking is not happening in the middle of the carrier gas stream anymore. The electrodes were switched to place the spark ablation in the middle of the gas inlet and outlet. This placed the Ho-electrode on the high ablation side and the Fe-electrode on the low ablation side. The effect can be seen in Figure 26.

The switching of the electrodes made the insertion of the Ho-electrode inside the Fe-electrode even worse and at the end of E33, very low yield was the result. To improve the electrode configuration, solid Fe-electrodes were used. These were expected to have a higher yield due to more efficient sparking. As a result of a more symmetric shape of the electrode, the heating spot was expected to be better and more constant, resulting in more efficient sparking.[85] The new Fe electrode indeed showed a much higher yield and the concentration of Fe-Ho spark ablation increased from 0.17 mmol/L in 4 days to 0.91 mmol/L in 1-day production.

a)   *b)*

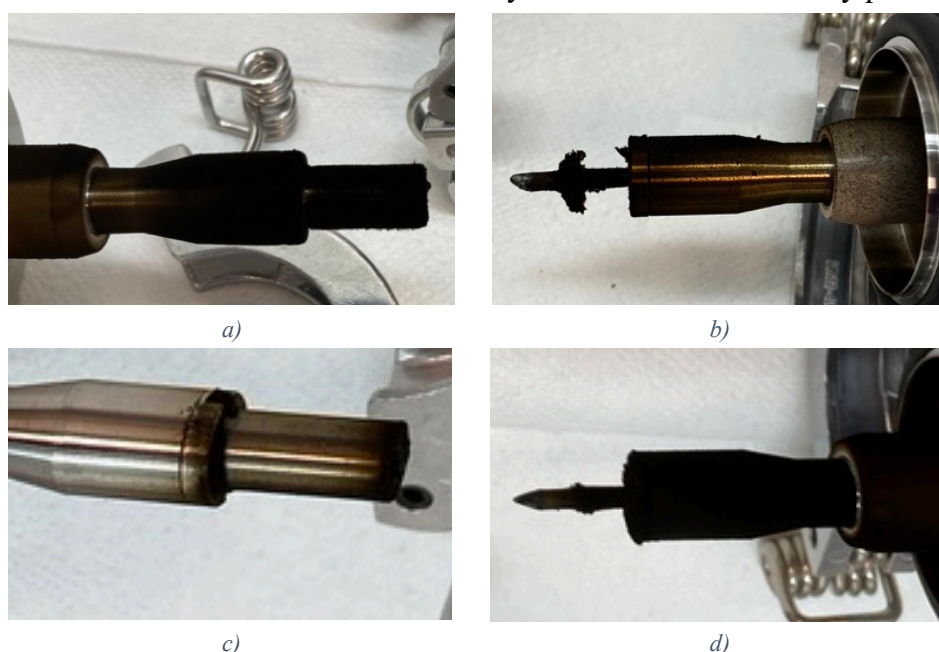*c)*   *d)*

Figure 26 Ablation of the electrodes is clearly seen by the different amounts of deposit on the electrode and electrode holder. a) shows the Fe-electrode as cathode, b) shows the Ho-electrode as anode, c) shows the Fe-electrode as anode and d) shows the Ho-electrode as cathode.

Summary VSP-G1 Setup

From the results given in this chapter, it could be concluded that the VSP-G1 was able to produce 4 nm Fe-Fe particles. To maximize the yield, the voltage, current and flow rate were set at 1.3 kV, 10 mA and 1 L/min. The bronze porous tablet was used as micro-bubbler and the bubbling column was filled with 60 mL to maximize the obtained concentration. Solid electrodes were used to improve the sparking efficiency.

4.2 Ho-doped Iron-oxide

In this section, the results for the characterization of Ho-Fe and Fe-Fe particles are shown. First, the morphology and size distribution were studied by TEM and DLS. The composition study was done by XRD, ICP, SEM-EDX and Mössbauer. Finally, the magnetic properties were assessed with the SQUID magnetometer and NMR. Since none of the samples were capable of generating heat, no heating measurements are presented in the results. The heating measurements are shown in Appendix B.7.

4.2.1 Morphology Studies

Morphology studies were done on the column and micro-bubbler samples of the experiments. The calculations on the TEM images are shown in Appendix B.1

Fe-Fe

From the TEM image in Figure 27a, it can be seen that NPs with an average size of 4 nm tend to aggregate. Figure 27b gives an overview of the TEM and shows many aggregates ranging from 50 nm to 800 nm. From the DLS chromatogram of E36, peaks at 30 nm and 100 nm were found (Figure 27c).

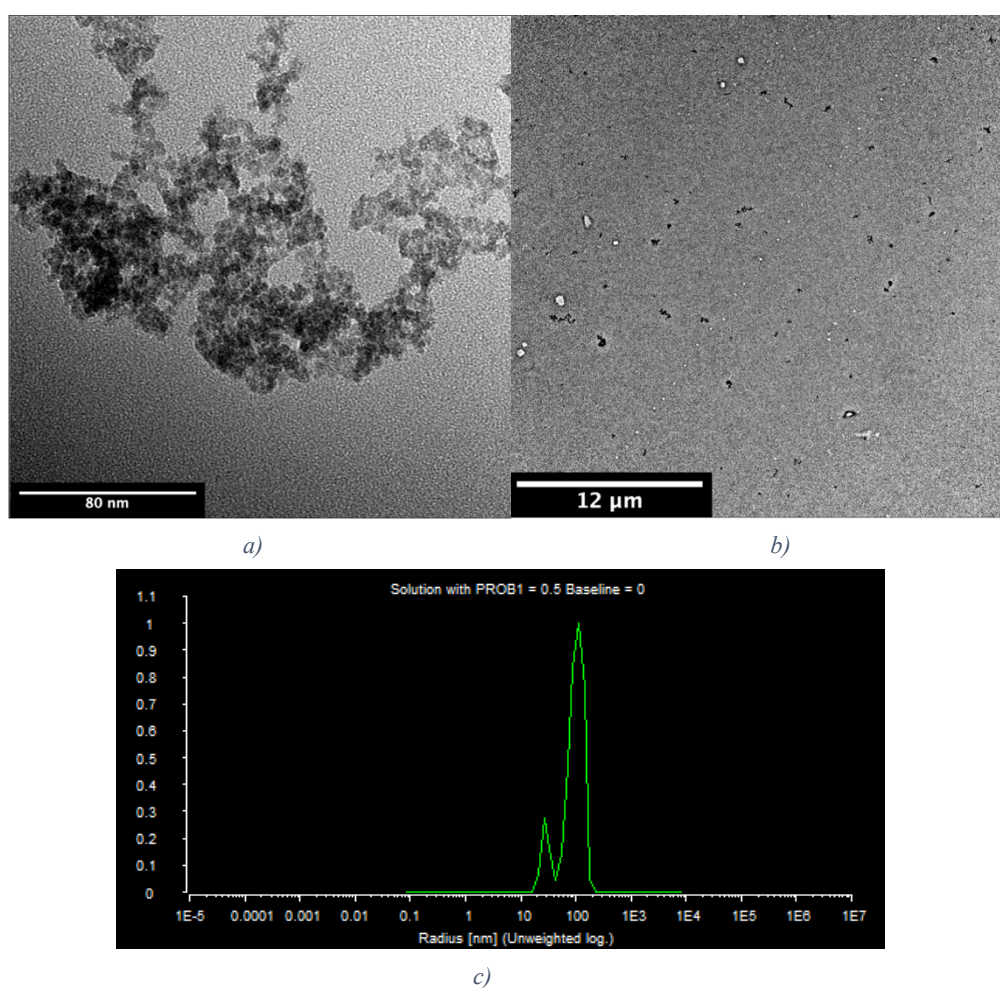*a)*   *b)*

c)

Figure 27 TEM images from the Fe particles of E36 a) agglomerate with primary particles sizes 4 nm; b) overview of the sample with agglomerates ranging from 50 nm to 800 nm in size; c) DLS chromatogram with peaks at 30 nm and 100 nm

Between the TEM and DLS measurement of E36, a big difference in the particle size was found. The difference can be explained by aggregation of the primary particles as observed also for the NPs in E13. The DLS analysis was carried out one day after the sample was taken. In both E13 and E36 a peak around 30 nm was found by DLS after one day of agglomeration, while the actual particle size by TEM was found to be around 4nm. This agglomeration is in agreement with literature.[64,70]

Ho-Fe

The DLS measurement of E37 reveals two mean peaks at 3 nm and 90nm, as shown in Figure 28c. The primary particle size found from the TEM image in Figure 28a is 4 nm and b) shows the agglomerates with a size of 600 nm and 350 nm
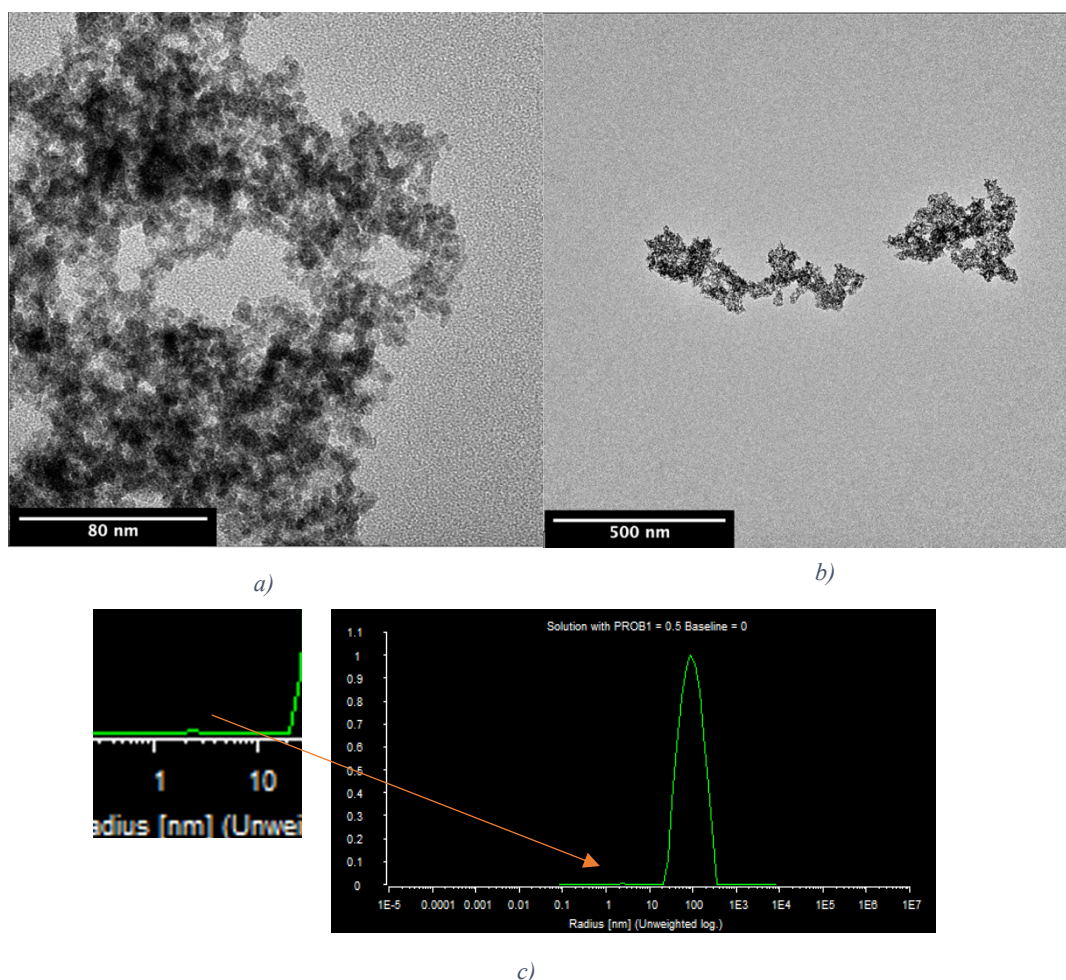

a)

b)

c)

Figure 28 TEM images from the Ho-Fe sample experiment 37. The average primary particle size in a) is estimated on 4 nm and the aggregate sizes in b) are 600 nm and 350 nm; c) DLS chromatogram with a peak at 3nm and 90nm

The 3 nm peak from the DLS chromatogram shows a low intensity because small particles scatter less efficient than large particle.[97,98] Furthermore, as a result of aggregation, the amount of small particles will be low.

Particle aggregation was confirmed by TEM and DLS, though it is not known where the aggregation happens. The aggregate formation on the TEM can happen after particle formation as described in the chapter about spark ablation, or it could happen during the TEM sample preparation, during which water is evaporated from the sample, leading to aggregation.[13,99]

Since the TEM measurements show bigger aggregates than the DLS measurement, it can be concluded that part of the aggregation happened before and some during the TEM preparation.

It can be concluded that for both the Fe-Fe and Ho-Fe electrode combinations, NPs of 4 nm were created. This is smaller than initially expected from data provided by VS-Particle, but in line with the data from Tabrizi *et al.*[13,99]

In Figure 29 it can be seen that large particles are also formed during spark ablation. As the spark discharges over the electrode arc, the electrode heats up and melts locally. According to Gray *et al.*, a force acts on the molten part of the electrode due to the ion bombardment.[70] This force is directed outwards from the electrode and if it exceeds the surface tension, a molten droplet is sputtered. Since these droplets are created by one electrode only, they will consist of pure Fe or Ho. These large particles can be found in both the column and micro-bubbler samples.

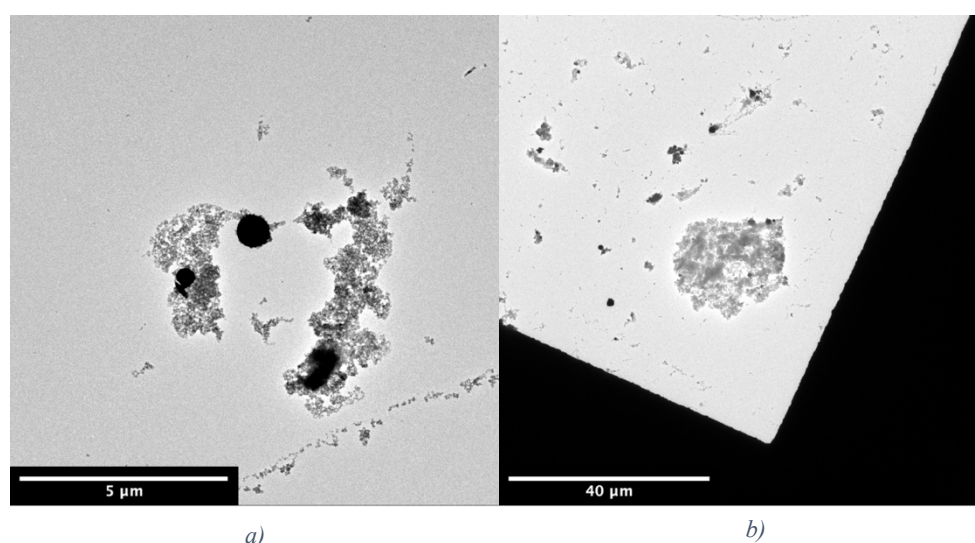a)   b)

Figure 29 TEM of the filter sample E33 from showing large particles a) two uniform spheres with size 380 nm and 740 nm b) overview illustrating the abundance of large particles in this sample with an average size of these particles of approximately 1.1 μm.

Inside the column sample of E34, crystal structures can be found (Figure 30). These are a result of preferred growth direction of the particles. Osial *et al.* reported that above a critical value of holmium dopant inside the ferrite lattice, particles will lose their spherical shape.[100] The same was found for doping magnetite with the lanthanides europium and samarium.[13]
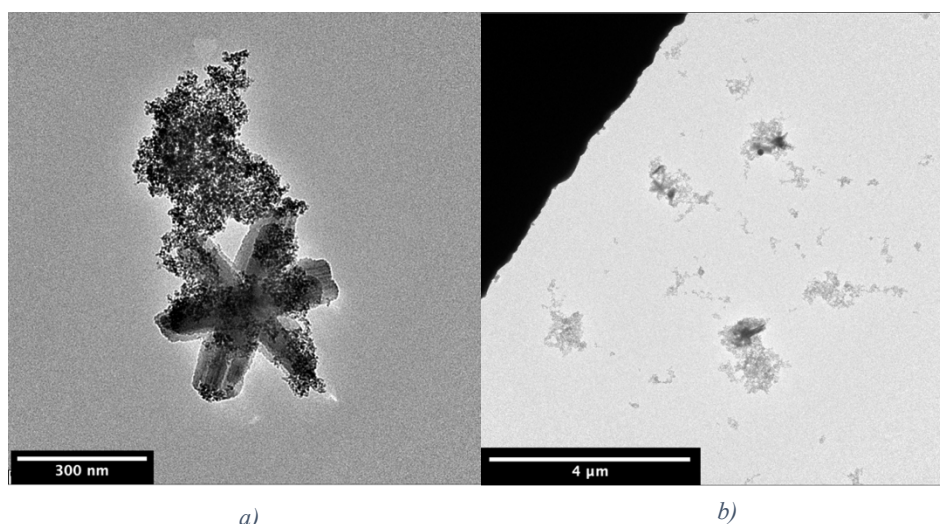
Figure 30 Star-like shapes created as a result of preferred growth direction; a) one enlarged symmetrical structure of approximately 400 nm b) an overview of the sample with several of these structures, all of a comparable size around 400 nm

Additionally, some unidentified large structures were found in the TEM that could not be explained. The images are presented in Appendix B.1 and are considered irrelevant for this research. However, this phenomenon should be investigated if it re-occurs.

4.2.2 Composition

To determine the composition of the created nanoparticles, several measurements were performed. As XRD and Mossbauer require a high amount of powder sample, the generator's residue powder was used. For ICP and SEM-EDX, the column and micro-bubbler samples were used.

XRD

For the XRD measurement, a very high background signal was found. The background was initially attributed to the fluorescence of iron in the sample.[57] Application of a monochromator was expected to block all fluorescence and reduce the background to almost zero. However, this attempt was not successful, as can be seen from Figure 31 and Figure 32. The cause of this background could not be explained.

Fe-Fe

For the Fe powder sample from the sparking chamber, the results are displayed in Figure 31 . All were compared with a pattern line from the database, however, only one match was found (Table 7). The score attributed to the matched compound indicates the quality of the match between the sample and the pattern in the database. Theoretically, a perfect match will be 100 but practice shows that matches will be in the order of 50-80.
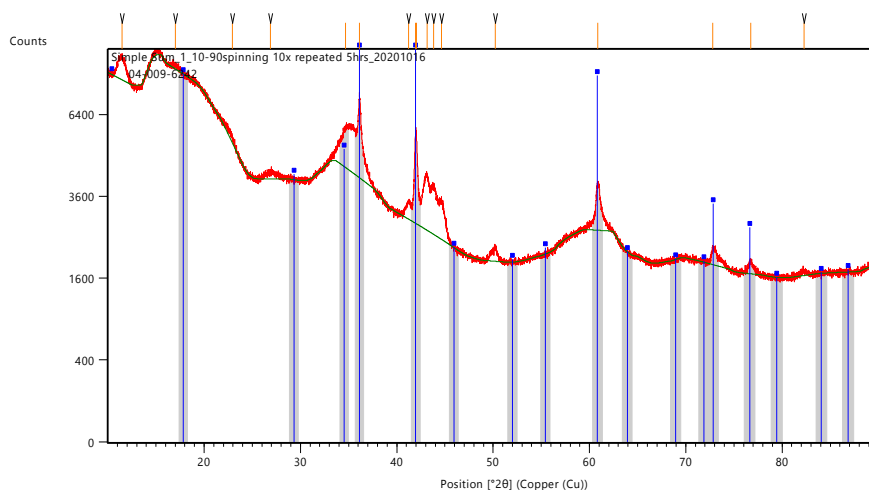
Figure 31 XRD Measurement with an Fe powder sample from the sparking chamber. The red line displays the signal measured and the blue lines show the iron oxide pattern with which it is matched.

Table 7 List of matched patterns from the database.

Sample	Score	Compound Name	Chem. Formula
Fe-Fe	63	Iron Oxide	$Fe_{3.776}O_4$
Ho-Fe	47	Holmium Oxide	Ho_2O_3

Ho-Fe

The XRD results of Ho-Fe powder from the sparking chamber are displayed in Figure 32 and Table 7. The intensity of two high peaks could not be matched with any of the database patterns.
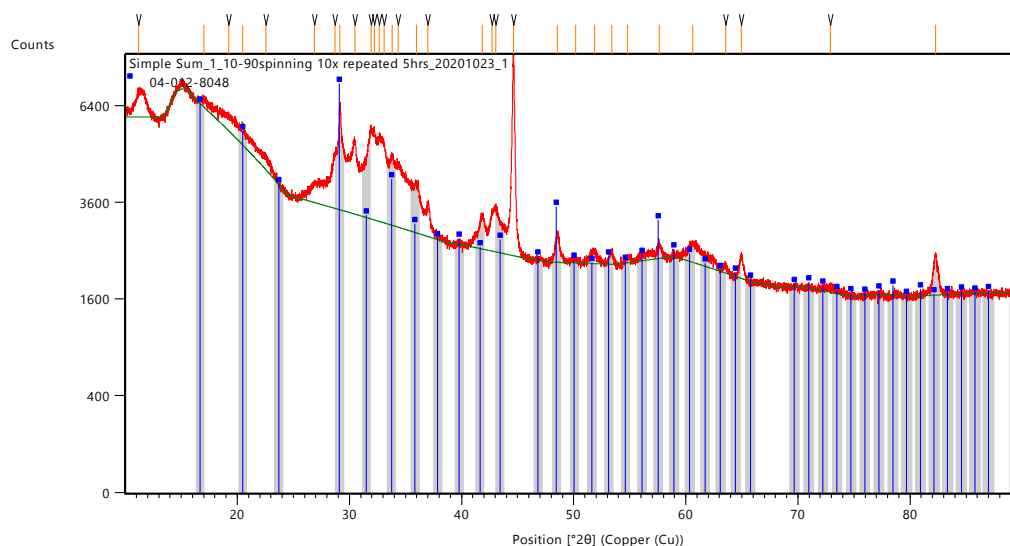

Figure 32 XRD measurement of Ho-Fe powder sample from the sparking chamber. The red line shows some narrow high peaks and the blue and green lines show the peaks with which the signal is matched. It should be noted that the highest peak is not matched correctly.

Remarkably, only one type of iron oxide was found in the Fe powder sample while the sample is expected to contain several oxidation states.[101] Also, no Fe contribution was found in the Ho-Fe sample. Both findings are attributed to the high background. Several reasons for the high background have been considered. However, no satisfactory explanation has been found. The background cannot be attributed to the small particles size, because no peak broadening was found.[102] The background cannot be attributed to fluorescence because a monochromator was used.[103] Neither can it be attributed to the presence of amorphous material because none was found with Mössbauer. Since the XRD measurement is not representative for the samples, the measurements are left out of consideration in further discussions.

ICP

ICP was performed on the samples taken from E33, E34, E36 and E37. Figure 33 shows the samples of these experiments. Because for E33 and E34 most particles where captured inside the micro-bubbler, two samples were used. One of the micro-bubbler and one column sample. For E33, E36 and E37 the Ho electrode was placed on the anode side of the generator. For E34, the Ho- and Fe-electrodes where switched to improve the electrode placement with respect to the carrier gas flow. The result of the ICP can be found in Table 8.

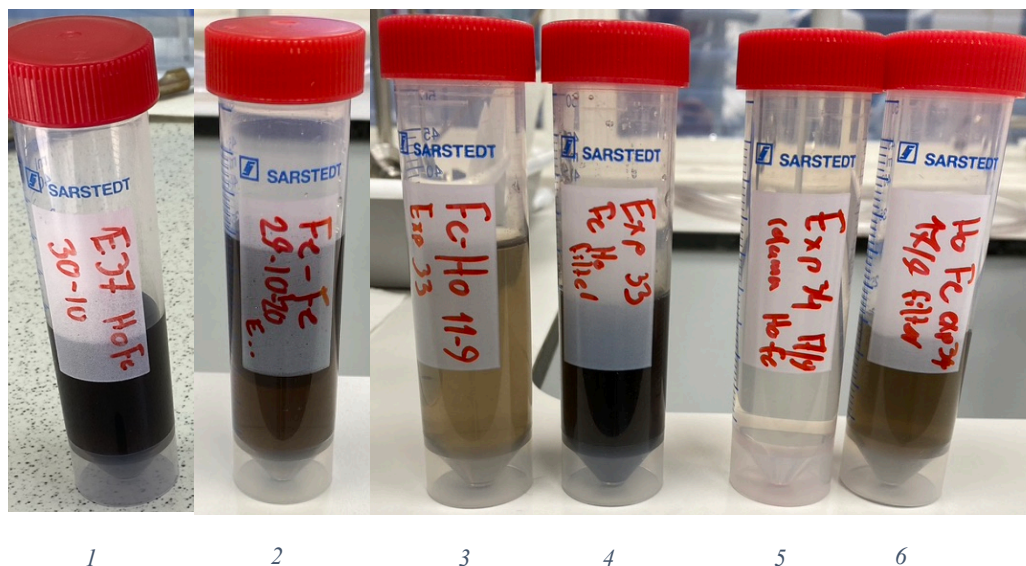|					
1	2	3	4	5	6

Figure 33 From left to right: E37, E36, E33 column, E33 micro-bubbler, E34 column, E34 micro-bubbler Clear concentration differences can be observed.

Table 8 ICP results for 5 mL sample

#	Experiment	Fe (mg/L)	Ho (mg/L)	Ratio mol Ho/Fe	Concentration (mmol/L)
1	Ho-Fe 37 column	51	21	0.085	0.91
2	Fe-Fe 36 column	23	0.1	0.00090	0.41
3	Ho-Fe 33 column	9.3	5.7	0.13	0.17
4	Ho-Fe 33 micro-bubbler	63	37	0.12	1.13
5	Ho-Fe 34 column	1.9	2.6	0.28	0.034
6	Ho-Fe 34 micro-bubbler	29	24	0.17	0.52

Since the composition of the sample was not known, the concentration was calculated with the assumption that the whole sample has the mol ratio measured by ICP (Ho_xFeO, where x is the Ho/Fe ratio). Thus, the contribution of pure Ho or Fe and all other oxides were neglected. The calculation can be found in the Appendix B.4.

The ICP measurements showed significant differences in the ratios between Fe and Ho. These can be explained by the change in the electrode placement. For E34 the ratio Ho/Fe is very

high because the Ho electrode was placed on the anode side. This is in agreement with literature.[104]

The low concentration for E34 can be explained by inefficient sparking. During experiment E33 it was noted that the Ho-electrode was placed inside the hollow Fe electrode. For E34 this was even worse and therefore the production was very low. For E33 and E34, large particles where found inside the micro-bubbler. The size of the particles was above 500 nm, which means that according to Figure 16, the particles get captured primarily by collisions and almost nothing by diffusion. Furthermore, the pore size of the micro-bubbler is 0.4-20 μm, so some of the particles will be filtered out by the micro-bubbler. This results in more particles in the micro-bubbler and explains the big difference in concentration between the micro-bubbler samples the column samples.

E36 and E37 were done with new electrodes and should be considered the most representative result for future experiments. A significant difference between the concentration of the Ho-Fe and Fe-Fe sample could be observed. Intuitively, when having two electrodes of the same material instead of one, one would expect double the amount of ablated material. However, Table 8 shows that for two iron electrodes, only half the amount of ablated Fe was found. This can be explained by the symmetry of the sparks occurring between two electrodes. The two Fe-electrodes have a big surface on which the spark can occur. During the sparking of two Fe-electrodes, the spark is observed, and it is concluded that the position of the spark constantly changes over the electrode surface. Since the Ho-electrode is much smaller than the Fe-electrode, sparking between those two electrodes always happens at the same place, creating higher temperatures at the sparking spot and thus more ablated material.

SEM-EDX

To learn more about the composition of the particles, four SEM-EDX measurements were performed on sample 37. The results are displayed in Figure 34.

In Table 9 the mass percentages of all EDX measurements can be found. The SEM image in Figure 34A shows again the presence of large particles in the sample. From the EDX measurement in Figure 34B and C, it is clear that these large particles consist of a high concentration of holmium-oxide. This is what is expected, because the large particles are a result of liquid droplets from one electrode only. Therefore, all large particles are expected to consist of only one material. Another remarkable fact is that a pure palladium particle is found inside this sample. The presence of Pd is explained as contamination of the generator by experiments carried out by another student.
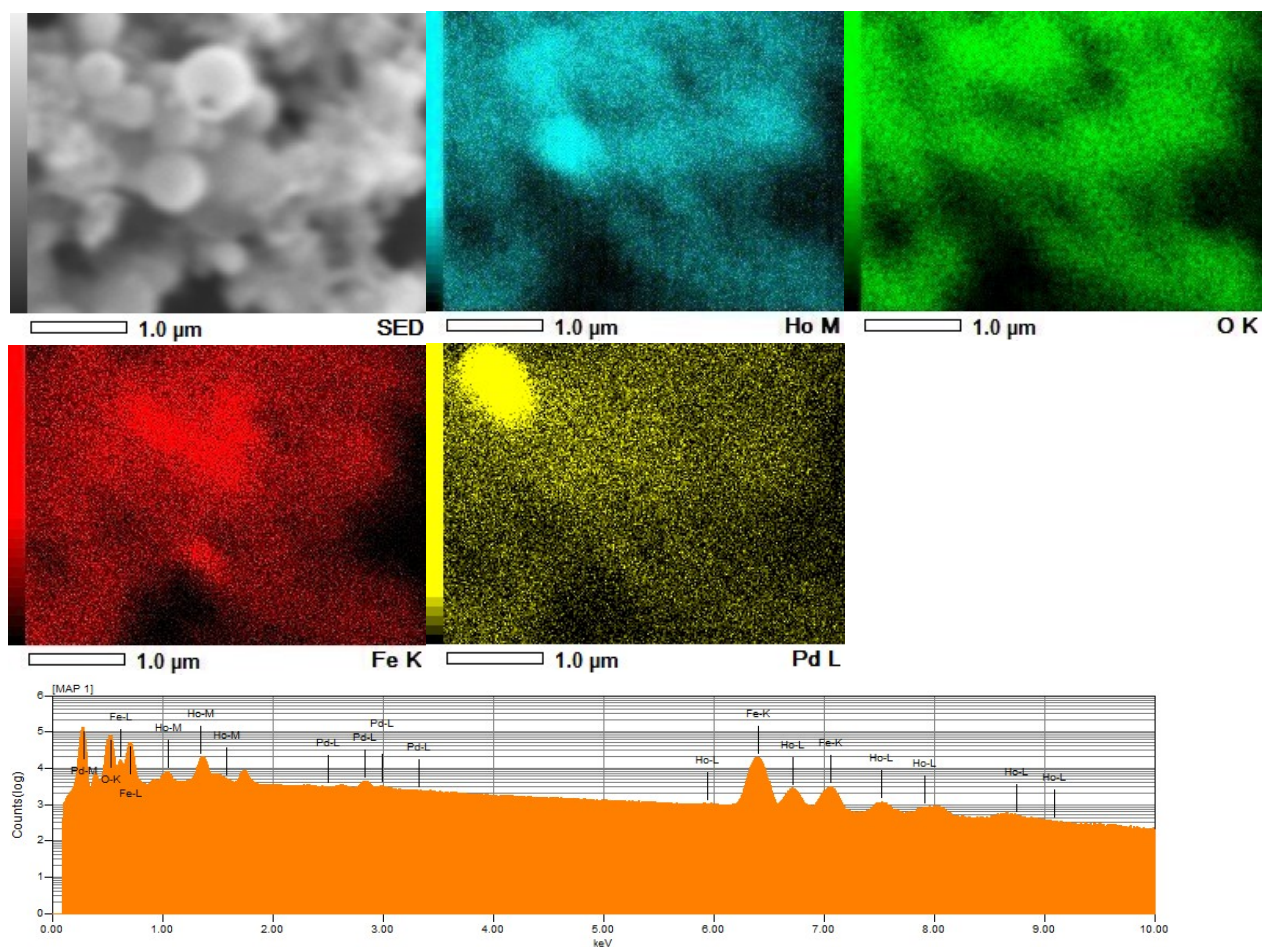
Figure 34 Characterization of Ho-Fe sample obtained after 1.5h spark-ablation A) SEM-EDX image, B-E) EDX images of different elements present, F) spectroscopy chart of the elements.

Table 9 Quantities of Ho and Fe obtained by EDX.

	Fe (wt%)	Ho (wt%)	O (wt%)	Ho/Fe (molar ratio)
Column 1	13.96	9.28	16.84	0.1369
powder	58.16	28.41	13.42	0.1006
freeze-dried	47.51	35.59	16.9	0.1542
Column 2	47.14	35	16.3	0.1529
Column 3	48.01	34.04	16.29	0.1460

The molar ratios found by SEM-EDX are very dependent on the sample used for therefore are not representable for the whole sample. However, they show that the bulk of NPs consist of Fe, Ho and O, as expected for the production process used.[69]

Mössbauer

Mössbauer measurements were performed on the iron powder from the generator. Since the Mössbauer needs 50 mg and only several milligrams were found in the generator per experiment, all powder samples were combined and used for the measurements. By doing this, it was assumed all samples consisted of the same iron species.

In Figure 35 Mössbauer measurement is displayed and Table 10 summarizes the calculated results. From the measurement it is clear that the powder sample consists of only 5% high magnetic moment magnetite and 34% superparamagnetic material; 51% of the sample is paramagnetic Fe^{2+} and 10% is bulk material.
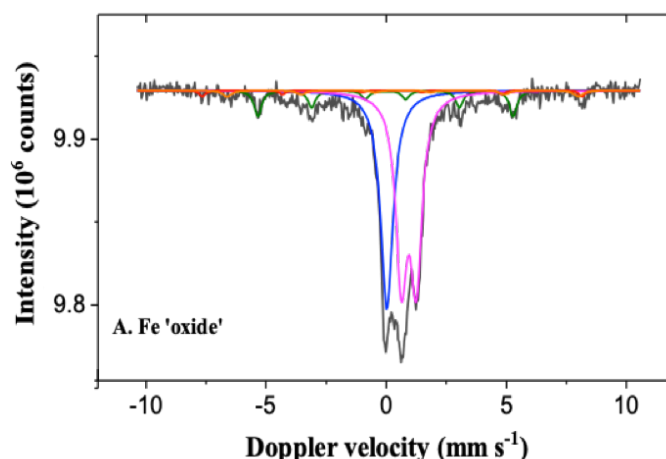

Figure 35 Mössbauer measurement at 300 K of the iron powder sample from the generator.

Table 10 The results of the Mössbauer measurement calculated by the Mosswinn 4.0 program.[70]

	IS (mm/s)	QS (mm/s)	Hyperfine field (T)	Γ (mm/s)	Phase	Spectral contribution (%)
Fe "oxide"	0.02	-	-	0.63	Fe^0 (SPM)[a]	34
	0.00	-	33.0	0.37	Fe^0	10
	0.94	0.62	-	0.57	Fe^{2+}	51
	0.25	0.01	49.1	0.30	Fe^{3+} (Fe_3O_4, A)	2
	0.69	0.00	45.5	0.45	$Fe^{2.5+}$ (Fe_3O_4, B)	3

TEM, EDX and Mössbauer show the presence of bulk material inside the sample. This leads to a discrepancy in the concentration calculation and magnetic properties of the nanoparticles. Furthermore, a low number of superparamagnetic NPs measured by Mössbauer raises the question how much of the sample consists of the desired particles and how much is a by-product. It must be emphasized that the materials used for the measurements in this section have been generator's rest-products. There is no control whatsoever on the production of these particles and no research has ever been done on the content of the material found inside the generator.

From the composition measurements, it must be concluded that the NPs content is still unknown. For the rest of the results, it must be realized that the sample content is too variable and no hard conclusions can be drawn.

4.2.3 Magnetization Properties

SQUID curve

To compare the magnetic performance of Ho-doped particles with that of a pure iron oxide particle, magnetization measurements were performed on the samples of E36 and E37. The concentration of E36 and E37 was too low and only diamagnetic water was measured. The result of the measurement of E36 can be seen in Appendix B.6.

Because no higher concentration was available, 1 mg of the residue powder from the generator was measured. The results suggests that this material exhibits superparamagnetic behavior (Figure 36), which is expected since these particles have a primary size of 5 nm and the measurement temperature was 300K, so above the blocking temperature.[93]
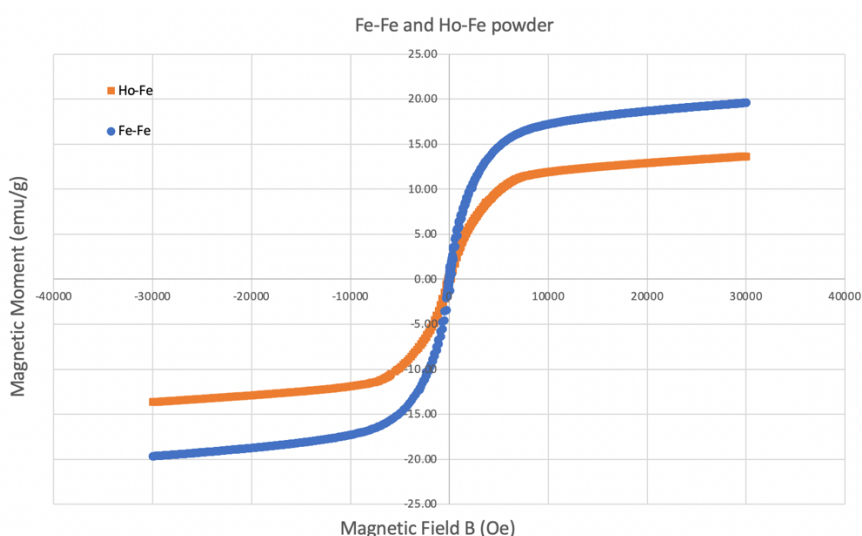

Figure 36 Hysteresis loop of Fe-Fe and Ho-Fe NP residue powder from the generator

The saturation magnetizations are 13.6 emu/g for Ho-Fe and 19.6 emu/g for Fe-Fe. Guardia *et al.* reported a saturation magnetization of 75 emu/g for magnetite NPs of 4.2 nm.[105] Osial *et al.* reported a saturation magnetization of 76 emu/g for pure magnetite of 10-15 nm and 7 emu/g for 5% Ho-doped magnetite of 30-40 nm.[51] From the Mössbauer measurements, it can be concluded that only a small part of the sample is superparamagnetic. Therefore, only a small amount of the sample is contributing to the magnetic saturation.

Furthermore, the particles are in powder form and thus have a high level of aggregation. It is assumed that the reduction of magnetization is a result of single magnetic domains canceling due to the cluster aggregation.[13] Since the particles were dried and aggregated, they cannot move freely under exposure to an external magnetic field, decreasing their saturation magnetization.

The difference in saturation magnetization between Fe-Fe and Ho-Fe can be explained by the distortion of the lattice structure by the introduction of Ho. Research shows that the saturation magnetization often decreases by adding a dopant and only for certain concentrations of a specific element, an increase in saturation magnetization occurs.[25] Osial *et al.* looked at the introduction of Ho in magnetite NPs and concluded that the saturation magnetization decreases rapidly for increasing Ho concentration.[12,13,42,52,59] Nonetheless, the saturation magnetization has also been reported to increase for incorporation of Ho and other lanthanides, depending on the placement of the dopant in the lattice structure.[55,59]

NMR

To compare the effect of Ho doping on the relaxation properties, a pure iron oxide sample was compared to several Ho-Fe samples. From the relaxation times measured, combined with the concentrations obtained from ICP, the relaxivities were calculated. All results are displayed in Table 11.

Table 11 Results of NMR measurement and ICP measurement combined to a relaxivity for r_1 and r_2

#	Experiment	Molar ratio Ho/Fe	Concentration (mM)	T_1 (s)	T_2 (s)	r_1 (mM/s)	r_2 (mM/s)	ratio r_2/r_1
1	Ho-Fe 37 column	0.085	0.91	0.39	0.17	2.84	6.29	2.22
2	Fe-Fe 36 column	0.00090	0.41	2.97	0.33	0.82	7.42	9.09
3	Ho-Fe column 33	0.13	0.17	3.07	0.16	1.96	37.45	19.13
4	Ho-Fe micro-bubbler 33	0.12	1.13	2.68	0.042	0.33	20.91	63.24
5	Ho-Fe column 34	0.28	0.034	~~0.0080~~[*]	0.68	~~3668.46~~[*]	43.36	~~0.012~~[*]
6	Ho-Fe micro-bubbler 34	0.17	0.52	3.02	0.094	0.64	20.45	32.09

[*] T_1 of E34 is a measurement error as can be seen in Appendix B.2 and is therefore neglected.

In contrast to iron-oxide, Ho has no saturation magnetization for high magnetic fields.[14,106] For high magnetic fields the transversal relaxivity increases with the residence time.[19] For small particles the residence time is negligible and the relaxivity is only governed by the outer sphere model. For larger particles the inner sphere relaxation becomes more significant and the residence time increases. Since the NMR spectrometer used a high magnetic field, the contribution of large Ho particles to the transversal relaxivity is expected to be higher than that of the small iron-oxide and Ho particles. Therefore, samples with a high concentration of large Ho particles are expected to have higher transversal relaxivities. For E33 and E34 the inefficient sparking resulted in numerous large particles. For E37 the electrode configuration was improved and therefore, no large particles were produced. From Table 11 it is seen that E33 and E34 have the highest and E36 has the lowest transverse relaxation, which substantiates this hypothesis

As described in the ICP results and discussion, the large particles are more likely to be captured in the micro-bubbler. Therefore, the micro-bubbler samples have a high concentration of large particles, but over time other particles accumulate as well. Therefore, the concentration in the micro-bubbler sample increases over time, without increasing the relaxation of the sample. As a result, the micro-bubbler samples have lower relaxivities than the column samples.

From the relaxivity ratios seen in Table 11, the Ho-Fe NPs created mostly act as T_2 relaxation agents. Comparable elements like Dy- and Mn-iron oxides act as T_2 CA, so it was expected that Ho also acts as a T_2 CA.[13] Because the NPs are superparamagnetic, the purely outer sphere behavior of the MAR regime would be expected. However, because of the aggregation, the particles might not be in the MAR regime, but in the SDR regime, where diffusion is neglected and the relaxation is linear with the magnetic moment.[19,30] However, this cannot be tested. On the other hand, iron oxide nanoparticles of the order below 4nm are reported to be T_1 contrast agents because of their high surface-to-volume ratio and low magnetic moment (eq. (8)).[107] Since all produced NPs were approximately 4nm, this could explain T_1 relaxation behavior seen in E37.

Although the relaxivities of E33 and E34 are much alike, it should be mentioned that the time between the experiment and the NMR measurement differed a lot. E33 was measured a week after the experiment, whereas E34 was measured directly after the experiment. E36 and E37 were measured 5 and 4 days after the experiment, respectively.

5 Conclusions and Recommendations

This work has examined the effect of Ho-doping on the performance of SPIONs. This was done using the relatively new synthetic method, spark ablation. An overall conclusion about the synthetic method and the Ho doped SPIONs are provided below. Additionally, recommendations for future research are given building on shortcomings of this research.

The first part of this research focused on the relatively new spark ablation synthesis method. Using the spark ablation generator from VS-Particle appeared to be more challenging than expected. The maximal size of primary particle that could be achieved for Fe NPs was 4nm, while larger sizes were desired in this project. Furthermore, the initial set-up was not able to provide yields high enough for sufficient analysis and intended applications. Therefore, the micro-bubbler was replaced by a bronze sintered filter with pore size 0.4-20 μm. Furthermore, the hollow Fe-electrodes provided by the company did not result in good outcome and had to be changed halfway to improve the sparking efficiency between the Ho- and Fe-electrodes. Finally, the bubbling column volume was lowered to 60 mL. This modification enhanced the spark ablation, resulting in improved yields. The concentration of Fe-Ho nanoparticles produced by spark ablation increased from 0.06 mmol/(L·day) to 0.91 mmol/(L·day).

Looking at the results of the second part of this research, it can be concluded that 4 nm Ho-doped iron oxides and 4 nm iron oxides can be produced using spark ablation. All particles showed superparamagnetic behavior and influenced the relaxivity times of water protons. It remains unclear to what extent the relaxivity was changed compared to pure SPIONs, because no good qualification of the produced particles could be obtained.

The goal of this research was to investigate if Ho-doped SPIONs can be applied for heating by an alternating magnetic field. Although big steps were made in the understanding of the particle formation inside the spark generator and particle capture inside the bubbling column, the data on the produced particles is not conclusive. From theory it is clear that the heating properties depend simultaneously on many parameters. Therefore, in order to be able to measure the effect of Ho-doping, all other parameters must be kept constant. Furthermore, the way Ho is integrated inside the SPIONs is critical and more advanced characterization should be done to evaluate this integration.

5.1 Recommendations

In order to overcome the challenges of obtaining reproducible production from spark ablation, some recommendations have been identified. First, the input factors of the generator should be examined using VS-Particle filter capture accessory. The current setup using the bubbling column has too many parameters influencing the production process and capturing of the nanoparticles. Low concentrations in the bubbling column did not allow for detailed investigations on the effect of the settings on the NPs production process. Using the filter of VS-Particle a better insight could be obtained on the particles produced. Second, to measure the magnetic properties of the produced NPs, the concentration of the samples should be increased. Promising concentrations were found for the final two experiments after one day. Longer experiments could provide higher concentrations. Also, the yield can be improved by changing the properties of the volume of bubbling column, for example by changing the acidity or viscosity of the solution.

In short, spark ablation is a very promising technique, but it may be a step too far to use it for research on medical NPs. Spark ablation becomes interesting if used for mass production but might not be flexible enough for research applications. If earlier mentioned suggestions do not work out, the use of spark ablation synthesis should be abandoned. Therefore, the final suggestion will be to investigate the suitability of Ho for application in hyperthermia using the hybrid particles prepared by wet-chemistry. Co-precipitation technique has proven to be a fulfilling way to incorporate Ho in magnetite and this can give a quick insight in the magnetic properties of Ho.[13,55] This could be conclusive on whether it is worthwhile to proceed with Ho for this purpose.

Nota Bene: For the Mössbauer measurement of another student, it was seen that Pd oxidizes to a lower extent than Fe.[108,109] If this is also true for Ho, this would be an interesting property for the heating application of Ho. Since no Mössbauer was done on the Ho-Fe samples, nothing could be said about the oxidation of Ho. Future research should therefore investigate the oxidation state of Ho.

Bibliography

1. Bray F, Ferlay J, Soerjomataram I, Siegel RL, Torre LA, Jemal A. Global cancer statistics 2018: GLOBOCAN estimates of incidence and mortality worldwide for 36 cancers in 185 countries. *CA Cancer J Clin*. 2018;68(6):394-424. doi:10.3322/caac.21492

2. DeSantis CE, Ma J, Gaudet MM, et al. Breast cancer statistics, 2019. *CA Cancer J Clin*. 2019;69(6):438-451. doi:10.3322/caac.21583

3. Pignol JP, Caudrelier JM, Crook J, McCann C, Truong P, Verkooijen HA. Report on the Clinical Outcomes of Permanent Breast Seed Implant for Early-Stage Breast Cancers. *Int J Radiat Oncol Biol Phys*. 2015;93(3):614-621. doi:10.1016/j.ijrobp.2015.07.2266

4. Crook J, Hilts M, Batchelar D, et al. Permanent breast seed implant for partial breast radiotherapy after partial mastectomy for favorable breast cancer: Technique, results, and applications to various seroma presentations. *Brachytherapy*. 2019;18(4):510-520. doi:10.1016/j.brachy.2019.04.003

5. Skowronek J. Current status of brachytherapy in cancer treatment – short overview. *J Contemp Brachytherapy*. 2017;9(6):581-589. doi:10.5114/jcb.2017.72607

6. Djanashvili K, Denkova A, Pignol JP, van Rhoon G. Nanoparticles for image guided Thermo-Brachytherapy. Published online 2017.

7. Vinardell M, Mitjans M. Metal/Metal Oxide Nanoparticles for Cancer Therapy. In: ; 2018:341-364. doi:10.1007/978-3-319-89878-0_10

8. Giustini AJ, Petryk AA, Cassim SM, Tate JA, Baker I, Hoopes PJ. Nano Life. *Nano Life*. 2010;1:17-32. doi:10.1142/S1793984410000067.MAGNETIC

9. Zhang Y, Zhang W, Geng C, et al. Thermal ablation versus conventional regional hyperthermia has greater anti-tumor activity against melanoma in mice by upregulating CD4+ cells and enhancing IL-2 secretion. *Prog Nat Sci*. 2009;19(12):1699-1704. doi:10.1016/j.pnsc.2009.05.007

10. Dennis CL, Ivkov R. Physics of heat generation using magnetic nanoparticles for hyperthermia. *Int J Hyperth*. 2013;29(8):715-729. doi:10.3109/02656736.2013.836758

11. Dadfar SM, Camozzi D, Darguzyte M, et al. Size-isolation of superparamagnetic iron oxide nanoparticles improves MRI, MPI and hyperthermia performance. *J Nanobiotechnology*. 2020;18(1):1-13. doi:10.1186/s12951-020-0580-1

12. Kershi RM, Ali FM, Sayed MA. Influence of rare earth ion substitutions on the structural, optical, transport, dielectric, and magnetic properties of superparamagnetic iron oxide nanoparticles. *J Adv Ceram*. 2018;7(3):218-228. doi:10.1007/s40145-018-0273-5

13. Osial M, Rybicka P, Pekala M, Cichowicz G. Easy Synthesis and Characterization of Holmium-Doped SPIONs. *Nanomaterials*. Published online 2018.

14. Mayer F, Peters JA, Djanashvili K. Microwave-assisted seeded growth of lanthanide-based nanoparticles for imaging and therapy. *Chem - A Eur J*. 2012;18(26):8004-8007. doi:10.1002/chem.201200472

15. De Silva CR, Smith S, Shim I, et al. Lanthanide(III)-doped magnetite nanoparticles. *J Am Chem Soc*. 2009;131(18):6336-6337. doi:10.1021/ja9014277

16. Xu W, Bony BA, Kim CR, et al. Mixed lanthanide oxide nanoparticles as dual imaging agent in biomedicine. *Sci Rep*. 2013;3:1-10. doi:10.1038/srep03210

17. Bult W, Varkevisser R, Soulimani F, et al. Holmium nanoparticles: Preparation and in vitro characterization of a new device for radioablation of solid malignancies. *Pharm Res*. 2010;27(10):2205-2212. doi:10.1007/s11095-010-0226-3

18. Smits MLJ, Nijsen JFW, Van Den Bosch MAAJ, et al. Holmium-166 radioembolization for the treatment of patients with liver metastases: Design of the phase i HEPAR trial. *J Exp Clin Cancer Res*. 2010;29(1):5-12. doi:10.1186/1756-9966-29-70

19. Norek M, Peters JA. MRI contrast agents based on dysprosium or holmium. *Prog Nucl Magn Reson Spectrosc*. 2011;59(1):64-82. doi:10.1016/j.pnmrs.2010.08.002

20. Scepka T. Noninvasive control of magnetic state in ferromagnetic nanodots by Hall probe magnetometry. 2016;(April).

21. Gamarra L, Silva AC, Oliveira TR, et al. Application of hyperthermia induced by superparamagnetic iron oxide nanoparticles in glioma treatment. *Int J Nanomedicine*. Published online 2011:591. doi:10.2147/ijn.s14737

22. Cotin G, Perton F, Blanco-Andujar C, Pichon B, Mertz D, Bégin-Colin S. Design of Anisotropic Iron-Oxide-Based Nanoparticles for Magnetic Hyperthermia. *Nanomater Magn Opt Hyperth Appl*. Published online 2018:41-60. doi:10.1016/B978-0-12-813928-8.00002-8

23. Chan KW, Chou CK. Use of thermocouples in the intense fields of ferromagnetic implant hyperthermia. *Int J Hyperth*. 1993;9(6):831-848. doi:10.3109/02656739309034986

24. Lucchini MA, Canepa F. Brownian relaxation of magnetic nanoparticles in fluid: The effect of the solvent. *J Nanoparticle Res*. 2012;14(4). doi:10.1007/s11051-012-0809-5

25. Wang C, Hsu CH, Li Z, et al. Effective heating of magnetic nanoparticle aggregates for in vivo nano-theranostic hyperthermia. *Int J Nanomedicine*. 2017;12:6273-6287. doi:10.2147/IJN.S141072

26. Cole AJ, Yang VC, David AE. Cancer theranostics: The rise of targeted magnetic nanoparticles. *Trends Biotechnol*. 2011;29(7):323-332.

doi:10.1016/j.tibtech.2011.03.001

27. Torres TE, Lima E, Calatayud MP, et al. The relevance of Brownian relaxation as power absorption mechanism in Magnetic Hyperthermia. *Sci Rep*. 2019;9(1):1-11. doi:10.1038/s41598-019-40341-y

28. Estelrich J, Sánchez-Martín MJ, Busquets MA. Nanoparticles in magnetic resonance imaging: From simple to dual contrast agents. *Int J Nanomedicine*. 2015;10:1727-1741. doi:10.2147/IJN.S76501

29. Shokrollahi H. Contrast agents for MRI. *Mater Sci Eng C*. 2013;33(8):4485-4497. doi:10.1016/j.msec.2013.07.012

30. Peters JA. Relaxivity of manganese ferrite nanoparticles. *Prog Nucl Magn Reson Spectrosc*. 2020;120-121:72-94. doi:10.1016/j.pnmrs.2020.07.002

31. Zhang Y, Wei W, Das GK, Yang Tan TT. Engineering lanthanide-based materials for nanomedicine. *J Photochem Photobiol C Photochem Rev*. 2014;20(1):71-96. doi:10.1016/j.jphotochemrev.2014.06.001

32. Bammer R. *MR and CT Perfusion and Pharmacokinetec Imaging: Clinical Applications and Theoretical Principles*. 1st ed. Wolters Kluwer; 2016.

33. Jung BA, Weigel M. Spin echo magnetic resonance imaging. *J Magn Reson Imaging*. 2013;37(4):805-817. doi:10.1002/jmri.24068

34. Kozlowska D, Foran P, MacMahon P, Shelly MJ, Eustace S, O'Kennedy R. Molecular and magnetic resonance imaging: The value of immunoliposomes. *Adv Drug Deliv Rev*. 2009;61(15):1402-1411. doi:10.1016/j.addr.2009.09.003

35. Burtea C, Laurent S, Elst L vander, Muller R. Contrast agents: Magnetic Resonance. *Handb Exp Pharmacol*. 2008;(may 2008):136-158. doi:10.1007/978-3-540-72718-7

36. Narmani A, Farhood B, Haghi-Aminjan H, et al. Gadolinium nanoparticles as diagnostic and therapeutic agents: Their delivery systems in magnetic resonance imaging and neutron capture therapy. *J Drug Deliv Sci Technol*. 2018;44(February):457-466. doi:10.1016/j.jddst.2018.01.011

37. Suntharalingam N. Chapter 13 BRACHYTHERAPY : *At Energy.*:451-484.

38. Skowronek J, Zwierzchowski G, Piotrowski T. Pulsed dose rate brachytherapy - Description of a method and a review of clinical applications. *Reports Pract Oncol Radiother*. 2001;6(4):197-202. doi:10.1016/S1507-1367(01)70973-X

39. Skowronek J, Malicki J, Piotrowski T. Values of biologically equivalent doses in healthy tissues: Comparison of PDR and HDR brachytherapy techniques. *Brachytherapy*. 2010;9(2):165-170. doi:10.1016/j.brachy.2009.08.007

40. van Limbergen E, Saw CB. Afterloading Technique. In: Brady LW, Yaeger TE, eds. *Encyclopedia of Radiation Oncology*. Springer Berlin Heidelberg; 2013:6. doi:10.1007/978-3-540-85516-3_427

41. Pignol JP, Keller B, Rakovitch E, Sankreacha R, Easton H, Que W. First report of a permanent breast 103Pd seed implant as adjuvant radiation treatment for early-stage breast cancer. *Int J Radiat Oncol Biol Phys*. 2006;64(1):176-181. doi:10.1016/j.ijrobp.2005.06.031

42. Kolhatkar AG, Jamison AC, Litvinov D, Willson RC, Lee TR. *Tuning the Magnetic Properties of Nanoparticles*. Vol 14.; 2013. doi:10.3390/ijms140815977

43. Jun YW, Seo JW, Cheon J. Nanoscaling laws of magnetic nanoparticles and their applicabilities in biomedical sciences. *Acc Chem Res*. 2008;41(2):179-189. doi:10.1021/ar700121f

44. Santoyo Salazar J, Perez L, De Abril O, et al. Magnetic iron oxide nanoparticles in 10-40 nm range: Composition in terms of magnetite/maghemite ratio and effect on the magnetic properties. *Chem Mater*. 2011;23(6):1379-1386. doi:10.1021/cm103188a

45. Chung SH, Hoffmann A, Bader SD, et al. Biological sensors based on Brownian relaxation of magnetic nanoparticles. *Appl Phys Lett*. 2004;85(14):2971-2973. doi:10.1063/1.1801687

46. Lartigue L, Innocenti C, Kalaivani T, et al. Water-dispersible sugar-coated iron oxide nanoparticles. An evaluation of their relaxometric and magnetic hyperthermia properties. *J Am Chem Soc*. 2011;133(27):10459-10472. doi:10.1021/ja111448t

47. Jeun M, Lee S, Kyeong Kang J, et al. Physical limits of pure superparamagnetic Fe_3O_4 nanoparticles for a local hyperthermia agent in nanomedicine. *Appl Phys Lett*. 2012;100(9):3-7. doi:10.1063/1.3689751

48. Fortin JP, Wilhelm C, Servais J, Ménager C, Bacri JC, Gazeau F. Size-sorted anionic iron oxide nanomagnets as colloidal mediators for magnetic hyperthermia. *J Am Chem Soc*. 2007;129(9):2628-2635. doi:10.1021/ja067457e

49. Zhen G, Muir BW, Moffat BA, et al. Comparative study of the magnetic behavior of spherical and cubic superparamagnetic iron oxide nanoparticles. *J Phys Chem C*. 2011;115(2):327-334. doi:10.1021/jp104953z

50. Noh SH, Na W, Jang JT, et al. Nanoscale magnetism control via surface and exchange anisotropy for optimized ferrimagnetic hysteresis. *Nano Lett*. 2012;12(7):3716-3721. doi:10.1021/nl301499u

51. Guardia P, Di Corato R, Lartigue L, et al. Water-soluble iron oxide nanocubes with high values of specific absorption rate for cancer cell hyperthermia treatment. *ACS Nano*. 2012;6(4):3080-3091. doi:10.1021/nn2048137

52. Lee JH, Huh YM, Jun YW, et al. Artificially engineered magnetic nanoparticles for ultra-sensitive molecular imaging. *Nat Med*. 2007;13(1):95-99. doi:10.1038/nm1467

53. Zeng H, Sun S, Li J, Wang ZL, Liu JP. Tailoring magnetic properties of core/shell nanoparticles. *Appl Phys Lett*. 2004;85(5):792-794. doi:10.1063/1.1776632

54. Ye F, Laurent S, Fornara A, et al. Uniform mesoporous silica coated iron oxide nanoparticles as a highly efficient, nontoxic MRI T(2) contrast agent with tunable proton relaxivities. *Contrast Media Mol Imaging*. 2012;7(5):460-468.

doi:10.1002/cmmi.1473

55. Bhat R, Want B, Firdous A, Dar GN. Probing of electric and magnetic properties of holmium doped iron oxide nanoparticles. *J Mater Sci Mater Electron*. 2018;29(22):19472-19483. doi:10.1007/s10854-018-0077-y

56. Fauth K (University of W. What_is_quenching_of_orbital_angular_momentum @ www.researchgate.net. Published 2017. Accessed November 6, 2020. https://www.researchgate.net/post/What_is_quenching_of_orbital_angular_momentum

57. Huan W, Cheng C, Yang Y, Yuan H, Li Y. A study on the magnetic and photoluminescence properties of Eu n+ and Sm 3+ doped Fe 3O 4 nanoparticles. *J Nanosci Nanotechnol*. 2012;12(6):4321-4334. doi:10.1166/jnn.2012.6190

58. Rebodos RL, Vikesland PJ. Effects of oxidation on the magnetization of nanoparticulate magnetite. *Langmuir*. 2010;26(22):16745-16753. doi:10.1021/la102461z

59. Meng YY, Liu ZW, Dai HC, et al. Structure and magnetic properties of Mn(Zn)Fe 2-xRE xO 4 ferrite nano-powders synthesized by co-precipitation and refluxing method. *Powder Technol*. 2012;229:270-275. doi:10.1016/j.powtec.2012.06.050

60. Lee J, Yang W, Lee MG, et al. Effective local control of malignant melanoma by intratumoural injection of a beta-emitting radionuclide. *Eur J Nucl Med*. 2002;29(2):221-230. doi:10.1007/s00259-001-0696-y

61. Kattel K, Park JY, Xu W, et al. A facile synthesis, in vitro and in vivo MR studies of d-glucuronic acid-coated ultrasmall Ln2O3 (Ln = Eu, Gd, Dy, Ho, and Er) nanoparticles as a new potential MRI contrast agent. *ACS Appl Mater Interfaces*. 2011;3(9):3325-3334. doi:10.1021/am200437r

62. Betke A, Kickelbick G. Bottom-up, wet chemical technique for the continuous synthesis of inorganic nanoparticles. *Inorganics*. 2014;2(1):1-15. doi:10.3390/inorganics2010001

63. Swihart MT. Vapor-phase synthesis of nanoparticles. *Curr Opin Colloid Interface Sci*. 2003;8(1):127-133. doi:https://doi.org/10.1016/S1359-0294(03)00007-4

64. Feng J. *Scalable Spark Ablation Synthesis of Nanoparticles: Fundamental Considerations and Application in Textile Nanofinishing*.; 2016. doi:10.4233/uuid

65. Nikam A V, Prasad BL V, Kulkarni AA. Wet chemical synthesis of metal oxide nanoparticles: a review. *CrystEngComm*. 2018;20(35):5091-5107. doi:10.1039/C8CE00487K

66. Zia M, Phull AR, Ali JS. Synthesis, characterization, applications, and challenges of iron oxide nanoparticles. *Powder Technol*. 2016;7(6):49-67.

67. Meuller BO, Messing ME, Engberg DLJ, et al. Review of spark discharge generators for production of nanoparticle aerosols. *Aerosol Sci Technol*. 2012;46(11):1256-1270. doi:10.1080/02786826.2012.705448

68. Sharaf A. Industrial Internship Report VSparticle. Published online 2017.

69. Tabrizi NS, Ullmann M, Vons VA, Lafont U, Schmidt-Ott A. Generation of nanoparticles by spark discharge. *J Nanoparticle Res*. 2009;11(2):315-332. doi:10.1007/s11051-008-9407-y

70. Tabrizi NS, Ullmann M, Vons VA, Lafont U, Schmidt-Ott A. *Generation of Nanoparticles by Spark Discharge Thesis*. Vol 11.; 2009. doi:10.1007/s11051-008-9407-y

71. Laban V. Introduction to VSP G1, the Nanoparticle Generator for research use. 2016;(November). https://www.researchgate.net/publication/311196744

72. Pfeiffer T V., Feng J, Schmidt-Ott A. New developments in spark production of nanoparticles. *Adv Powder Technol*. 2014;25(1):56-70. doi:10.1016/j.apt.2013.12.005

73. Schwyn S, Garwin E, Schmidt-Ott A. Aerosol generation by spark discharge. *J Aerosol Sci*. 1988;19(5):639-642. doi:10.1016/0021-8502(88)90215-7

74. Helsper C, Mölter W, Löffler F, Wadenpohl C, Kaufmann S, Wenninger G. Investigations of a new aerosol generator for the production of carbon aggregate particles. *Atmos Environ Part A, Gen Top*. 1993;27(8):1271-1275. doi:10.1016/0960-1686(93)90254-V

75. Weber AP, Baltensperger U, Gäggeler HW, Schmidt-Ott A. In situ characterization and structure modification of agglomerated aerosol particles. *J Aerosol Sci*. 1996;27(6):915-929. doi:10.1016/0021-8502(96)00013-4

76. Wittmaack K. Deriving the mean primary-particle diameter and related quantities from the size distribution and the gravimetric mass of spark generated nanoparticles. *J Nanoparticle Res*. 2007;9(2):191-200. doi:10.1007/s11051-006-9127-0

77. Byeon JH, Park JH, Hwang J. Spark generation of monometallic and bimetallic aerosol nanoparticles. *J Aerosol Sci*. 2008;39(10):888-896. doi:10.1016/j.jaerosci.2008.05.006

78. Messing ME, Dick KA, Wallenberg LR, Deppert K. Generation of size-selected gold nanoparticles by spark discharge - For growth of epitaxial nanowires. *Gold Bull*. 2009;42(1):20-26. doi:10.1007/BF03214902

79. Seipenbusch M, Weber AP, Schiel A, Kasper G. Influence of the gas atmosphere on restructuring and sintering kinetics of nickel and platinum aerosol nanoparticle agglomerates. *J Aerosol Sci*. 2003;34(12):1699-1709. doi:10.1016/S0021-8502(03)00355-0

80. Horvath H, Gangl M. A low-voltage spark generator for production of carbon particles. *J Aerosol Sci*. 2003;34(11):1581-1588. doi:10.1016/S0021-8502(03)00193-9

81. Yun K, Lee J, Nam HS. Effect of Temperature on Coalescence Behavior of Unsupported Gold Nanoparticles. *Electron Mater Lett*. 2019;15(1):133-139. doi:10.1007/s13391-018-0090-6

82. Antoniammal P, Arivuoli D. Size and shape dependence on melting temperature of gallium nitride nanoparticles. *J Nanomater*. 2012;2012. doi:10.1155/2012/415797

83. Kamachali RD. Surface-Induced Phase Transition

During Coalescence of Au Nanoparticles: A Molecular Dynamics Simulation Study. 2019;(April 2008):1-15. http://arxiv.org/abs/1902.01750

84. Zachariah MR, Carrier MJ. Molecular dynamics computation of gas-phase nanoparticle sintering: A comparison with phenomenological models. *J Aerosol Sci*. 1999;30(9):1139-1151. doi:10.1016/S0021-8502(98)00782-4

85. Pfeiffer TV. *Spark Ablation Proefschrift*.; 2014.

86. Conde J, Doria G, Baptista P. Noble Metal Nanoparticles Applications in Cancer. *J Drug Deliv*. 2012;2012:1-12. doi:10.1155/2012/751075

87. Koch D, Weber AP. Separation of gas-borne nanoparticles in bubble columns. *J Aerosol Sci*. 2012;53:61-75. doi:10.1016/j.jaerosci.2012.05.012

88. Charvet A, Bardin-Monnier N, Thomas D. Can bubble columns be an alternative to fibrous filters for nanoparticles collection? *J Hazard Mater*. 2011;195:432-439. doi:10.1016/j.jhazmat.2011.08.064

89. Cadavid-Rodriguez MC, Charvet A, Bemer D, Thomas D. Optimization of bubble column performance for nanoparticle collection. *J Hazard Mater*. 2014;271:24-32. doi:10.1016/j.jhazmat.2014.01.040

90. McDonald JE. The Mechanics of Aerosols. N. A. Fuchs. Translated from the Russian edition (Moscow) by R. E. Daisley and Marina Fuchs. C. N. Davies, Ed. Pergamon, London; Macmillan, New York, 1964. xiv + 408 pp. Illus. $17.50. *Science (80-)*. 1964;146(3647):1033-1034. doi:10.1126/science.146.3647.1033-b

91. Bronckhorst. EL-FLOW Select F-201CB.

92. Abràmoff MD, Magalhães PJ, Ram SJ. Image processing with imageJ. *Biophotonics Int*. 2004;11(7):36-41. doi:10.1201/9781420005615.ax4

93. Klencsár Z. Mössbauer spectrum analysis by Evolution Algorithm. *Nucl Instruments Methods Phys Res Sect B Beam Interact with Mater Atoms*. 1997;129(4):527-533. doi:10.1016/S0168-583X(97)00314-5

94. Taurozzi JS, Hackley VA, Wiesner MR. Ultrasonic dispersion of nanoparticles for environmental, health and safety assessment issues and recommendations. *Nanotoxicology*. 2011;5(4):711-729. doi:10.3109/17435390.2010.528846

95. Instruments P. Centering ring with sintered metal filter , pore size 20 μm , FKM / stainless steel , DN 25 ISO-.

96. Instruments P. Centering Ring with Sintered Metal Filter , Stainless steel. :1-3.

97. Bhattacharjee S. DLS and zeta potential - What they are and what they are not? *J Control Release*. 2016;235:337-351. doi:10.1016/j.jconrel.2016.06.017

98. Malvern, Instruments M. Dynamic Light Scattering : An Introduction in 30 Minutes. *Tech Note MRK656-01*. Published online 2011:1-8. http://scholar.google.com/scholar?hl=en&btnG=Search&q=intitle:Dynamic+Light+Scattering+:+An+Introduction+in+30+Minutes#3

99. Shrestha S, Wang B, Dutta P. Nanoparticle processing: Understanding and controlling aggregation. *Adv Colloid Interface Sci*. 2020;279:102162. doi:10.1016/j.cis.2020.102162

100. Gray EW, Pharney JR. Electrode erosion by particle ejection in low-current arcs. *J Appl Phys*. 1974;45(2):667-671. doi:10.1063/1.1663300

101. Monochromators FS. Basic XRD Course PANalytical. Published online 2013:1-23.

102. Mos YM, Vermeulen AC, Buisman CJN, Weijma J. X-Ray Diffraction of Iron Containing Samples: The Importance of a Suitable Configuration. *Geomicrobiol J*. 2018;35(6):511-517. doi:10.1080/01490451.2017.1401183

103. Muhammed Shafi P, Chandra Bose A. Impact of crystalline defects and size on X-ray line broadening: A phenomenological approach for tetragonal SnO2 nanocrystals. *AIP Adv*. 2015;5(5). doi:10.1063/1.4921452

104. Benten J van. SYNTHESIS OF SUPERPARAMAGNETIC FEXOY NANOPARTICLES BY SPARK ABLATION. Published online 2018.

105. Kucheryavy P, He J, John VT, et al. Superparamagnetic iron oxide nanoparticles with variable size and an iron oxidation state as prospective imaging agents. *Langmuir*. 2013;29(2). doi:10.1021/la3037007

106. Norek M, Pereira GA, Geraldes CFGC, Denkova A, Zhou W, Peters JA. NMR transversal relaxivity of suspensions of lanthanide oxide nanoparticles. *J Phys Chem C*. 2007;111(28):10240-10246. doi:10.1021/jp072288l

107. Bao Y, Sherwood JA, Sun Z. Magnetic iron oxide nanoparticles as: T 1 contrast agents for magnetic resonance imaging. *J Mater Chem C*. 2018;6(6):1280-1290. doi:10.1039/c7tc05854c

108. Brandt B, Schalow T, Laurin M, Schauermann S, Libuda J, Freund HJ. Oxidation, reduction, and reactivity of supported Pd nanoparticles: Mechanism and microkinetics. *J Phys Chem C*. 2007;111(2):938-949. doi:10.1021/jp0658086

109. Bugaev AL, Zabilskiy M, Skorynina AA, Usoltsev OA, Soldatov A V., Van Bokhoven JA. In situ formation of surface and bulk oxides in small palladium nanoparticles. *Chem Commun*. 2020;56(86):13097-13100. doi:10.1039/d0cc05050d

110. Kaech A. An Introduction To Electron Microscopy Instrumentation, Imaging and Preparation. *Cent Microsc Image Anal*. Published online 2013:1-26. http://www.zmb.uzh.ch/static/bio407/assets/Script_AK_2014.pdf

111. Bunaciu AA, Udriştioiu E gabriela, Aboul-Enein HY. X-Ray Diffraction: Instrumentation and Applications. *Crit Rev Anal Chem*. 2015;45(4):289-299. doi:10.1080/10408347.2014.949616

112. Hou X, Jones B. Inductively Coupled Plasma-Optical Emission Spectroscopy. *Anal Chem*. 1974;46(13):1110A-1120A. doi:10.1021/ac60349a722

113. Abd Mutalib M, Rahman MA, Othman MHD, Ismail AF, Jaafar J. *Scanning Electron Microscopy (SEM) and Energy-Dispersive X-Ray (EDX) Spectroscopy*. Elsevier B.V.; 2017. doi:10.1016/B978-0-444-63776-5.00009-7

114. Fultz B. Mössbauer Spectrometry. Published online 2011.

115. Buchner M, Höfler K, Henne B, Ney V, Ney A. Tutorial: Basic principles, limits of detection, and pitfalls of highly sensitive SQUID magnetometry for nanomagnetism and spintronics. *J Appl Phys*. 2018;124(16). doi:10.1063/1.5045299

116. Version H. an introduction. 2003;(September).

117. Albarqi HA, Wong LH, Schumann C, et al. HHS Public Access. 2019;13(6):6383-6395. doi:10.1021/acsnano.8b06542.Biocompatible

118. Le Pevelen DD. Small Molecule X-Ray Crystallography, Theory and Workflow. In: Lindon JC, ed. *Encyclopedia of Spectroscopy and Spectrometry (Second Edition)*. Second Edi. Academic Press; 2010:2559-2576. doi:https://doi.org/10.1016/B978-0-12-374413-5.00359-6

119. Speakman SA. Introduction to X-Ray Powder Diffraction Data Analysis. *Mater Sci*. Published online 1902:20. https://www.researchgate.net/file.PostFileLoader.html?id=58d22df3dc332d06c7245969&assetKey=AS%3A474618730422273%401490169331513

120. Bruker. Periodic Table of Elements and X-ray Energies. *Bruker Website*. Published online 2020:2. https://www.bruker.com/fileadmin/user_upload/8-PDF-Docs/X-rayDiffraction_ElementalAnalysis/HH-XRF/Misc/Periodic_Table_and_X-ray_Energies.pdf

Appendix A   logbook

IP address to access VSP control panel: 192.168.4.1

Desktop name: TUD210409

Day 1 (18/6/2020): Experiment to replicate results from internship report (A. Sharaf)

The reactor assembly was not disturbed. No electrode replacement or cleaning of the reactor assembly was done due to recent maintenance operation performed on the unit.

Steps to Start Nanoparticle Production
- Ensure the flow is zero before changing the water in the bubbling column (BC).
- Remove the topmost clamp to drain the water from the BC.
- Use milliQ water to clean the bubbling column.
- Pour 100ml of milliQ water into the bubbling column.
- Set the flow to 2 l/min and check for bubble flow response in the bypass. If there is any leak at any of the clamps or connections, bubble flow velocity will be very small in comparison to the set flow rate.
- Check for leaks using foam at all the clamp connections. Check if the bubbles increase in size.
- Adjust and correct the clamps or connections to avoid leaks. If there isn't any leak, set the flow rate and turn the knob down as fast as possible to direct the flow from bypass to bubbling column.
- If everything is okay, then set the voltage and current parameters. Press "Go".

Steps to Stop Nanoparticle Production
- Turn "Off" the particle generator.
- Turn the knob upwards as fast as you can while keeping the gas flow on. If you turn the flow off before turning the knob, water from the bubbling column will flow back and seep into the machine.
- Set the flow rate to zero.
- Remove the topmost clamp to collect the sample in plastic collection tubes (Red)- close to 80-90 ml of water with nanoparticles remained after 1 hour. Each batch is put into two collection tubes.
- Label the sample
- If there is excess sample in the column, drain it into the nanoparticle waste collection jar (it will be in the fume hood)
- Use milliQ water to clean the bubbling column.
- Drain the contaminated water into the nanoparticle waste collection jar.

Sample preparation for DLS
- Use a syringe to draw samples from the collection tube. (This step must be done inside the fume hood)
- Screw the 400nm filter at the tip of the syringe and transfer the sample in the syringe into a test tube. (This step must be done inside the fume hood)
- Cover the mouth of the test tube with a parafilm and label the sample.

(Note: Use gloves whenever you handle sample with nanoparticles and perform tasks in fume hood wherever necessary)

Date	Exp. No.	Voltage (kV)	Current (mA)	Flow (l/min)	Time	Pressure Reading (mbar) Limit: 1400mbar	Comments
	1 (100mL)	1	5	1	Start time: 11:58 pm End time: 12:58	1113	Batch 1a & 1b Check the excel. Only one peak was observed, and the largest size was around 198nm. The peak was observed around 41nm
	2 (100mL)	1	5	2	Start time: 13:45 End time: 14:45	1210	Batch 2a & 2b Check the excel. Only one peak was observed, and the largest size was around 300nm. The peak was observed around 34nm
18/6	3 (100mL)	0.7	2.5	2	Start time: 15:05 End time: 16:05	1098	Batch 3a & 3b Check the excel. Only one peak was observed, and the largest size was around 172nm. The peak was observed around 37nm
	4 (100mL)	1	7.5	2	9:45-10:49	1103	Batch 4.a & 4.b
	5 (100mL)	1.3	10	3	11:40-13:12	1125	Batch 5a & 5.b
19/6	6 (100mL)	1.3	10	4	13:53-15:23	1177	Batch 6a & 6B
	7 (100mL)	1.3	10	1	9:49-11:20	1125	Batch 7a & 7b Evaporated water = 5ml
	8 (100mL)	0.5	1.5	1	12:20-13:50	1112	Batch 8a & 8b Evaporated water = 3ml
22/6	9 (100mL)	0.7	2.5	1	14:00-15:30	1135	Batch 9a & 9b
	10 (100mL)	0.7	2.5	2			Batch 10a & 10b
23/6	11 (100mL)	0.7	5	2	12:30 - 9:30 (24/6)	1144	Batch 11 Evaporated water = 42ml unfiltered peak 22nm filtered 13nm

							frequ ency 170/95 resp
	12 (100mL)	1	5	2	11:00-16:00	1125	Batch12 Evaporated water = 15ml unfiltered peak 12, 48, 250 filtered peak 17, 70 freq 145/ 50 resp
24/6	13 (100mL)	1	5	2	16:30-10:15	1105	Batch 13 Evaporated water= 45ml unfiltered 20, 160 filtered 30,103 freq 500/280 resp
25/6	14 (100mL)	1	7	2	10:45-10:42 (26/6)	1215	Batch 14 Evaporated water= 55ml unfiltered 16, 62, 495 became 2 micrometer after 3 days filtered 11, 37 freq 550/280 resp first meas 26, scn 29
29/6	15 (100mL)	1	5	2	9:00-9:28	1091	Batch 15 evaporated water unfiltered 0.2, 2, 150 nm filtered 4,3 nm freq 650/340
30/6	16 (100mL)	1	5	2	09:54	1234	
6/7	17 (100mL)	1.3	10	1	9:05-14:10		Batch 17 Evaporated water= 3 ml Non-sonicated filtered - 249kHz 21,71nm Sonicated filtered - 411kHz 81nm
7/7	18 (100mL)	1.3	10	2	9:00-14:00	1098	Batch 18 Evaporated water= 5 ml Non-sonicated filtered - 260kHz

							8,62nm Sonicated filtered - 363kHz 70nm
8/7	19 (100mL)	1.3	10	0.5	11:00-16:00	1100	Batch 19 Evaporated water= 3 ml filtered - 247kHz 25,83nm
9/7	20 (100mL)	1.3	10	0.5	17:00-12:30 (9/7)	1088	Batch 20 Evaporated water= 15 ml Without dilution Non-sonicated filtered - 949kHz 9,80nm Sonicated filtered - 1316kHz 24,95nm With dilution and 10mM Nacl Non-sonicated filtered(1ml)+ mq(1ml) - 539kHz 17,75nm Non-sonicated filtered(1ml)+Nacl (1ml) - 594kHz 1.6,27,281nm Sonicated filtered (1ml)+ mq(1ml) - 668kHz 30,102nm Sonicated filtered(1ml)+Nacl(1ml - 747kHz 0.14,1.8,105nm
11/7	21 (220 ml)	1.3	5	0.7	12:00-12:00 (13/7)	1260	Batch 21 Evaporated water= 80ml Non-sonicated filtered - 759kHz 15,37,101nm Non-sonicated filtered(1ml)+ mq(1ml) - 410kHz 3.5,76nm Pressure reached upto

							1390 starting from 1320 at 2 l/min over a period of 20 hours. (Most likely due to blockage in filter)
15/7	22 (200 ml)	1.3	10	0.3	15:30-15:30(17/7)	1104	Batch 22 Evaporated water = 20ml Non-diluted & Filtered - 966kHz 2,76 Diluted (1ml sample+1ml MQ) & Filtered - 561 kHz 17,74,1069
17/7	23 (200 ml)	0.65	10	0.3	16:10-15:00 (20/7)	1126	Batch 23 Evaporated water=
(Thijs) Ho-FeO	24 (200)	0.65	10	3	12:00-experiment failed		Batch 24
27-7 (Thijs)	25 (200)	0.7	10	3	10:30-10:30 (30/7)	1133	Batch 25 Evaporated water=160ml 4Khz because of retention in filters. Concentration is far too low. However, some of it was visible on TEM. 4 filters used
12/08	26 (80mL)	1.3	10	1	11:00-9:00 (13/08)		Fe-Fe test sample to see if new filter works
14/08	27 (80mL)	1.3	10	1&2	8:40-16:30		Fe-Fe, see if we can improve the pressure by closing and opening the valve a lot of particles captured before the filter
17/08	28 (80mL)	1.3	10	1	10:20-15:10		Ho-Ho, immense pressure increase, not able to run for more than 5 hours
18/08	29 (80mL)	1.3	10	1	9:35-9:15 (20/08)		Bronze filter: Ho-Ho works very good. no pressure builtup, no particles inside the generator, white particles.

							Fe-Fe to see if many particles will get collected. much stuck to the walls and inside the filter
20/08	30 (80mL)	1.3	10	1	10:50-9:00 (24/08)		
24/08	31 (80mL)	1.3	10	1	11:45-9:00 (27/8)		Fe-Ho Very high concentration, both in the filter and column,
27/08	32 (80mL)	1.3	10	1	12:00-9:30		34 Fe-Fe high concentration, not exceptional much in the filter
07/09	33 (80mL)	1.3	10	1	12:00-14:00(11/08)		Very high concentration. Especially in the filter
14/09	34 (80mL)	1.3	10	1	10:00-10:00(17/09)		Way too low production because of electrode positions with respect to each other
25/09	35	1.3	10	1	2:15-	1060	Pd-Pd
27/10	36 (60mL)	1.3	10	1	24hrs		Fe-Fe high concentration
28/10	37 (60mL)	1.3	10	1	24hrs		Ho-Fe high concentration

Appendix B   Results

B.1   TEM

E12
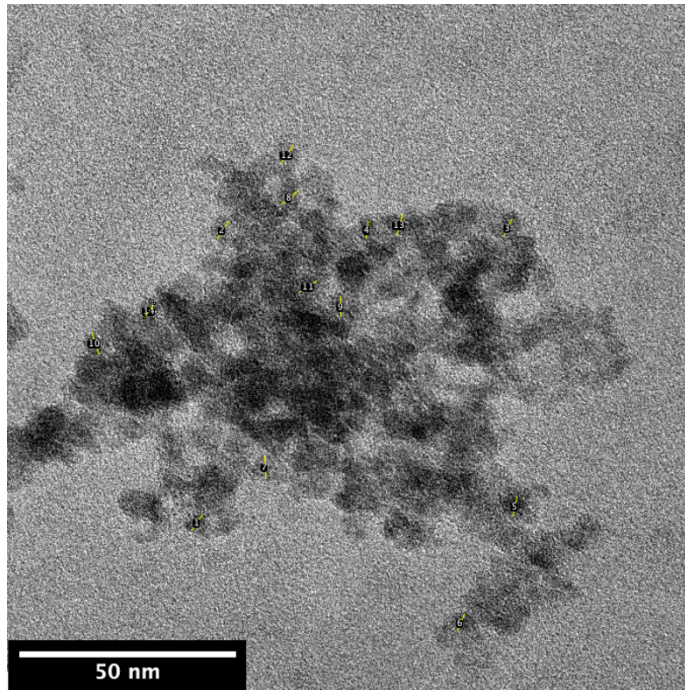
1	4.207
2	4.726
3	4.175
4	3.763
5	4.531
6	4.076
7	4.906
8	4.994
9	4.668
10	5.388
11	4.403
12	5.049
13	5.097
14	4.015
	4.57128571

E15
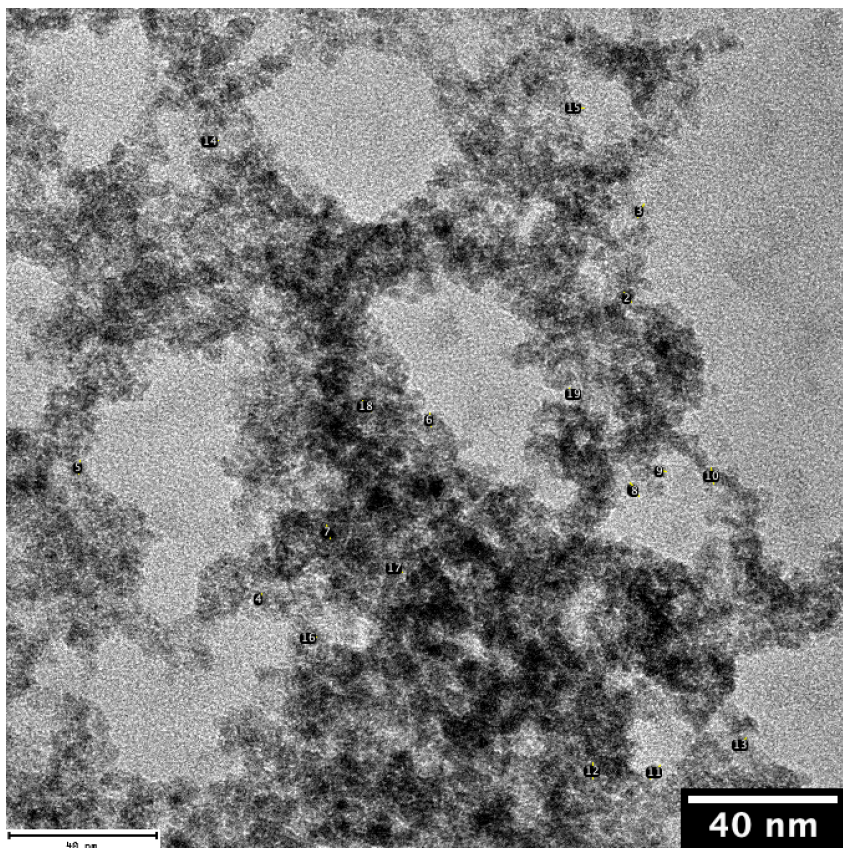
1	3.724
2	3.331
3	4.025
4	3.16
5	3.679
6	3.679
7	3.798
8	3.884
9	3.071
10	4.381
11	4.53
12	4.33
13	4.066
14	3.997
15	5.007
16	3.679
17	4.343
18	3.798
19	3.768
av	3.91

E13
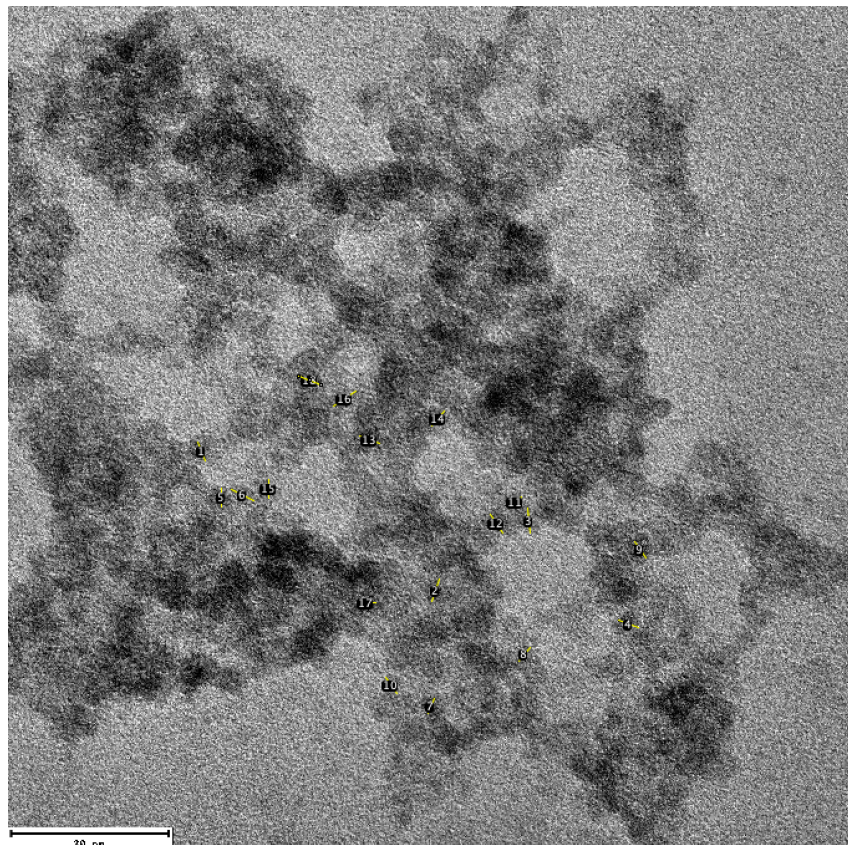
1	3.77
2	4.428
3	4.691
4	3.988
5	3.501
6	4.697
7	3.034
8	3.317
9	3.69
10	3.69
11	3.14
12	4.207
13	3.988
14	3.645
15	3.501
16	5.049
17	3.501
18	4.507
av	3.91

E36
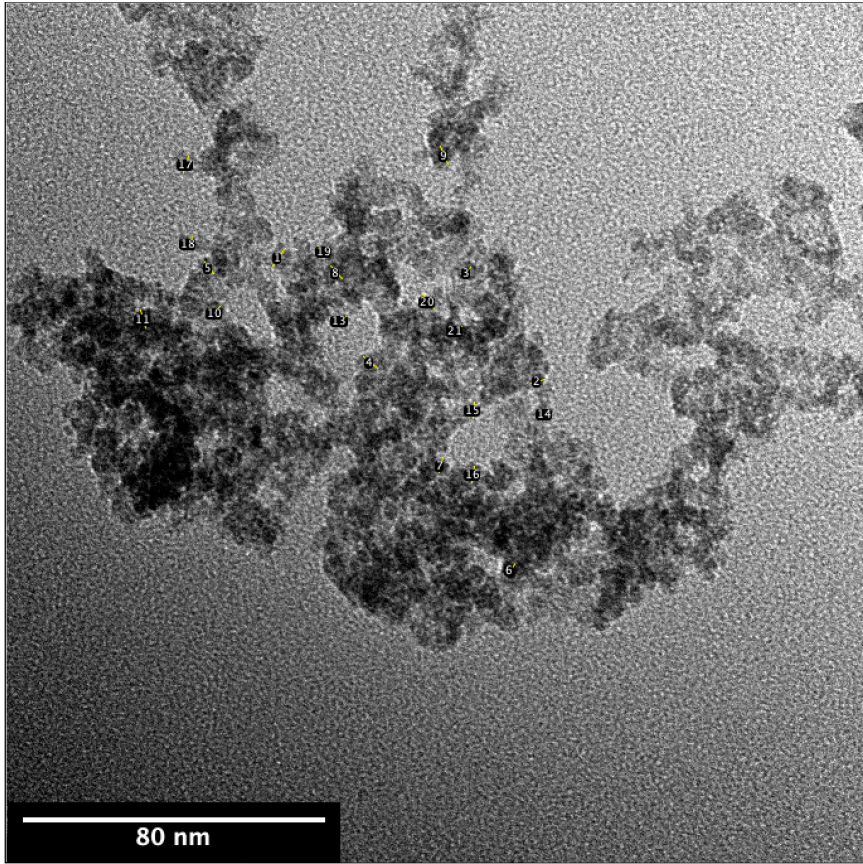
1	5.266
2	3.798
3	3.429
4	4.734
5	3.876
6	3.798
7	4.12
8	4.481
9	5.073
10	4.265
11	4.85
12	3.331
13	4.08
14	4.066
15	4.343
16	4.381
17	4.53
18	3.724
19	4.265
20	4.996
21	3.798
	4.24780952
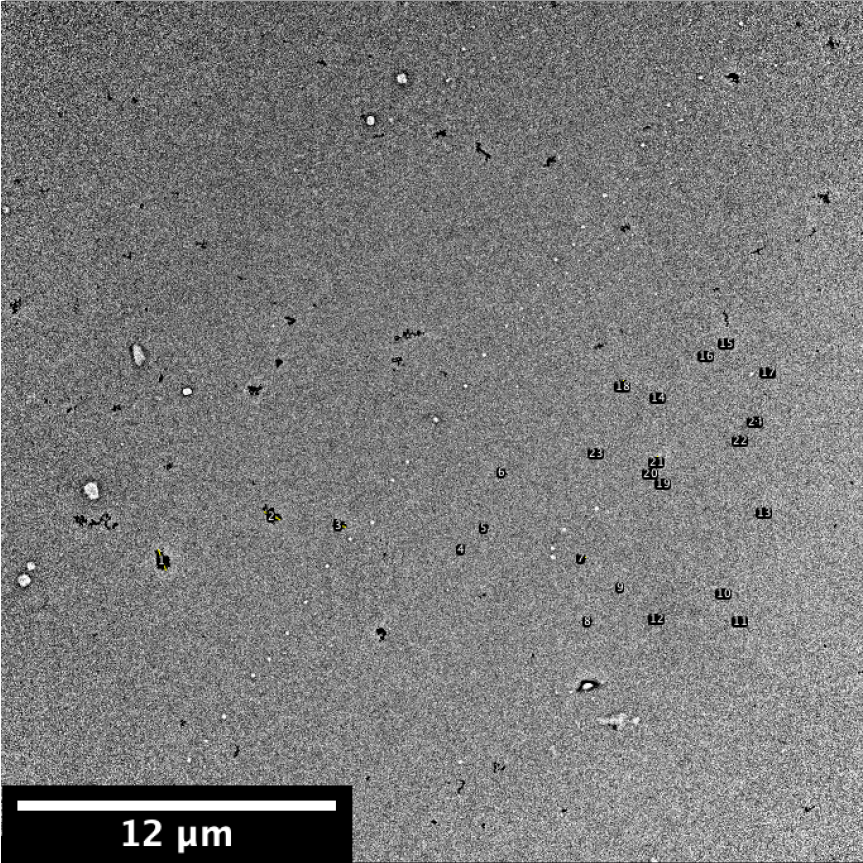
	Length microm		
1	0.811	14	0.206
2	0.637	15	0.329
3	0.451	16	0.142
4	0.224	17	0.149
5	0.19	18	0.413
6	0.258	19	0.085
7	0.17	20	0.312
8	0.208	21	0.381
9	0.057	22	0.067
10	0.135	23	0.071
11	0.096	24	0.05
12	0.057		
13	0.23		0.27107692

E37
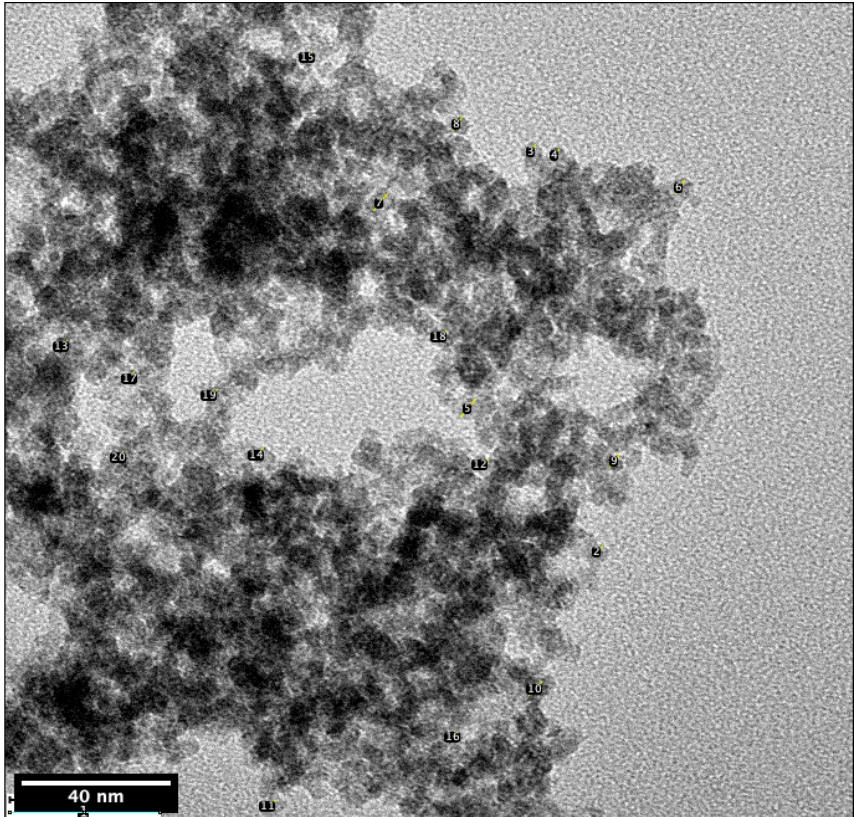
1	40.303
2	3.798
3	4.076
4	3.085
5	6.485
6	4.496
7	5.862
8	4.19
9	4.441
10	5.184
11	4.996
12	4.734
13	4.011
14	4.481
15	3.603
16	3.071
17	3.972
18	4.265
19	4.396
20	3.82
	4.367
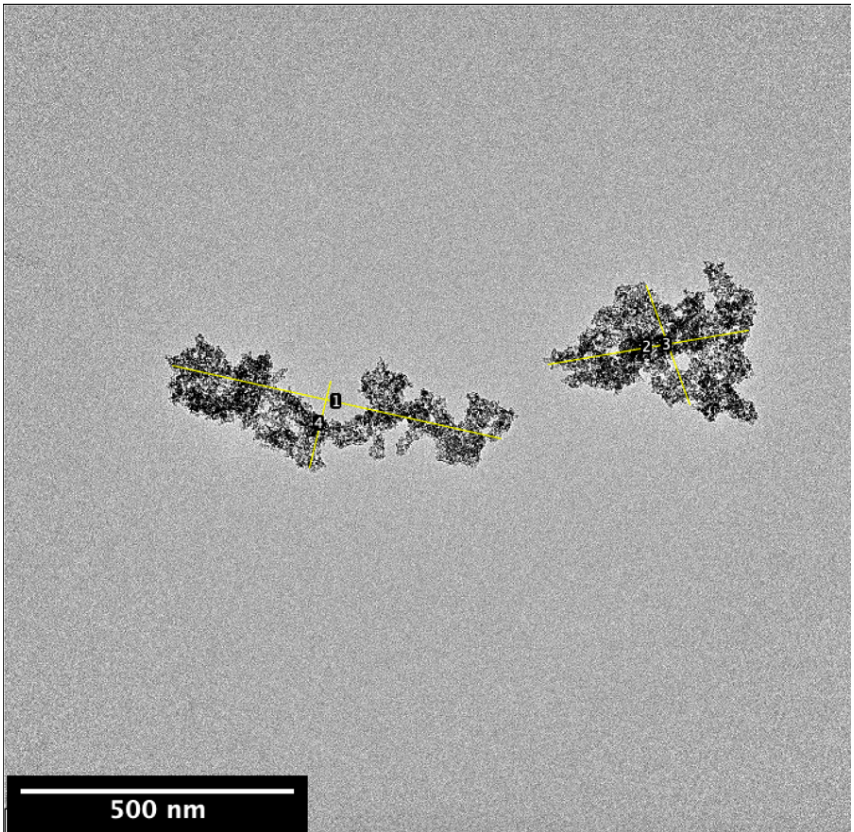
	Length
1	613.421
2	370.267
3	235.783
4	165.418

E33 micro bubbler
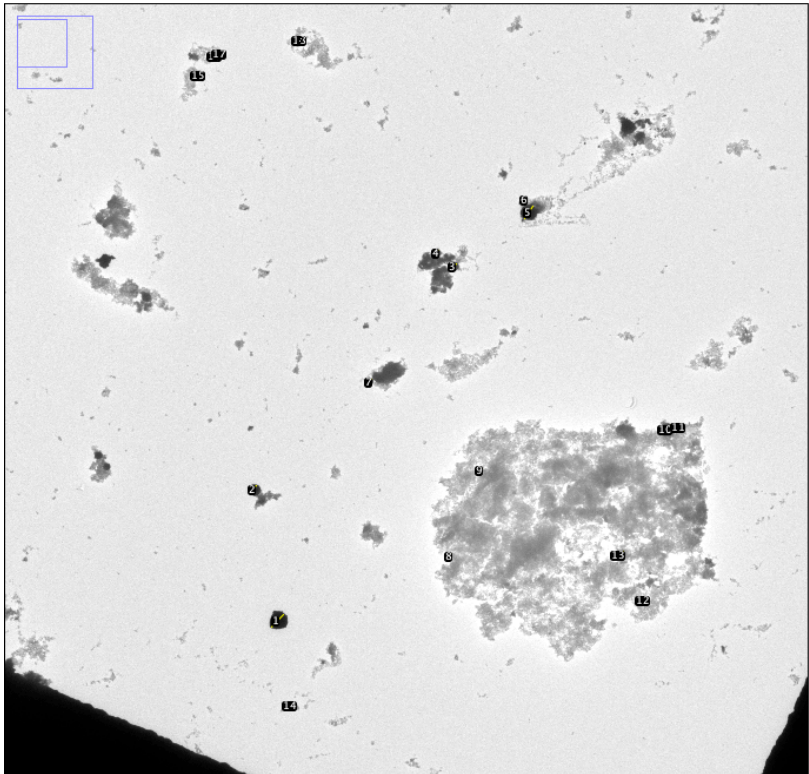
1	1.414
2	0.806
3	0.739
4	0.616
5	1.238
6	0.234
7	0.448
8	0.49
9	0.29
10	1.135
11	0.67
12	0.31
13	0.809
14	0.487
15	0.613
16	0.212
17	0.19
18	0.342
av	0.61 micro
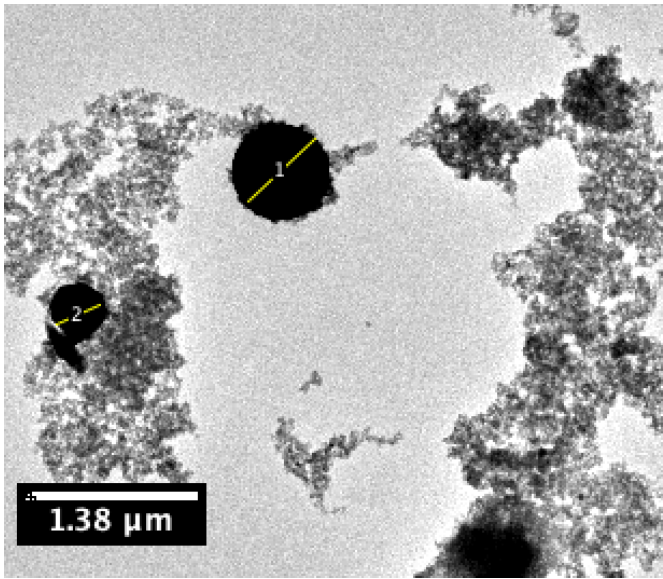
1	0.788
2	0.416

E33 column
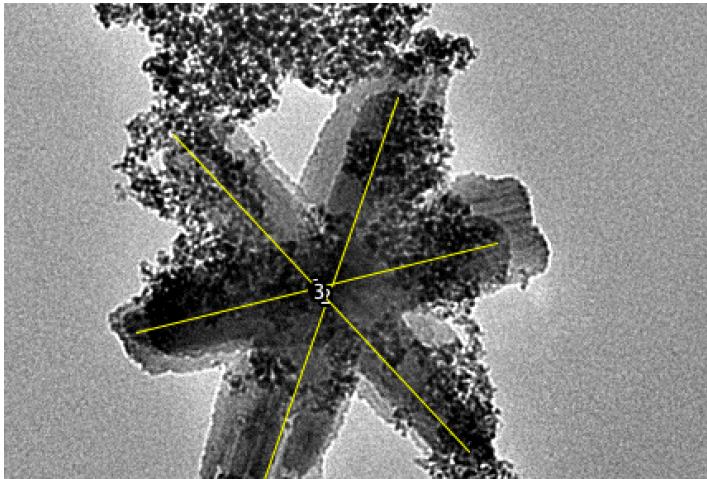
1	0.359
2	0.411
3	0.419
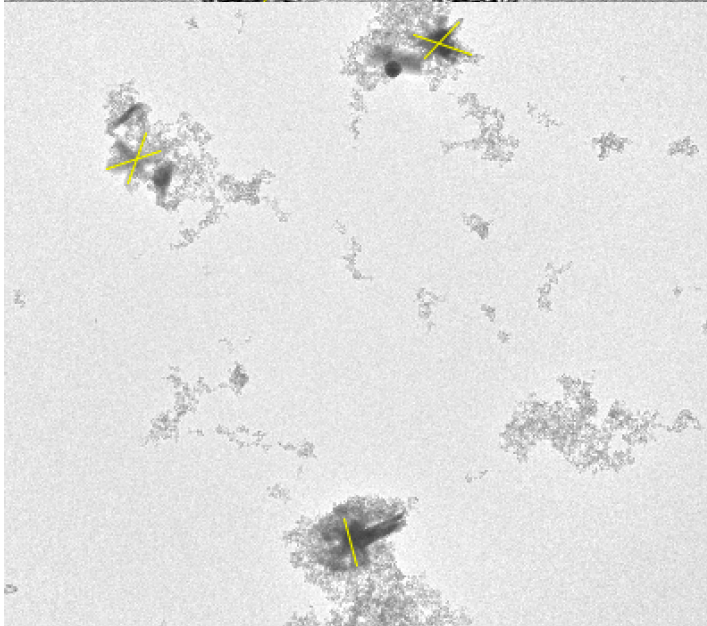
1	0.435
2	0.409
3	0.465
4	0.379
5	0.37
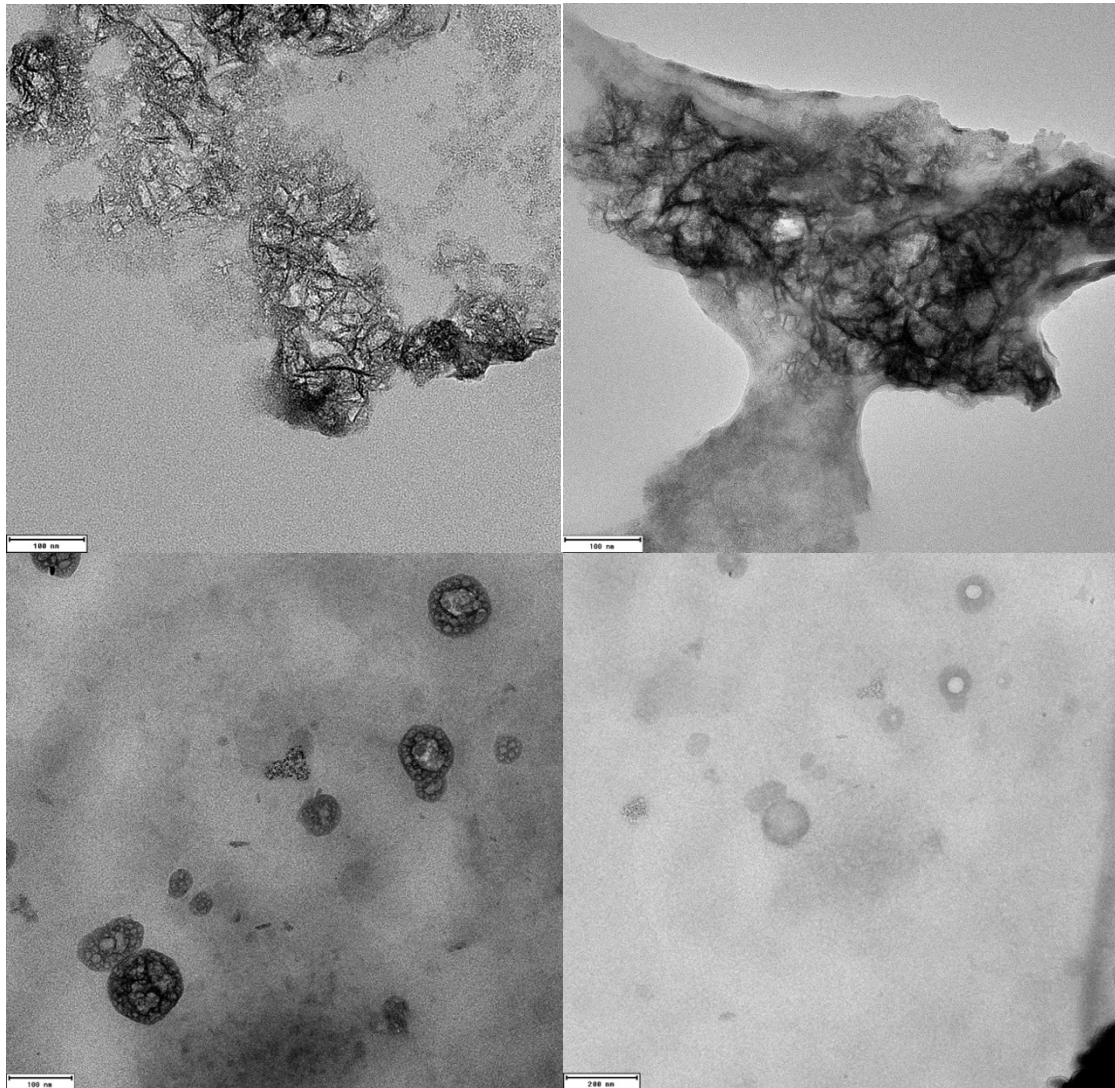
B.2   DLS
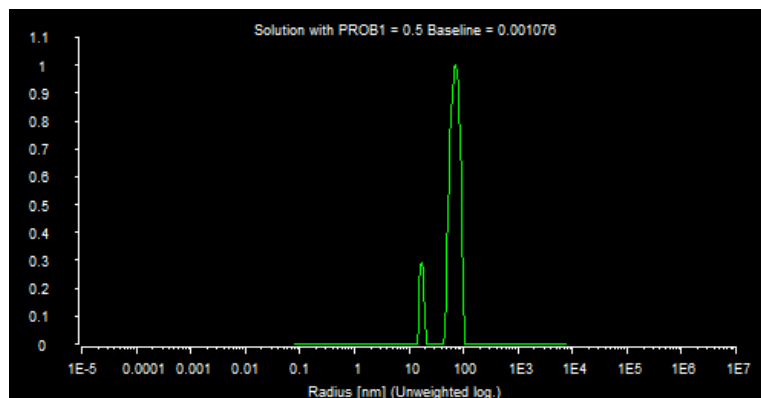
Exp 12 V=1kv, I=5mA, F=2.2L/min
        The average count rate: 50 kHz.
Peak 1, from 14.92 nm to 19.72nm
Mean Peak Position: 17.1 nm
Peak 2, from 36.05 nm to 109.8nm
Mean Peak Position: 59.5 nm
Peak 3, from 149 nm to 442 nm
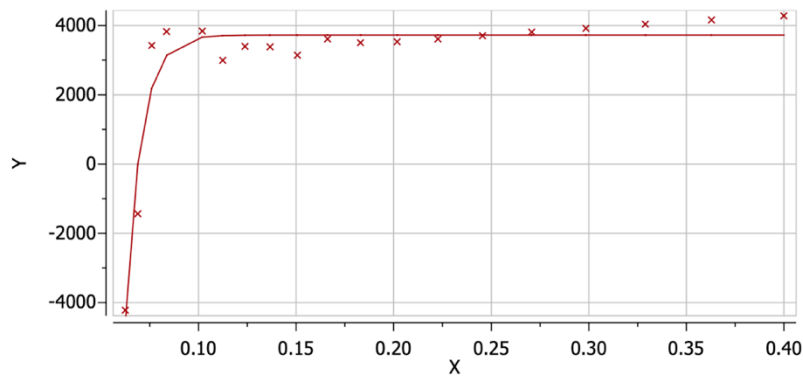Mean Peak Position: 271.8 nm
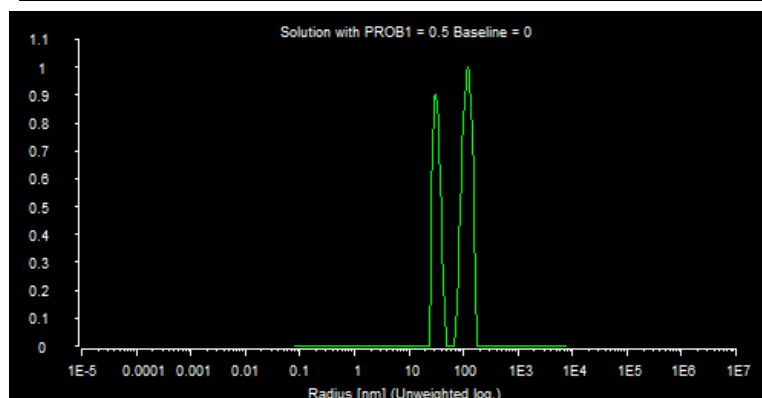
Exp 13 V=1kv, I=5mA, F=2.2L/min

The average count rate: 272 kHz.
Peak 1, from 24.8 nm to 47.6 nm
Mean Peak Position: 32.45 nm
Peak 2, from 72.3 nm to 166.9 nm
Mean Peak Position: 115.6 nm
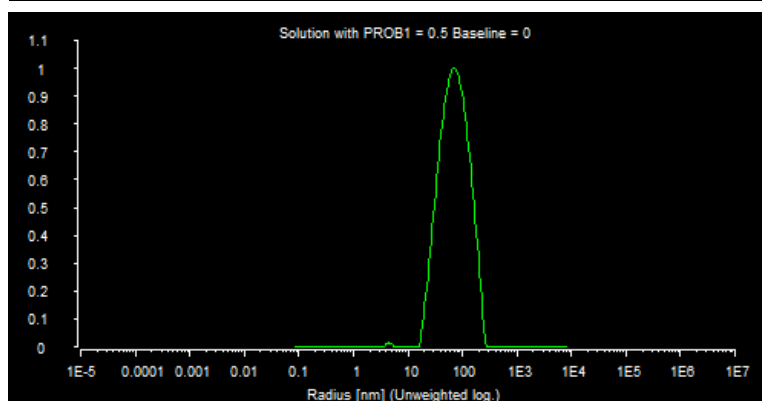
Exp 15: V=1kv, I=5mA, F=2.2L/min

The average count rate: 336 kHz.
Peak 1, from 3.818 nm to 5.284 nm
Mean Peak Position: 4.795 nm
Peak 2, from 16.1 nm to 260.9 nm
Mean Peak Position: 69.84 nm

B.3 NMR

Y' = B+F*exp(-X*G)
B=3725; F=-2.033e+7; G=124.8;
Error: 11.95
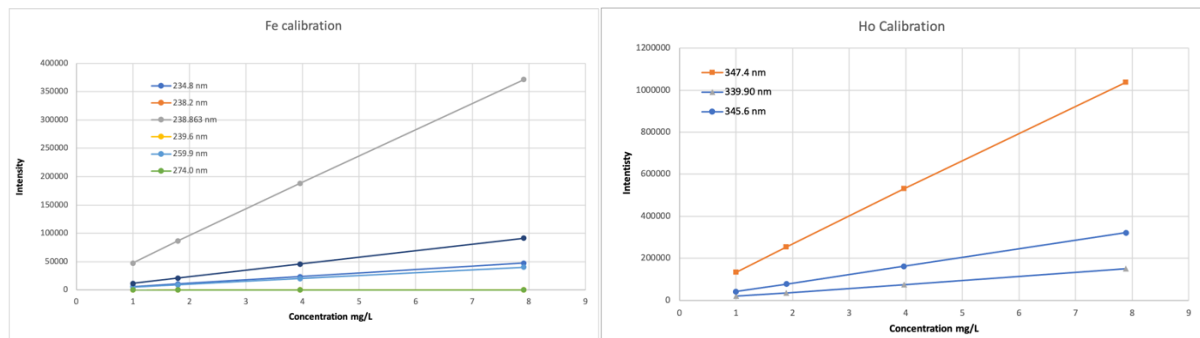
B.4 Concentration calculation

$$r = m_{Ho}/m_{Fe}$$

$$M = r * (271.29) + 55.85$$

$$C = (m_{Fe} + m_{Ho})/M$$

Where r is the ratio between the Ho and Fe mass. M is the molar mass calculated for the expected molecule structure. C is the concentration.

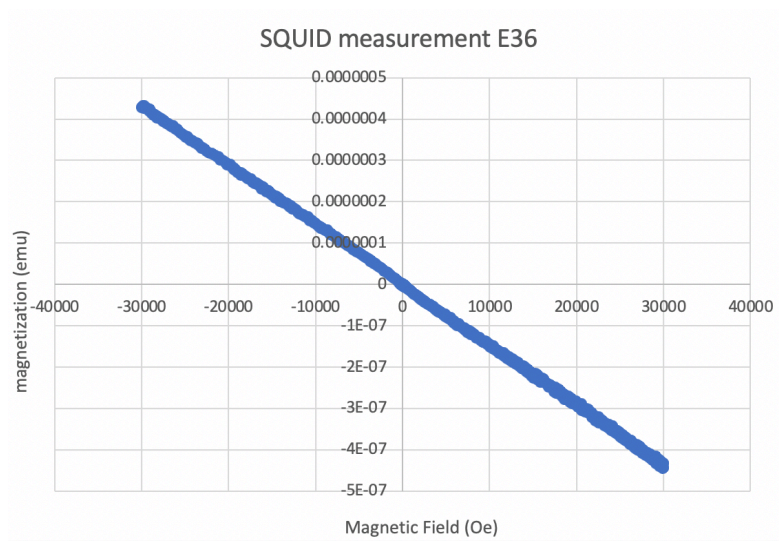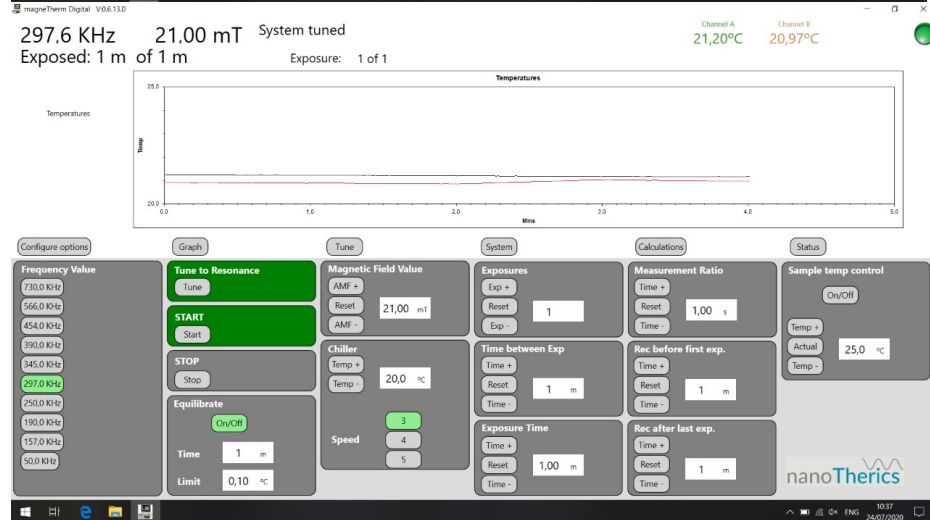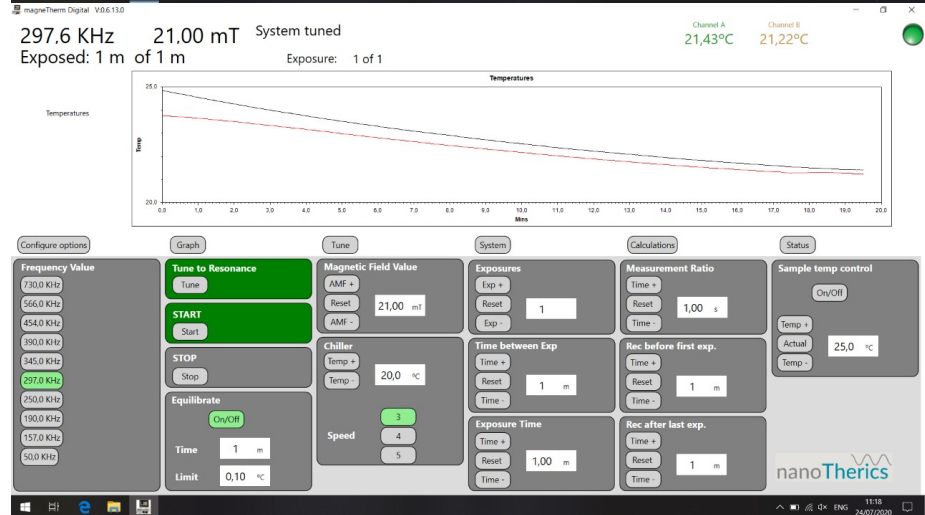## B.5 ICP Calibrations

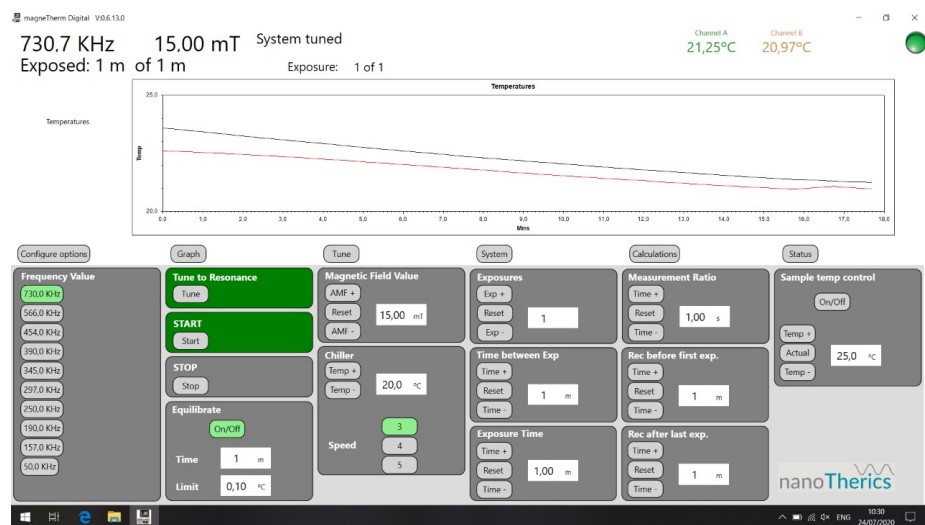## B.6   SQUID diamagnetic Water

Figure 37 Diamagnetic curve found for low concentration iron oxide in water.

B.7   Calometric measurements

Appendix C   Extra information

C.1   Measurement Techniques

Dynamic Light Scattering (DLS)

Brownian motion causing diffusion of nanoparticles is dependent on the size of a particle. The diffusion coefficient can be measured by DLS. For a DLS measurement, a constant monochromatic signal is sent out and the detector compares the signals via a correlator. The change of a signal is correlated with the size of a particle. Small particles will have a rapidly changing intensity, whereas larger ones will give a smoother intensity change. Furthermore, the correlation function tells something about the size distribution of the sample. A steep correlation function shows a monodisperse sample and increasing polydispersity is seen by extended correlation decay. Software is used to calculate the size distribution from the correlation function. [76]

Transmission Electron Microscopy (TEM)

The Transmission Electron Microscope (TEM) uses a constant beam of electrons radiated on a sample and measures the number of transmitted electrons. This way, the TEM gives great insight into the structure and morphology of the samples. With the TEM, the DLS obtained values for particle sizes can be verified.[30]

X-Ray Diffraction Spectroscopy (XRD)

XRD is used to characterize the crystal structure of the samples. It is used to analyze the composition and oxidation state of the NPs. The sample is irradiated with X-rays and the crystal structure causes constructive interference on the diffracted X-rays. The constructive interference is measured as an intensity peak on the diffractometer. The peaks form a fingerprint of periodic atomic arrangements. This fingerprint is matched with a database to determine which substances are present.[110]

Inductively Coupled Plasma Optical Mass Spectroscopy (ICP OMS)

Inductively coupled plasma optical mass spectroscopy (ICP OMS) is a very powerful method to analyze the element content of a sample. ICP OMS uses the heat of plasma to atomize and ionize a sample. When an atom is brought into the plasma, an electron of the atom may excite to a higher orbit. Upon relaxation of this excited electron, a photon is emitted with characteristic energy. The amount of characteristic energy measured by optical spectroscopy corresponds with the mass percentage of the initial sample.[111]

Scanning Electron Microscopy (SEM) & Energy Dispersive X-ray (EDX/EDS)

The Scanning Electron Microscope (SEM) scans the surface of a sample with a focused electron beam. By measuring the interactions from the electrons, an image of the surface topography can be made. By irradiating the sample with electrons, electrons are knocked out of the electron shells. By measuring the characteristic X-rays of electrons which fill this vacancy, qualitative and quantitative information can be obtained about the content of the sample.[112]

Mössbauer Spectroscopy

Mossbauer spectroscopy is a very powerful tool for the investigation of magnetic nanomaterials. Because a fraction of interactions between γ-rays and a solid-state material occur recoil-less, resonance studies can be done on the material. The isomer shift (IS) gives

information about the electron charge density, the quadrupole splitting (QS) refers to the electron's crystal structure. The hyperfine magnetic field originates from the unpaired electron density at the nucleus, defining the magnetic properties.[113]

Superconducting Quantum Interference Device (SQUID)

A superconducting quantum interference device (SQUID) magnetometer uses the periodicity of the diffusive quantum regime in a superconductor to measure the magnetization of a sample. The sample is placed inside the magnetic field of a coil. By moving the sample inside the coil, a flux and therefore, a current is induced. This current can be measured by the SQUID.[114] The measurement provides a magnetization curve as a function of the magnetic field.

Nuclear Magnetic Resonance (NMR)

The NMR measurement provides the longitudinal and transverse relaxation times of the samples. NMR spectrometer applies an RF pulse to excite the sample protons. During the relaxation, the longitudinal and transversal magnetizations are measured and these are fitted for the function given in Figure 6B.

Heating measurement

The sample will be put inside a coil through which an alternating current will induce an AMF. As a result of the AMF, the nanoparticles should get heated. Two probes measure the heating, one on the bottom, one in the middle of the sample holder. A significant temperature difference indicates the precipitation of the NPs during the measurement. By measuring the heat differences when heating up and the cooling down process, the specific absorption rate (SAR) can be calculated.[115,116]

C.2 XRD

XRD is a rapid analytical technique used for phase identification of crystalline material. It is based on the constructive interference of reflected waves. Bragg's law is given by the following equation:

$$n\lambda = 2dsin\theta$$

Where n is an integer, λ is the wavelength of the X-ray source, d is the distance between crystal structure layers and θ is the angle between the crystal structure layer and the incoming waves. Bragg's law defines the angles for which constructive interference can be found.

An XRD measurement measures the intensity of the reflected beam for a set of angles and therefore gives information about the distances d between the crystal structure layers. In Figure 38 the constructive interfering beams are visualised.
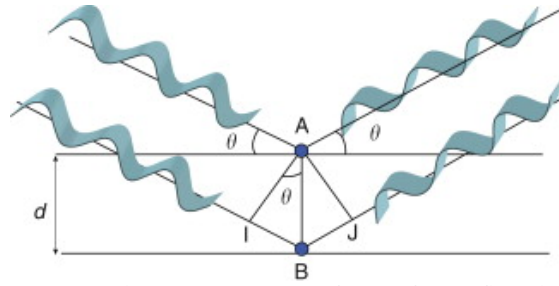
Figure 38 Bragg's law constructive interference from reflected waves[117].

For a qualitative analysis of the reference pattern, the peaks of the obtained reference pattern are compared with a database. Here the position and intensity of the peaks are compared with peaks of previously measured material and can be matched. In Figure 39 an XRD measurement of a TiO_2 and Al_2O_3 sample is shown where the peaks are matched with the pattern.
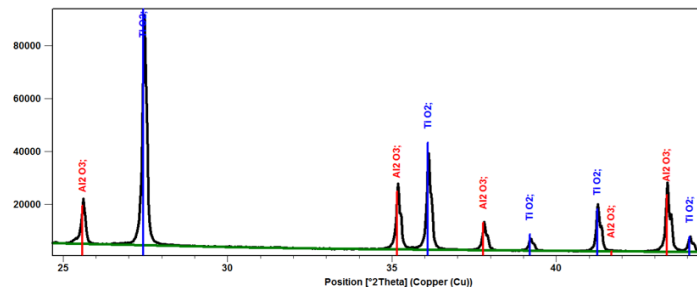

Figure 39 XRD pattern shows peaks for different phases which are matched with the database[118]

The intensity of the peaks does not correspond with the amount the phase occurs with, since every phase will interact with the incoming beams in its own way. The sample analysed in Figure 39 contains the same amount of TiO_2 and Al_2O_3, but TiO_2 diffract the X-rays more efficiently[119]. Therefore, the blue (TiO_2) peaks have a higher intensity. If broadening of the peaks occurs, this often means that there is an inhomogeneous composition of a solid solution or alloy or that there are defects in the crystal structure.

The X-rays are emitted from a Copper X-ray tube at certain energies $K\alpha$ and $K\beta$. For diffraction measurements, only $K\alpha$ is wanted, so the $K\beta$ are filtered out. Certain elements in the sample are able to absorb these photons and will then emit new characteristic X-rays. Because the photons emitted by these elements are close to Cu $K\alpha$, they will be detected as if they were a diffracted beam and will increase the background signal. This is called fluorescence and can be prevented in several ways.
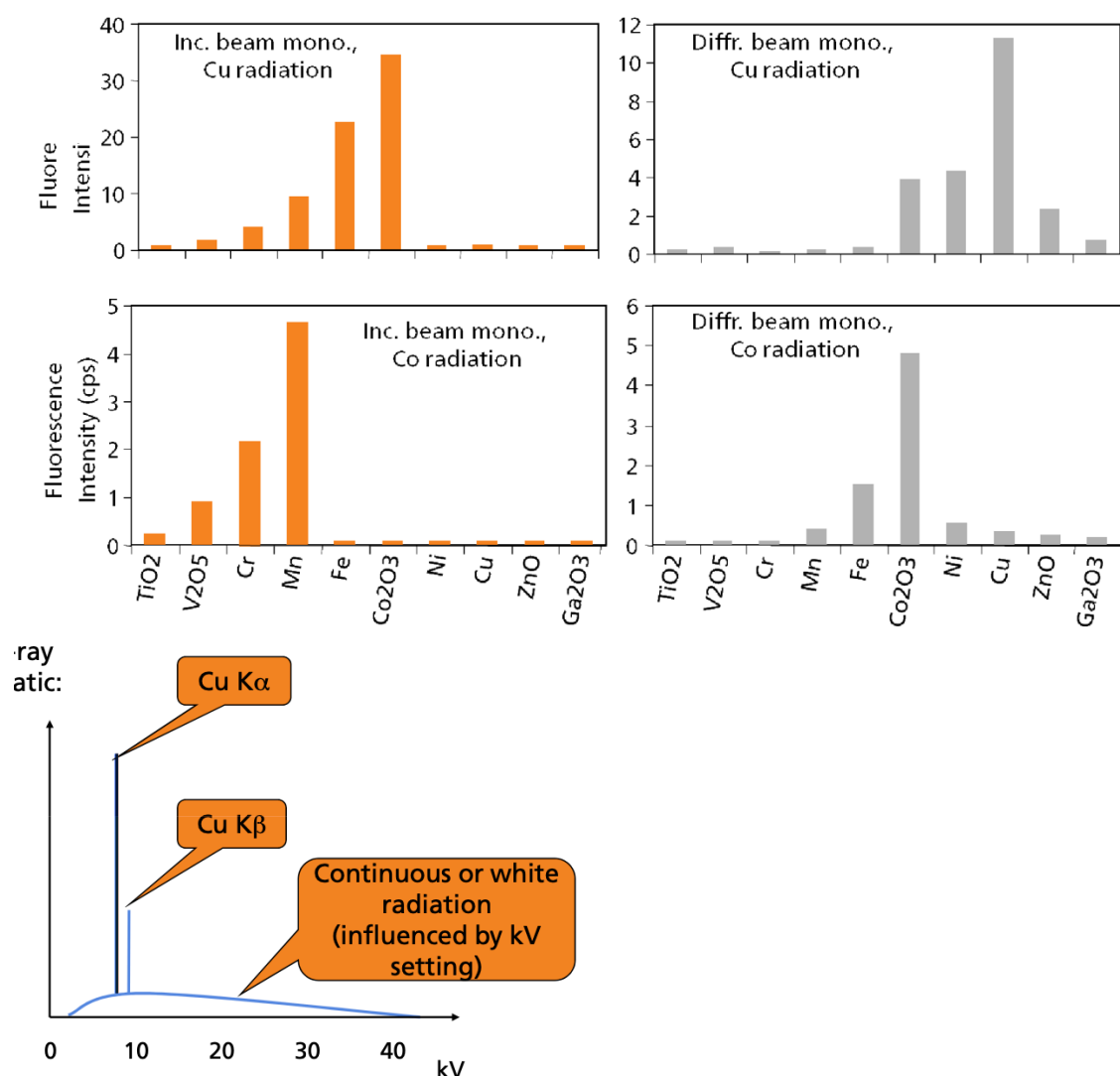
Figure 40 Emission spectrum of Copper X-ray tube[119]

The energy of Cu $K\alpha$ is 8046 eV for that of Fe $K\alpha$ is 6405 eV.[101] By using a monochromator, only the energy of Cu $K\alpha$ can be selected and the fluorescence will be gone. Due to fluorescence, the intensity of Cu $K\alpha$ will have decreased significantly, thus the intensity of a measurement using a monochromator will be very low. The measurement should therefore be run for a longer duration.

Another possibility could be to change the detector settings. By changing the PHD values of the detector, a selection of the measured energies can be made. As a result, a window excluding the fluorescence can be used to select only the Cu $K\alpha$ peak. By increasing the lower limit to a value above the fluorescence energy, the fluorescence can be excluded. This is visualized in Figure 41.
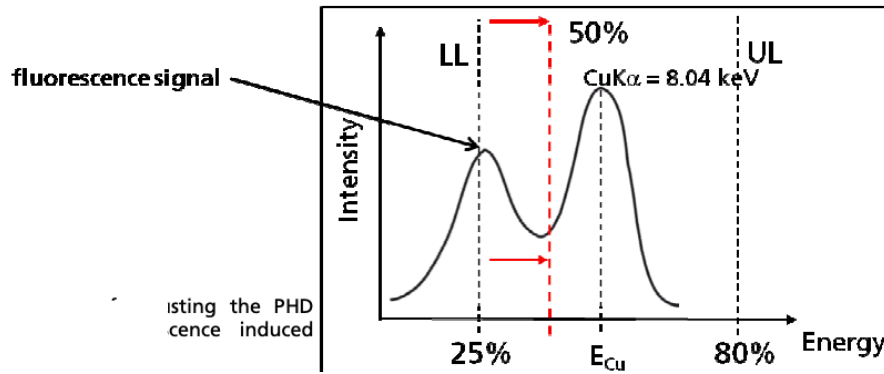
Figure 41 increasing the lower limit of the PHD values of the detector may lead to the exclusion of fluorescence in your sample.[120]

A third option to decrease the amount of fluorescence is to use a cobalt X-ray tube. Since the Co $K\alpha$ combination can be used for the prevention of air scattering and double detection

C.3   DLS

Brownian motion causing diffusion of nanoparticles is dependent on the size of a particle. The diffusion coefficient can be measured by DLS. For a DLS measurement, a constant monochromatic signal is sent out and the detector compares the signals via a correlator. The change of a signal is correlated with the size of a particle. Small particles will have a rapidly changing intensity whereas larger ones will give a smoother intensity change (Figure 42a). Furthermore, the correlation function tells something about the size distribution of the sample. A steep correlation function shows a monodisperse sample and increasing polydispersity is seen by extended correlation decay (Figure 42b).
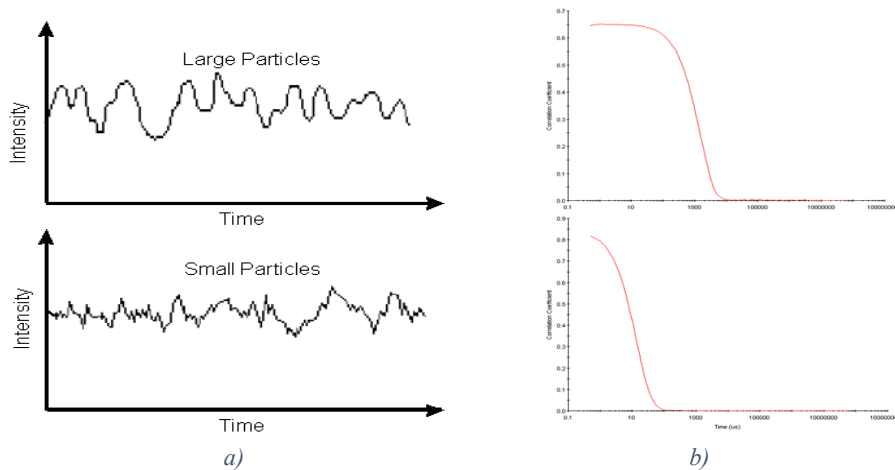

Figure 42 intensity signal (a) of a sample with large or small particles and the corresponding correlation function (b).[72]

Since the intensity is related to the diameter of particles via $I \sim D^6$, large particles will give a high intensity and small particles will give a low intensity. This means that when looking at a polydisperse sample, let say 10 nm and 1000 nm, the contribution of the small particle will extremely small. Figure 43 shows the big difference in intensity between particles of 5 and 50 nm.[101]
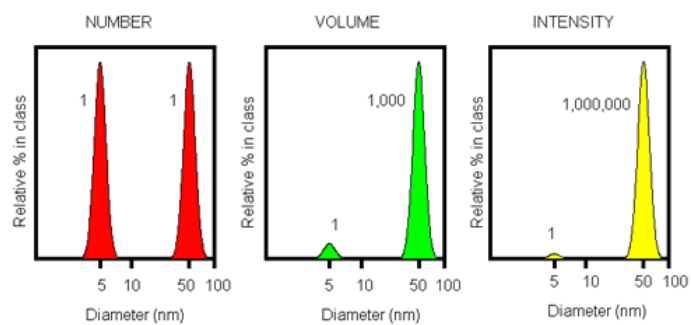
Figure 43 Number, volume and intensity distributions as an illustration of the ratio differences between the number and intensity[98].

The counting rate for DLS should be below 1250kHz and is optimal at 500kHz.

Spherical behavior is lost above a certain percentage[98]